INDUCTION MOTOR BEARING FAULT DETECTION USING A SENSORLESS APPROACH

A Dissertation

by

LIN WANG

Submitted to the Office of Graduate Studies of
Texas A&M University
in partial fulfillment of the requirements for the degree of

DOCTOR OF PHILOSOPHY

May 2007

Major Subject: Mechanical Engineering

INDUCTION MOTOR BEARING FAULT DETECTION USING A SENSORLESS APPROACH

A Dissertation

by

LIN WANG

Submitted to the Office of Graduate Studies of
Texas A&M University
in partial fulfillment of the requirements for the degree of

DOCTOR OF PHILOSOPHY

Approved by:

Chair of Committee,	Alexander Parlos
Committee Members,	Suhada Jayasuriya
	Edgar Sanchez-Sinencio
	Won-jong Kim
Head of Department,	Dennis O'Neal

May 2007

Major Subject: Mechanical Engineering

ABSTRACT

Induction Motor Bearing Fault Detection Using a
Sensorless Approach. (May 2007)
Lin Wang, B.S., Zhejiang University, Hangzhou, China;
M.S., Southwest Jiaotong University, Chengdu, China
Chair of Advisory Committee: Dr. Alexander G. Parlos

Continuous condition assessment of induction motors is very important due to its potential to reduce down-time and manpower needed in industry. Rolling element bearing faults result in more than 40% of all induction motor failures. Vibration analysis has been utilized to detect bearing faults for years. However, vibration sensors and expert vibration interpretation are expensive. This limitation prevents widespread monitoring of continuous bearing conditions in induction motors, which provides better performance compared to periodic monitoring, a typical practice for motor bearing maintenance in industry. A strong motivation exists for finding a cost-effective approach for the detection of bearing faults. Motor terminal signals have attracted much attention. However, not many papers in the literature address this issue as it relates to bearing faults, because of the difficulties in effective detection.

In this research, an incipient bearing fault detection method for induction motors is proposed based on the analysis of motor terminal voltages and currents. The basic idea of this method is to detect changes in amplitude modulation between the spatial harmonics caused by bearing faults and the supply fundamental frequency. This amplitude modulation relationship can be isolated using the phase coupling property. An Amplitude Modulation Detector (AMD), developed from higher order spectrum estimation, correctly captures the phase coupling and isolates these modulation rela-

tionships.

In this research, in-situ bearing damage experiments are conducted so that the accelerated life span of the bearing can be recorded and investigated. Experimental results shown in this dissertation are based on different power supplies, load levels, VSI control schemes, and motor operating conditions. Taking the mechanical vibration indicator as a reference for fault detection, the proposed method is demonstrated to be effective in detecting incipient bearing faults in induction motors. If motors are operating at near steady state conditions, then experimental results show that the bearing fault detection rate of the proposed approach is 100%, while no false alarms are recorded.

To My Parents

ACKNOWLEDGMENTS

I would like to express my appreciation to my committee chair and advisor, Dr. Alexander G. Parlos, for his patience, continuous guidance, technical support and advice through the course of my research work. I would also like to express my appreciation to other members of my committee: Dr. Suhada Jayasuriya, Dr. Edgar Sanchez-Sinencio and Dr. Won-jong Kim, for their comments and advice.

Finally, I would like to thank all the students at NIML, especially Dr. Parasuram, Mr. Choi, Dr. Aninda and Dr. Dan, for their insightful discussions on related and unrelated topics.

TABLE OF CONTENTS

CHAPTER Page

CHAPTER Page

Page

LIST OF TABLES

LIST OF FIGURES

FIGURE Page

FIGURE Page

FIGURE Page

FIGURE Page

FIGURE Page

CHAPTER I

INTRODUCTION

A. Induction Motor Fault Detection and Diagnosis

1. Motivation

Induction motors play a very important role in the safe and efficient running of any industrial plant. Like all rotating machinery, induction motors are not 100% reliable. Several parts of the machine are especially susceptible to failure. For example, the stator windings are subject to insulation failures caused by mechanical vibration, heat, age, damage during installation, and contamination by oil. The rotor bars are subject to failures caused by a combination of various stresses that act on the rotor. Machine bearings are subject to excessive wear and damage caused by inadequate lubrication, incorrect loading, or misalignment. In many applications, these failures can shut down an entire industrial process. The unexpected shutdowns cost the user both time and money that can be avoided if some form of early warning system is used. Furthermore, such systems add to safety and reliability, which are key factors in a wide range of industrial environments. Fault detection and diagnosis schemes are intended to provide advanced warnings so that corrective action can be taken without detrimental interruption of the process. Extensive fault diagnosis of motors can lead to greater plant availability, extended plant life, higher quality products, and smoother plant operation.

The goal of fault detection and diagnosis is to ensure the success of the planned operations by providing information that recognizes and indicates anomalies of sys-

---

The journal model is *IEEE Transactions on Automatic Control.*

tem behavior. This information not only keeps the operators better informed of the status of the system, but also assists them in taking appropriate remedial actions to eliminate any abnormal system behavior. The success of a fault detection and diagnosis algorithm is fundamentally related to the available information, the features of the information that it uses, and the technique with which these features are evaluated. A fault is defined as the inability of a system to perform in an acceptable manner. A fault manifests itself as a deviation in observed system behavior from a set of acceptable behaviors. Fault detection is the recognition of the unacceptable behavior, and fault diagnosis is the identification of a component or set of components in the system that caused the fault, including the type, location, magnitude, and time of the fault. The detection and diagnosis tasks should be considered separately, but this distinction is not always made clear in practice because detection and diagnosis processes can be closely intertwined. Fault detection consists of 1) collecting data, 2) extracting relevant features from the data and evaluating those extracted features into a form of fault indicators, and 3) comparing those indicators to baseline observations formed from the normal condition of the system. Based on the results of this comparison, a fault can be declared.

Before the literature review, motor anomalies, motor faults, and motor fault detection and diagnosis methods are reviewed in this chapter.

2. Motor Anomalies

Motor anomalies are not faulty conditions of the machine. They are normal machine operating conditions that occur when there are temporal variations in the motor inputs and disturbances. Motor anomalies, being major sources of false alarms, can produce signatures similar to some faults. Motor anomalies originate from supply imbalance and the load fluctuations.

a. Supply Imbalance

Three phase electric power systems generally provide voltage supply at the generating station that is well balanced in both magnitude and displacement. At the distribution end, unbalanced single phase loads and non-linear loads cause unequal voltage drops in the transformer and line impedances. This results in an unbalanced supply voltage at the point of utilization. The supply imbalance will affect fault detection to some extent. For example, the majority of the methods developed until now to detect stator faults are based on monitoring the negative sequence of the current. If the supply becomes unbalanced, a negative sequence current will flow because of the motor's low negative sequence impedance. Using only current measurements, it is difficult to distinguish between the negative sequence current due to unbalanced voltage and due to motor stator deterioration. This makes the negative sequence of the current alone an unreliable indicator for incipient fault detection.

b. Load Fluctuations

If the load torque varies, the stator current spectrum contains load induced frequency components that coincide with those caused by a fault condition. In the sinusoidal steady-state, a load torque oscillation produces a related oscillation in the electromagnetic field. The current drawn by the motor contains all of the frequency components found in the load torque. The magnitude of these developed load torque harmonics are primarily dependent upon the system inertia and the frequency of the torque oscillation. If the stator flux linkage is purely sinusoidal, then any oscillation in the load torque at multiples of the rotational speed will produce stator currents at frequencies [1],

$$f_{load} = f_e \pm k f_{rm} = f_e \left[1 \pm k \frac{(1-s)}{p/2} \right], \tag{1.1}$$

where f_e is the electrical supply frequency, $k = 1, 2, 3, \ldots$, s is the per unit slip, p is the number of poles, and f_{rm} is the mechanical rotor speed in Hertz. Since motor faults, like air-gap eccentricity and broken rotor bars generate the same frequencies as those given in equation (1.1), it is clear that when induction motors operate with a typical time-varying load, stator current frequency components caused by torque oscillations can obscure those caused by fault conditions.

3. Motor Faults

Motor reliability studies have been performed by both General Electric, under the sponsorship of the Electric Power Research Institute [2], and the IEEE Industry Application Society [3], in order to evaluate the reliability of electric motors and to identify the design and operational characteristics offering the potential to increase their reliability. These two surveys are for motors energized by power supply mains. Another motor reliability survey for motors energized by inverters was performed by Thorson [4]. The failure rates are reported to be 47% for stator faults, 5% for rotor faults, 32% for bearing faults, and 16% for other faults. However, the original sources of the Thorson survey cannot be tracked down in the literature. Table I shows the first two motor reliability survey results, where the first two columns include motors of all types and the third column includes only squirrel-cage induction machines.

The majority of electric machine component failures are related to three main components of motors, the stator, the rotor, and the bearings. Bearing failures account for 30% to 50% of all electric motor failures. In the following sections, failures related to each of these motor components are discussed.

Table I. Motor Reliability Survey Results [2, 3].

Survey Size	EPRI Survey 1052 Failures	IEEE IAS Survey 380 Failures	IEEE IAS Survey 304 Failures
Stator	36%	26%	25%
Rotor	9%	8%	9%
Bearings	41%	44%	50%
Others	14%	22%	16%

a. Stator Faults

Stator faults are usually insulation related, which might be inter-turn, phase-to-phase, and phase-to-ground shorts. While the insulation is most susceptible to failure where the end windings enter the stator slots, failures also occur at locations where the conductors pass through the motor casing [5]. Manufacturing defects that include voids, contamination, and penetration by foreign materials, such as oil or metal, frequently cause failures in the electrical insulation of the machine. Damaging conditions are also produced by the large electrical voltage stresses at conductor bends, electro-dynamic forces produced by the winding current, thermal aging from multiple heating and cooling cycles, and mechanical vibrations from internal and external sources. The deterioration of the insulation strength eventually leads to shorted or grounded stator windings that give rise to zero and negative sequence currents.

b. Rotor Faults

Bar defects occur in squirrel-cage rotors. These defects come from two sources [5]. The first source is associated with high temperatures and large centrifugal forces

developed during transient operations, such as startup. Defective casting (voids) or poor end-ring joints formed during manufacturing are the second source. Once the initial defect occurs, propagation of the fault is the result of multiple startups and load fluctuations that produce high centrifugal forces. The condition is further accentuated by the heating and cooling cycles of the rotor. Similar to stator windings, damage in wound rotors generally occurs at the end regions. Mechanical defects produced by high centrifugal stresses experienced by rotor components can lead to catastrophic failures. These failures are accelerated if the cooling system contains impurities, which encourage corrosion and degrade the mechanical strength of the rotor. Long before unassisted disassembly occurs, the machine begins to exhibit some level of mechanical imbalance. In many cases, this eccentricity of the rotor is amplified by the unbalanced magnetic pull produced by the magnetic field of the machine. This situation is compounded when the asymmetrical heating leads to thermal bending of the rotor. Machines with small air-gaps are especially susceptible and the possibility of contact between the rotor and the stator becomes real.

c. Bearing Faults

Over the past several decades, rolling-element bearings have been utilized in many electric machines, while sleeve bearings are installed in only the larger machines. In the case of induction motors, rolling-element bearings are widely used to provide rotor supports. Bearing deterioration, which accounts for 30% to 50% of all machine failures, is now one of the main causes of induction motor failures [2, 3, 4]. The causes and classifications of bearing failures are discussed in Chapter II.

d. Air-Gap Eccentricity

An induction motor can fail due to air-gap eccentricity, which can be caused by many reasons. There are two types of air-gap eccentricities: static air-gap eccentricity and dynamic air-gap eccentricity. In the case of static air-gap eccentricity, the position of the minimal radial air-gap length is fixed in space. Static air-gap eccentricity can be caused by the ovality of the core or by the incorrect positioning of the stator or rotor at the commissioning stage. In the case of dynamic air-gap eccentricity, the center of the rotor is not at the center of the rotation and the minimum air-gap rotates with the rotor. It follows that dynamic eccentricity is time and space dependent, whereas static eccentricity is only space dependent. Dynamic eccentricity can be caused by a bent rotor shaft, wear of bearings, misalignment of bearings, mechanical resonances at critical speed, and so on. Both types of eccentricities cause excessive stressing of the motor and greatly increase bearing wear. In addition, the radial magnetic force waves produced by eccentricity can also act on the stator core and subject the stator windings to unnecessary and potentially harmful vibrations. It is also possible that rotor-to-stator rub might occur, leading to damage of the core, windings, and the rotor cage [6].

4. Fault Detection and Diagnosis Methods

Detection techniques consider one or more fault indicators of the observations. These indicators are calculated from the measured data, which in some way represent the state or behavior of the system. For fault detection, limits may be placed on some of the indicators, and a fault is detected whenever one of the indicators is evaluated to be outside its limits. The indicators of a fault detection scheme are mainly derived from three approaches, data-driven, knowledge-based, and analytical methods.

The data-driven indicators are derived directly from measurements. The analytical approach uses mathematical models often constructed from physical principles, while the knowledge-based approach uses qualitative models. The analytical approach is applicable to information-rich systems, where satisfactory models and sufficient sensors are available. Meanwhile, the knowledge-based approach is better applied to information-poor systems, where few sensors or poor models are available [7].

a. Data-Driven Methods

Accurate and detailed models are difficult to develop for complex systems containing a large number of inputs, outputs, and/or states. Thus, analytical methods cannot be successfully applied to complex systems. In these situations, data-driven methods are widely applied. Data-driven methods use the data collected during normal operating conditions and during specific faults to develop the fault indicators for detecting and diagnosing failures. Because these methods are data-driven, their effectiveness is highly dependent on the quantity and quality of the measured data. While a large amount of data might be available from many sensors, typically only a small portion might be useful. One must determine with confidence that the useful fraction of the data are not somehow corrupted and that no unknown faults occurred in the system [8, 9, 10].

b. Knowledge-Based Methods

For establishing a knowledge base for fault detection and diagnosis, several approaches have been described in the literature [11]. In general, specific rules are applied in order to set up logical interactions between observed symptoms (effects) and unknown faults (causes). The propagation from the actual fault appearance to observable symptoms follows physical cause-effect relationships such that physical properties and variables

are not only connected to each other quantitatively, but also as functions of time. However, the underlying physical laws are usually not known in analytical form or are too complicated for calculations. Rule-based expert systems are a general technique for representing knowledge in usable forms, and are thus capable of using almost any pre-specified observation feature for diagnosis [12]. Expert systems can be excellent tools for capturing and utilizing knowledge that is not or cannot be captured by traditional techniques, such as models. Expert systems generally work well when a model is not known, or is too complex to develop. In some types of systems, the symptoms used by the expert system are more successful in identifying a fault compared to the model-based diagnosis. This is because some types of symptoms are difficult to relate to a fault through a model, but may easily be related to a fault through a simple rule. However, rule-based expert systems have several drawbacks [13]. Most expert systems are fault specific and are only capable of diagnosing faults that are represented in the knowledge base. In a complex system, it may not be possible or practical to represent all possible faults. Moreover, although rules can easily be added to the knowledge base, expert systems can be difficult to modify and maintain in certain circumstances. This is because the knowledge base would require extensive reworking following a system modification or sensor change.

c. Analytical Methods

Fault diagnosis can be achieved using a replication of hardware (e.g., computers, sensors, actuators, and other components). In what is known as hardware or physical redundancy, outputs from identical components are compared for consistency. Alternatively, fault diagnosis can be achieved using analytical information about the system being monitored. This is known as analytical or functional redundancy. In contrast to hardware redundancy, in which measurements from different sensors are

compared, in analytical redundancy sensory measurements are compared to analytically obtained values of the corresponding variable. This implies that the inherent redundancy contained in the static and dynamic relationships among the system inputs and outputs is exploited for fault diagnosis. Such computations exploit the present and/or previous measurements of other variables and the mathematical model of the system describing their relationships. The model can use the system input and output data to estimate information about the system, including the output, state, or internal parameters [14, 15].

d. Pattern Recognition

Many data-driven, knowledge-based, and analytical approaches incorporate pattern-based techniques to some extent. Pattern-based methods generally consist of templates or patterns distinguishing acceptable and unacceptable operations. These are then compared to the system observations to determine whether a fault has occurred. Templates or patterns may be determined by performance specifications, by past observations of faulty operations, by expert knowledge, or even from analysis or simulation of a system model. Since pattern recognition approaches are based on inductive reasoning through generalization from a set of stored or learned examples of system process behaviors, these techniques are useful when data are abundant, and expert knowledge is lacking [16]. The artificial neural network (NN) is a particularly promising approach in pattern-based fault detection and diagnosis [6, 17, 18, 19].

e. Motor Condition Monitoring Sensors

While there have been numerous sensors proposed in the literature, such as temperature, flux, etc., the most widely used induction motor fault detection sensors are of mechanical and electrical origin [5].

Mechanical monitoring of electric machines is accomplished through the use of spectral signature analysis, which converts the measured vibration signal into frequency components of constant bandwidth by using Fast Fourier Transform (FFT) [5]. The idea is based on the concept that mechanical vibrations at various frequencies are related to identifiable causes of anomalies in the machine and they can be used to provide an indication of the condition of the machine. The vibrational energy of the machine is measured in units of one of the three related quantities: displacement, velocity, or acceleration. These measurements are accomplished using either displacement probes, velocity transducers, or accelerometers. The appropriate device depends upon the size of the machine and the frequency range of interest; however, it is now common practice for displacement and velocity to be integrated from the acceleration measurements.

While mechanical monitoring has been utilized for decades, most of the recent research has been directed toward electrical monitoring techniques utilizing stator currents of the machine. On the surface, stator currents contain much less information than the magnetic flux density, but are more readily accessible by non-invasive measurement techniques. They have been selected as appropriate signals for processing, together with the supply line voltages in this research. A large amount of research has been directed toward using motor currents to sense stator insulation failures involving turn-to-turn shorts, rotor faults involving air-gap eccentricity, and broken rotor bars.

Thermal monitoring of electric machines is accomplished by measuring either the local or the bulk temperatures of the motor [5]. Local temperatures include those measurements taken with embedded detectors located at hot spots within either the stator core and windings or the motor bearings. While these measurements provide temperature indications at known problem areas, there is still the question of whether the hottest spot in the machine is being monitored. Bearing temperatures are often

surveyed on a routine basis, like vibration levels. They provide a useful warning for tribological problems. Winding temperature is very valuable for determining the limit to which a motor can be loaded and for estimating the remnant life of the winding insulation. Bulk temperatures include the measurements of cooling and lubrication fluids such as the air flowing inside the machine casting and the bearing oil. They are valuable for indicating motor cooling problems and for monitoring motor operation beyond its rating. But, even these temperature measurements can miss isolated problems in the machine.

5. Motor Current Signature Analysis and Electrical Signal Analysis

Traditionally, motor condition has been monitored by measuring variables such as noise, vibration, and temperature. But the implementation of such systems is expensive and they are generally installed only on the largest motors or most critical applications where the cost of the monitoring system can be justified. In addition, the environmental sensitivity of some sensors can cause mechanical monitoring techniques to provide unreliable indications. Mechanical forms of sensing are also limited in their ability to detect some electrical faults such as stator insulation faults. A solution to this problem can be the use of quantities that are already measured in a drive system, or easily accessible in a system with or without drives, e.g., the machine's stator currents and voltages.

In the literature, two categories of fault detection schemes that use the motor terminal signals are presented, Motor Current Signature Analysis (MCSA) and Electrical Signal Analysis (ESA).

The Motor Current Signal Analysis (MCSA), which separates the monitored signal into individual frequency components, is commonly used to detect some induction

machine mechanical faults. Most rotor faults affect either the air-gap permeance or the magnetomotive force (MMF) that cause variations in the air-gap flux density. These flux variations produce stator currents at frequencies related to the fault condition. In MCSA, only motor stator currents are considered as the fault media. This is acceptable in some special environment where the voltage inputs are clean and mostly stationary. However in practical industrial environments, the voltage inputs are highly non-stationary signals where rich harmonic information comes from the supply and other devices, and may mask fault signatures abstracted using MCSA techniques.

The ESA is based on the concept that air-gap flux density variations caused by mechanical and electrical defects produce correlated changes in currents and voltages. Therefore, stator voltages and currents are utilized for fault detection purposes. In this research, both stator currents and voltages are used for motor bearing detection purposes.

"Sensorless" means that only current and voltage measurements are used. Current and voltage monitoring can be implemented inexpensively on any size machine by utilizing the current transformers and potential transformers in the motor control/switch gear centers. Use of the existing current transformers and potential transformers makes it feasible to monitor large numbers of motors remotely from one location. Similarly, these measurements can be easily obtained when a drive system is used to energize the motor.

B. Literature Review

In this research, detection of bearing faults in motors energized by power supply mains and VSI type drives is investigated. The desired fault detection method should be

independent of any physical motor parameters and must utilize only motor terminal currents and voltages.

In the following sections, the literature for bearing fault detection in motors energized by power supply mains and VSI type drives is reviewed.

1. Classification of the Bearing Faults

Depending on the location of the fault, bearing faults can be classified as ball fault, inner race fault, outer race fault, and train fault. But, this classification does not include all bearing faults. In [20], bearing faults are grouped into two categories: single point defects and generalized roughness faults.

A single point defect is defined as a single, localized defect on an otherwise relatedly undamaged bearing surface. A common example is a pit or a spall. A single point defect produces one of the four characteristic fault frequencies depending on which surface of the bearing contains the fault, the ball, the inner raceway, the outer raceway, or the cage. These predictable frequency components typically appear in the machine vibration spectrum and are often reflected into the stator current spectrum. Despite its name, a bearing can possess multiple single point defects.

Generalized roughness is a type of fault where the condition of a bearing surface degrades considerably over a large area and becomes rough, irregular, or deformed. This damage may or may not be visible to the unaided eye. There is no localized defect to be identified as the fault; rather, large areas of the bearing surfaces deteriorate. A common example is the overall surface roughness produced by a contamination or loss of lubricant. The effects produced by this type of fault are difficult to predict, and there are no characteristic fault frequencies in the current or vibration spectra associated with this type of fault [20].

There are many reasons that cause the general roughness fault in a bearing. Some

of the more common fault sources include contamination of the lubricant, lack or loss of lubricant, shaft currents, and misalignment. While these fault sources may also produce single point defects, it is common that they produce unhealthy bearings that do not contain single point defects. If one of these bearings is removed from service prior to a catastrophic failure, a technician can easily recognize that a problem exists within the bearing because it either spins roughly or with difficulty. However, upon a visual examination, there is no single point defect, and the actual damage of the bearing may or may not be visible to the unaided eye. For this kind of fault, it is stated in [20] that the specific way in which these bearings fail is unpredictable. Therefore, the effect the fault has on machine vibration and stator current spectra is unpredictable. However, as the fault increases in severity, the magnitude of the broadband machine vibration increases accordingly.

2. Bearing Fault Detection in Induction Motors Energized by the Power Supply Mains

In the literature, most bearing fault detection techniques for induction motors are intended for detecting single point defects. To detect such faults, vibration analysis is widely used. In MCSA approaches, frequency analysis, time-frequency analysis, and model based method are used for detecting single point defects. For bearing generalized roughness faults, model based approaches are used.

a. Frequency Analysis

Single-point defects produce one of the four characteristic fault frequencies in machine vibration spectrum depending on which bearing surface contains the fault. These frequencies are listed below. More details can be found in [4, 20, 21, 22].

Cage fault frequency:

$$F_{CF} = \frac{1}{2}F_R(1 - \frac{BDcos\beta}{PD}), \tag{1.2}$$

Outer raceway fault frequency:

$$F_{ORF} = \frac{N_B}{2}F_R(1 - \frac{BDcos\beta}{PD}), \tag{1.3}$$

Inner raceway fault frequency:

$$F_{IRF} = \frac{N_B}{2}F_R(1 + \frac{BDcos\beta}{PD}), \tag{1.4}$$

Ball fault frequency:

$$F_{BF} = \frac{PD}{2BD}F_R(1 - \frac{BD^2cos^2\beta}{PD^2}). \tag{1.5}$$

Ball bearing dimensions are shown in Figure 1. In the above equations, BD is the ball diameter; PD is the bearing pitch diameter; N_B is the number of rolling elements; β is the contact angle; and F_R is the rotor frequency.

It has been shown that single point defects in damaged bearings cause air gap variations. These variations generate stator current harmonics at the following frequencies [21],

$$F_{BNG} = |F_E \pm m \cdot F_V|, \tag{1.6}$$

where F_E is the supply fundamental frequency, F_V is one of the characteristic vibration frequencies, and m = 1, 2, 3, ...

Equation (1.6) is the most often quoted model studying the influence of bearing damage on the induction machine stator current. However in the literature, researchers reported that it's not easy to identify these bearing fault related frequencies in the stator current spectra [23, 24]. Studies in [25] gave the following modified version of equation (1.6),

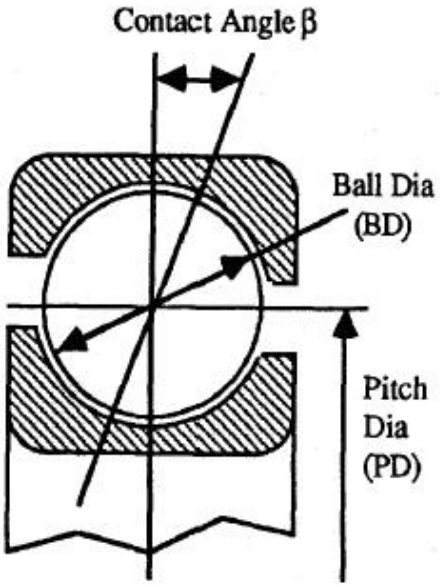

Fig. 1. Ball Bearing Dimensions.

Outer raceway fault frequency:

$$F_{BNG\_ORF} = |F_E \pm m \cdot F_{ORF}|, \tag{1.7}$$

Inner raceway fault frequency:

$$F_{BNG\_IRF} = |F_E \pm F_R \pm m \cdot F_{IRF}|, \tag{1.8}$$

Ball fault frequency:

$$F_{BNG\_BF} = |F_E \pm F_{CF} \pm m \cdot F_{BF}|. \tag{1.9}$$

The main drawback of the bearing defect frequency identification method is that calculation of a bearing defect frequency requires full knowledge of the bearing design parameters. Usually such parameters are not available, except to bearing designers. Moreover, it is difficult to identify the contact angle β because it is depended on the

practical assembling.

b. Time-Frequency Analysis

Induction motor stator currents are known to be non-stationary and the Fast Fourier Transformation is not suitable for such non-stationary signals [26]. In order to overcome this problem, a time-frequency method is proposed in [26] and [27].

In [26], inner and outer race bearing defect frequencies are investigated. The total number of balls and the fundamental electrical frequency are needed for the calculation. The Short Time Fourier Transformation (STFT) is used to capture time variation of the bearing defect frequencies. Bearing conditions are determined statistically, by analyzing the bearing fault related spectrum and comparing it with a baseline spectrum.

Compared to STFT, Wavelet Packet Decomposition (WPD) is known to provide optimal combination of time and frequency resolution. This results in better diagnostic performance. In [27], small ranges of bearing defect frequency bands are isolated from the entire stator signature using WPD. The Root Mean Square (RMS) values of the frequency bands are compared with a baseline value and the bearing condition is determined accordingly. The bearing defect frequency bands are associated with single point defects. Hence, identifying a specific defect band requires bearing dimensions and other bearing design parameters.

c. Model Based Method

A recurrent neural network model was used to detect single point defects in [6]. In this method, quasi-stationary data segments in the terminal currents are grouped together so that the non-stationarity of the signal can be avoided. Then, a neural network model is used to predict the healthy system response.

For bearing generalized roughness faults, Stack presented pioneer work using mechanical vibration analysis [22]. He also used a stator current Auto-Regressive (AR) model to detect generalized bearing faults [28]. In this paper, the current fundamental frequency is removed before sampling the data, so that variations caused by the supply voltage fundamental can be avoided. But, the problem is that the other frequency components of the supply voltage are presented in the current spectrum and they are time-varying. Moreover, in most experimental results shown in this paper, the fault indicator drops down to the healthy level while bearings are already damaged. This makes fault detection difficult.

3. Bearing Fault Detection in Induction Motors Energized by Voltage Source Inverter (VSI)

Induction machine drives can be classified into two major categories, Voltage Source Inverter (VSI) and Current Source Inverter (CSI). While CSI's were originally the choice for motor drives, they have pretty much been replaced by VSI's for all but the higher power levels where the controlled output current and reduced load harmonics are desired [29]. VSI type drive is used in this research because it is commonly used in industry.

Bearing fault detection in induction machines energized by VSI are rarely discussed in the literature. Only one method has been published in the open literature, the Vienna Monitoring Method (VMM).

The VMM was proposed in an attempt to reduce the negative effects from inverter harmonics [30, 31, 32]. The VMM is a time domain, model based method. In this method, the stator resistance is needed to model the stator flux and the rotor position is needed to transform the current space phasor in the rotor fixed reference frame. Two models are used in VMM, the voltage model and the current model. In

case of an ideal symmetric motor, both models calculate the same torque. As a fault occurs, the distribution of air gap flux is distorted and a deviation appears between the torque values calculated from the two different models. The voltage model is able to indicate the real (faulty) motor performance, while the current model represents the healthy machine. The deviation of the torque is found to be approximately proportional to load torque. Although the authors stated that this method can be used to detect bearing faults, the paper does not provide suitable evidence to support the claim. Moreover, in this method accurate knowledge of induction motor parameters is needed, but such accuracy is usually not practically feasible in most applications.

Although very few papers discuss bearing fault detection of motors energized by VSI drives, yet there exists literature on other kinds of motor faults, like stator shorts and broken rotor bars.

Bellini and Filippetti used the torque and flux components of the current for the detection of stator short circuit and broken rotor bar faults [33, 34]. They conclude that the flux current is suitable for fault diagnosis purposes and the torque current is not robust enough to be a diagnostic index. The reason is that the torque current is strongly affected by load torque values and ripples.

Stator faults are also investigated in [35], where the discrete wavelet transform is used on both the current and voltage, and in [36], where a neural network model is used to estimate the reference signals.

In [37], a rotor cage defect machine model based on motor parameters is developed for rotor cage fault diagnosis under inverter fed conditions. It serves two purposes: to determine the signature frequencies of a cage defect, and to generate the training data for a neural network model. The NN model is used for the purpose of fault classification.

C. Research Objectives

From the previous sections, it can be seen that there is a strong motivation to develop an improved and cost-effective fault detection method for induction motor bearing faults. The objectives of this research are to

- Detect bearing faults when motors are energized by power supply mains and VSI type drives,
- Detect bearing failures using only motor terminal voltage and current measurements, i.e., in a sensorless manner, and,
- Develop an approach that is independent of physical motor parameters, so that it can be applicable to various induction motors, independent of voltage and power ratings, and manufacturers.

D. Proposed Approach

To develop a bearing fault detection scheme, bearing fault data are needed. Such data can be generated in an offline manner. That is, to disassemble the bearing, damage it separately, and then assemble the machine in order to collect damaged bearing data. The act of disassembling, reassembling, remounting, and realigning the test motor significantly alters the current and vibration characteristics of the machine, which is one of the difficulties in collecting fault data for a bearing fault detection scheme. In this research, in-situ bearing damage experiments are conducted so that the life span of the bearing can be accelerated and the bearing fault detection scheme can be developed and validated.

In both single defect and general roughness bearing faults, the damaged bearing leads the radial motion between the stator and the rotor. This type of motion

varies the air gap of the machine in a way which can be characterized as a modulation relationship with fundamental frequency of the supply. Although this type of modulation relationships exit in the healthy condition, they are changed by the damaged bearing. In single point defect bearing faults, the fault related frequencies can be detected according to the bearing geometry dimensions, while in the generalized roughness bearing faults, the fault related frequencies are residing in wide frequency bands and are not easily predictable. Moreover, the damaged bearing impedes the rotor rotation and causes additional loading on the motor. Although the load itself is small and ignorable, the load fluctuations imposed on the motor increase. This load fluctuations are also modulated with the fundamental frequency of the supply.

Bearing faults can be captured in frequencies that are modulated with the fundamental frequency of the supply. This modulation relationship can be isolated using the phase coupling between the bearing fault frequencies and the fundamental frequency of the supply. An Amplitude Modulation Detector (AMD), developed from estimates of the higher order spectrum, can correctly capture the phase coupling and isolate the modulation relations. This approach is proposed in this research.

The system power supply plays a very important role in bearing fault detection. Variations in the power supply definitely change the stator current spectrum and mask bearing faults. To negate the effects of the power supply changes, bearing fault indicators are developed using the combinations of the stator current AMD and the voltage AMD.

E. Research Contributions

The main contribution of this research is the development and validation of a method for the detection of bearing faults in induction motors. The method is characterized

by the following attributes:

- It is applicable to motors energized by power supply mains and VSI type drives,
- It requires monitoring of the motor terminal currents and voltages only, and,
- Even though it is a model-based method, it does not make use of any physical motor parameters, so that it is easily portable to induction motors of different voltage, power ratings and to induction motors made by different manufacturers.

F. Organization of the Dissertation

It is expected that this research will provide a powerful general method for incipient bearing fault detection in induction motors.

In Chapter II, an overview of bearing fault causes and effects are discussed. The experimental test beds used in in-situ bearing damage are introduced. In Chapter III, the higher order spectrum, the amplitude modulation detector, the system modulation model and the bearing fault indicators developed in this research are summarized. In Chapter IV, the experimental and the analysis results of the induction motor bearing faults under different power supplies, load levels, VSI control schemes, and operating condition are presented. In Chapter V, a summary of this dissertation, the conclusions reached from this research, and the directions for future research are given.

CHAPTER II

BEARING FAULTS AND DESCRIPTION OF EXPERIMENTAL SETUPS FOR IN-SITU BEARING DAMAGE

A. Overview of Bearing Faults and Failures

Bearing problems are one of the main causes of induction motor failures, accounting for 30% to 50% of all induction motor failures [2, 3, 4].

1. Causes of Motor Bearing Faults and Failures

Rolling element bearings generally consist of two rings, an inner and an outer, between which a set of balls or rollers rotate in raceways. Under normal operating conditions of balanced load and good alignment, fatigue failure begins with small fissures, located below the surfaces of the raceway and rolling elements. These fissures gradually propagate to the surface, generating detectable vibrations and increasing noise levels. Continued stresses cause fragments of the materials to break, producing a localized fatigue phenomena known as flaking or spalling. Once started, the affected area expands rapidly contaminating the lubrication and causing localized overloading over the entire circumference of the raceway. Eventually, failure of the bearing results in rough running. While this is the normal mode of failure in rolling element bearings, there are many other conditions that reduce the time of bearing failure. These external sources include contamination, corrosion, improper lubrication, improper installation, or brinelling [21].

Contamination and corrosion frequently accelerate bearing failure because of the harsh environment present in most industrial settings. Dirt and other foreign matter that is commonly present often contaminate the bearing lubrication. The abrasive

nature of these minute particles, whose hardness can vary from relatively soft to diamond like, cause pitting and sanding actions that give way to measurable wear of the balls and raceways. Bearing corrosion is produced by the presence of water, acids, deteriorated lubrication, and even perspiration from careless handling during installation. Once the chemical reaction has advanced sufficiently, particles are worn off, resulting in the same abrasive action produced by bearing contamination [21].

When a bearing operates with the proper lubrication and at the right speed, the balls or rollers lift off the raceway slightly and there is an oil film between the rolling elements and the raceways. This film is called Elasto-Hydro-Dynamic (EHD) film. This extremely thin film protects and lubricates the bearing while it is running. Improper lubrication includes both under and over lubrication. In either case, the rolling elements are not allowed to rotate on the designed oil film, causing increased levels of heating. The excessive heating causes the grease to break down, which reduces its ability to lubricate the bearing elements and accelerates the failure process.

Installation problems are often caused by improperly forcing the bearing onto the shaft or in the housing. This produces physical damage in the form of brinelling or false brinelling of the raceways, leading to premature failure. Misalignment of the bearing is also a common result of defective bearing installation.

Brinelling is caused when the load applied to a ball bearing exceeds the elastic limits of the steel and the raceways are permanently deformed. Brinelling creates measurable dents at each ball location similar to the deformation caused by a Brinell Hardness Tester. This type of damage can occur quite easily if proper care is not taken. High energy impacts (from hammers and smash-ups), improper bearing handling, and incorrect spindle assembly can all damage bearings. While this form of damage is rare, a form of 'false brinelling' occurs more often.

False brinelling is not related to excessive loads. False brinelling is caused by

ambient vibration. Even a brand new bearing, sealed in a box on a shelf, is subject to false brinelling if it is exposed to environmental vibrations for an extended period. When a bearing is not operating it is subject to false brinelling in the box or in the machine. When a bearing is running, it is protected by the EHD film. When the bearing is stopped there is no EHD film and there is metal to metal contact. That is when false brinelling can quietly attack bearings. The combination of metal to metal contact and vibration creates wear and corrosion patterns that mimic brinelling.

Bearing failures can be classified to single point defects and generalized roughness faults. In both cases, fault related frequency components are modulated with the fundamental frequency in stator current. These modulation relationships are discussed in the following sections.

2. Basis for Amplitude Modulation

A frequency domain representation of amplitude modulation is depicted in Figure 2, where F_s is the baseband signal component and F_c is the carrier frequency. In this illustration, a signal with frequency F_s and phase ϕ_s interacts with another signal at F_c, ϕ_c to produce two new sideband components at F_c+F_s ,$\phi_c+\phi_s$ and F_c-F_s, $\phi_c-\phi_s$. Because the phases of the two sideband components are related to the phases of F_c and F_s, this type of interaction is generally referred to as Quadratic Phase Coupling (QPC).

A standard analytic tool for the detection of QPC is the bispectrum and its normalized form, the bicoherence [22].

3. Amplitude Modulation Relationships in Bearing Faults

Single point defects begin as localized defects on the raceways or rolling elements. As the rolling elements pass over these defect areas, small collisions occur producing

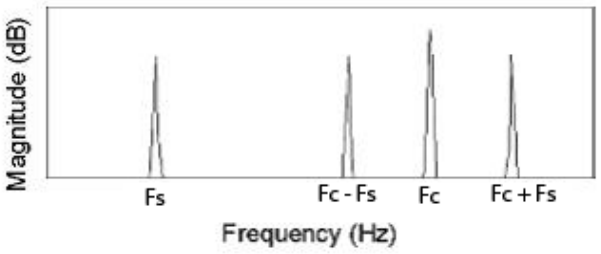

Fig. 2. Basic Amplitude Modulation in the Frequency Domain.

mechanical vibration shockwaves. These shockwaves then excite the frequencies of natural mechanical resonance in the machine. This process occurs every time a defect collides with another part of the bearing, and its rate of occurrence is equal to one of the previously defined characteristic fault frequencies, as shown in equations (1.2) to (1.5). These characteristic fault frequencies are modulated with the mechanical resonant frequencies (the carriers) [21, 27].

The relationship of the bearing vibration to the stator current spectrum can be determined by considering that any air gap eccentricity produces anomalies in the air gap flux density. Since ball bearings support the rotor, any bearing defect will produce a radial motion between the rotor and the stator of the machine. The mechanical displacement resulting from damaged bearings causes the air gap of the machine to vary in a manner that can be described by a combination of rotating eccentricities. These variations generate stator currents at predictable frequencies, as shown in equation (1.6) [21]. Although equation (1.6) is improved further by [25], the modulation relationship between the bearing fault characteristic frequencies and the supply fundamental frequency always hold.

Bearing generalized roughness faults are common in industry, but they are often neglected in the research literature. Many of the newer, more sophisticated condition

monitoring techniques focus only on single point defects. This explains the discrepancy between the large number of state-of-the-art techniques in the research literature and their lack of use in industry [20].

Bearing generalized roughness faults do not excite any one of those characteristic fault frequencies as in the case of single point defects. But, they alter the current spectrum in ways that are similar to the spectrum of bearings with single point defects. Bearings with generalized roughness exhibit radial motion between the stator and the rotor. Like the single defect cases, this kind of motion varies the air gap of the machine in a way which can be characterized as the modulation relationship with the supply fundamental frequency. For bearings with single point defect, fault related frequencies can be decided according to the bearing geometry dimensions, while for generalized roughness bearings, fault related frequencies are located in wide frequency bands and are not predictable.

Additionally, in both the single defect and generalized roughness bearing faults, the damaged bearing impedes the rotor rotation and causes extra load to the motor. Although the load itself is small and ignorable, the load fluctuation of the system is increased. This kind of load fluctuation is also modulated with the supply fundamental frequency, as indicated by equation (1.1).

4. Bearing Faults Caused by the In-situ Bearing Damage Experiments

In a practical environment, bearing single-point defects and general roughness defects cannot be distinguished absolutely. When a bearing is damaged, most possibly these two classes of faults occur at the same time. It is necessary to develop a method that can deal with the combination of these two classes of faults.

As discussed in previous sections, bearing fault related frequencies are modulated with the stator current fundamental frequency. No matter what the classification of

the bearing fault is and what the real fault signature frequencies are, this amplitude modulation relationship always exits. This is the basic idea of the proposed approach in this research. Note that these fault frequency components are not only modulated with the stator current fundamental frequency, they are also modulated with all other harmonics in the supply voltage.

Using the proposed approach, bearing faults can be isolated without knowing the exact fault signature frequencies. Hence, bearing physical dimensions and motor parameters are not needed so that the proposed method is independent of the physical motor parameters.

The proposed method is intended to detect both single point defects and generalized roughness bearing faults. But, bearing damaging experiments conducted in this research usually damage bearings in a way that mainly results in generalized roughness faults. When a bearing is slightly damaged by the shaft currents, there are no obvious pits or roughness can be seen by the naked eyes on any surfaces of the bearing. Large area roughness appears only after the bearing is heavily damaged. In Figure 3, one of bearings damaged in this research by the shaft currents is shown. Only large area roughness can be seen and there are no significant pits on the surfaces of this bearing although it was damaged heavily. Because of this, the detection of bearing single point defects is not fully demonstrated in this research.

B. Experimental Staging of Bearing Faults via Shaft Currents

1. Motivation for In-situ Bearing Damage Experiments

When experimental bearing fault data are collected for research purposes, the test bearings are typically seeded with faults generated off-line, e.g., scratching, drilling, or Electric Discharge Machining (EDM), and then placed in a test motor. The act of

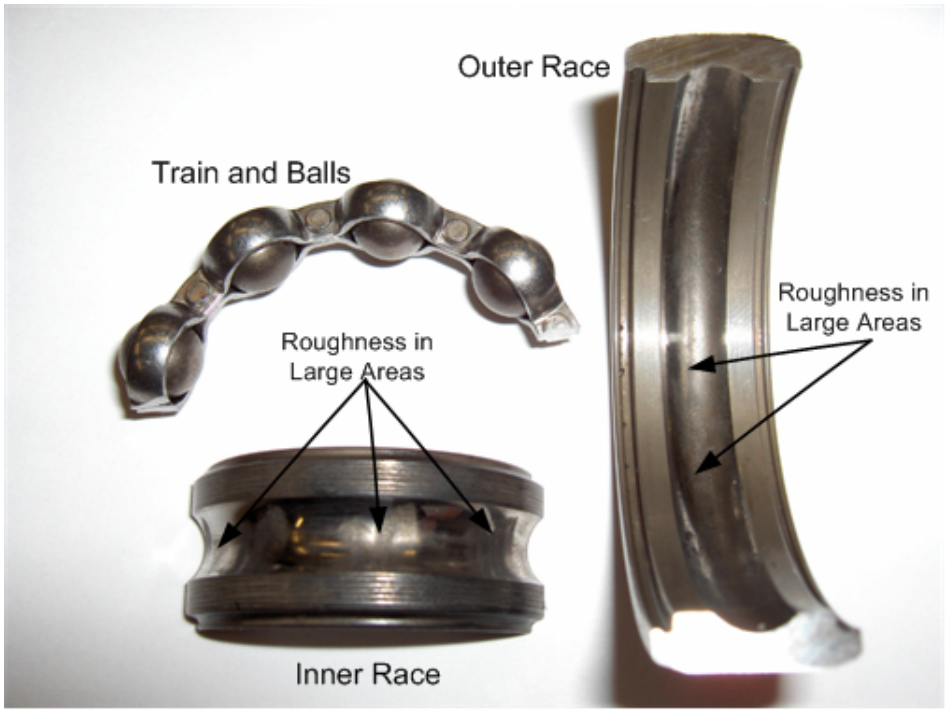

Fig. 3. A Bearing Damaged by a Generalized Roughness Fault.

disassembling, reassembling, remounting, and realigning the test motor significantly alters the current and vibration characteristics of the machine. This biases the experimental data, rendering them invalid for use in many bearing condition monitoring schemes. The drastic variations in machine vibration and stator current can result simply from the act of removing and reinstalling the same bearing [38]. In a research setting, these variations will appear every time test bearings are interchanged. This can potentially conceal fault signatures, contribute to misleading results, or add difficulty and confusion to the process of evaluating certain bearing condition monitoring schemes. Therefore, there is a definite need for a method that facilitates an online, in-situ failure process to effectively evaluate these condition monitoring methods and conduct bearing failure research.

2. Bearing Faults Generated by Shaft Currents

The tendency for shaft currents to cause bearing failures in actual installations has been studied by many scholars [38, 39, 40]. Studies indicate that there are several mechanisms by which bearings are damaged by shaft currents. However, the most common and most destructive is EDM. For EDM damage to occur, the rolling elements must be separated from the raceways by a thin film of lubricant. This film of lubricant serves as a dielectric and allows the bearing to behave as a capacitor. When the voltage across the bearing exceeds the dielectric strength of the grease, EDM occurs and pits are etched on the raceways and rolling elements.

Research indicates that a healthy bearing will possess a film of lubrication ranging from 0.2 to 2.0 μm thick at normal operating speeds. Given this thickness of lubrication, EDM currents can be caused by the 60 Hz shaft voltages with magnitudes as low as 0.2 to 2 V [41]. Another study suggests that it is not the magnitude of the EDM current, but rather the current density within the bearing that directly

determines the rate of failure [40]. The purpose of this research is not to explore and explain the mechanisms by which shaft currents cause bearing failures. This research uses shaft currents as means for experimentally generating online bearing faults.

3. Experimental Setups for In-situ Bearing Damage

a. Induction Motors and Loads Utilized

In this research, 3HP, 3 Phase, 230V induction motors, manufactured by Marathon Electric Company, are tested. A Delta VFD-B voltage source inverter (VSI) is used. Two test beds, one loaded by a synchronous generator, the other loaded by a gearbox, are used for different experimental purposes.

In the first test bed, a synchronous generator is used to load the induction motor. Figure 4 shows a photograph a schematic diagram of this test bed. The synchronous generator of this research is obtained by modifying a Delco Remy CS-130 Lundell automotive alternator. In order to utilize a general synchronous generator, the voltage regulator and the three phase rectifier are removed from this alternator [42]. A field excitation DC current fed to the rotor coil is provided by an external power supply. An Agilent HP E3631A power supply is chosen due to its availability in the laboratory. In addition, the power supply is powered by a single phase, 120V power line from a power outlet, while the in-situ bearing damage circuit uses separate power lines. Therefore, the high bearing damage current does not affect the proper operation of the power supply.

The generator used produces three phase AC voltage and the output power is consumed by a bank of three resistors. The electrical load consists of three OHMITE D225-ND power resistors, a piece of wooden plate, and low resistivity stranded 8AWG wires. Each of the power resistors has 225W power rating and 5Ω resistance. Hence,

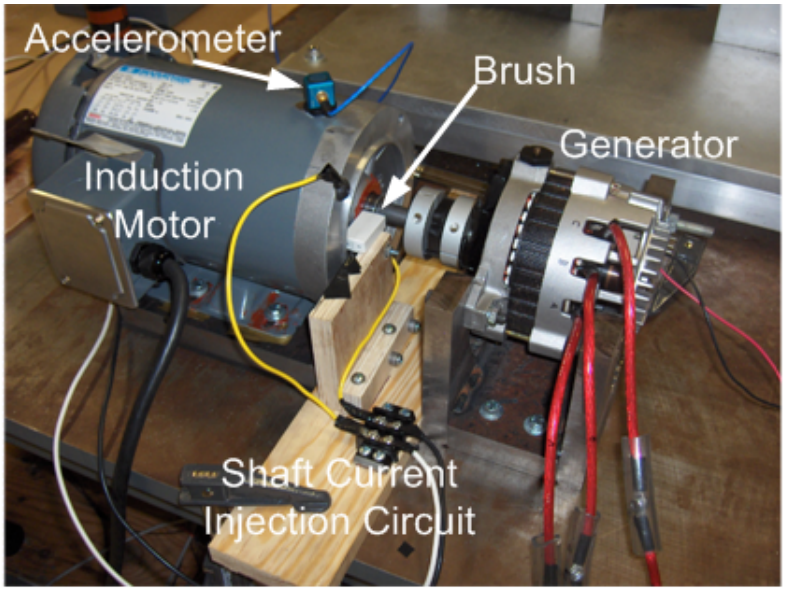

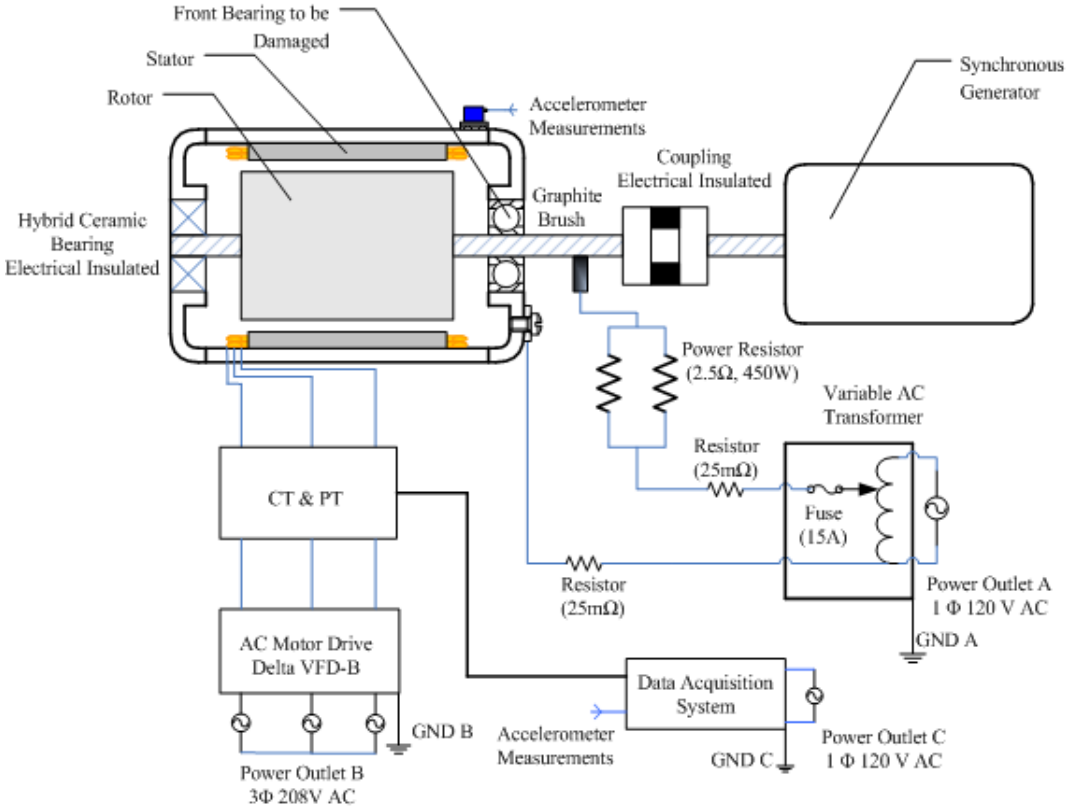

Fig. 4. Experimental Setup of the Motor-Generator Test-bed.

the maximum current that the power resistor can carry is about 6.7A. The required power rating is initially estimated based on the test results of the alternator. The resistors are mounted on the wooden plate, which also serves as a heat insulator. The resistors are wired to form a delta winding. The three terminal connections of the delta winding are connected to the three armature terminals.

In the second test bed, the induction motor is loaded by a gearbox, which is shown in Figure 5. This test bed is used to test the proposed bearing fault detection scheme using the VSI under speed feedback control. In this test bed, the Delta VFD-B VSI is set to V/Hz closed-loop control mode. An ACCU 260 encoder is used to close the speed feedback loop. This encoder cannot be placed on the first test bed because of limitation on the generator shaft length. On the other hand, the gearbox cannot endure long running time; therefore, different experimental procedures are used in closed loop tests, which are presented in Chapter IV.

The easy availability of the induction motor, the gearbox, the alternator, and their internal replacement components in the market, the small size, and the suitable output power rating are some of the main reasons for the experimental setup choices.

b. Sensors and Data Acquisition System

Induction motor line voltages and line currents are measured by LAH 25-NP current transducers and LV 25-P potential transducers, respectively. A PIEZOTRONICS three axis shear accelerometer is used for motor vibration sensing. This accelerometer is capable of measuring ±50 G, peak gravitational acceleration, with the sensitivity of 100mV/G from 0.2Hz up to 5000Hz. It is mounted on the top of the induction motor bearing that is damaged during the experiment.

The data acquisition hardware consists of a National Instruments (NI) PCI-6070E DAQ card, a NI SCXI-1531 8 channel accelerometer input module, a NI

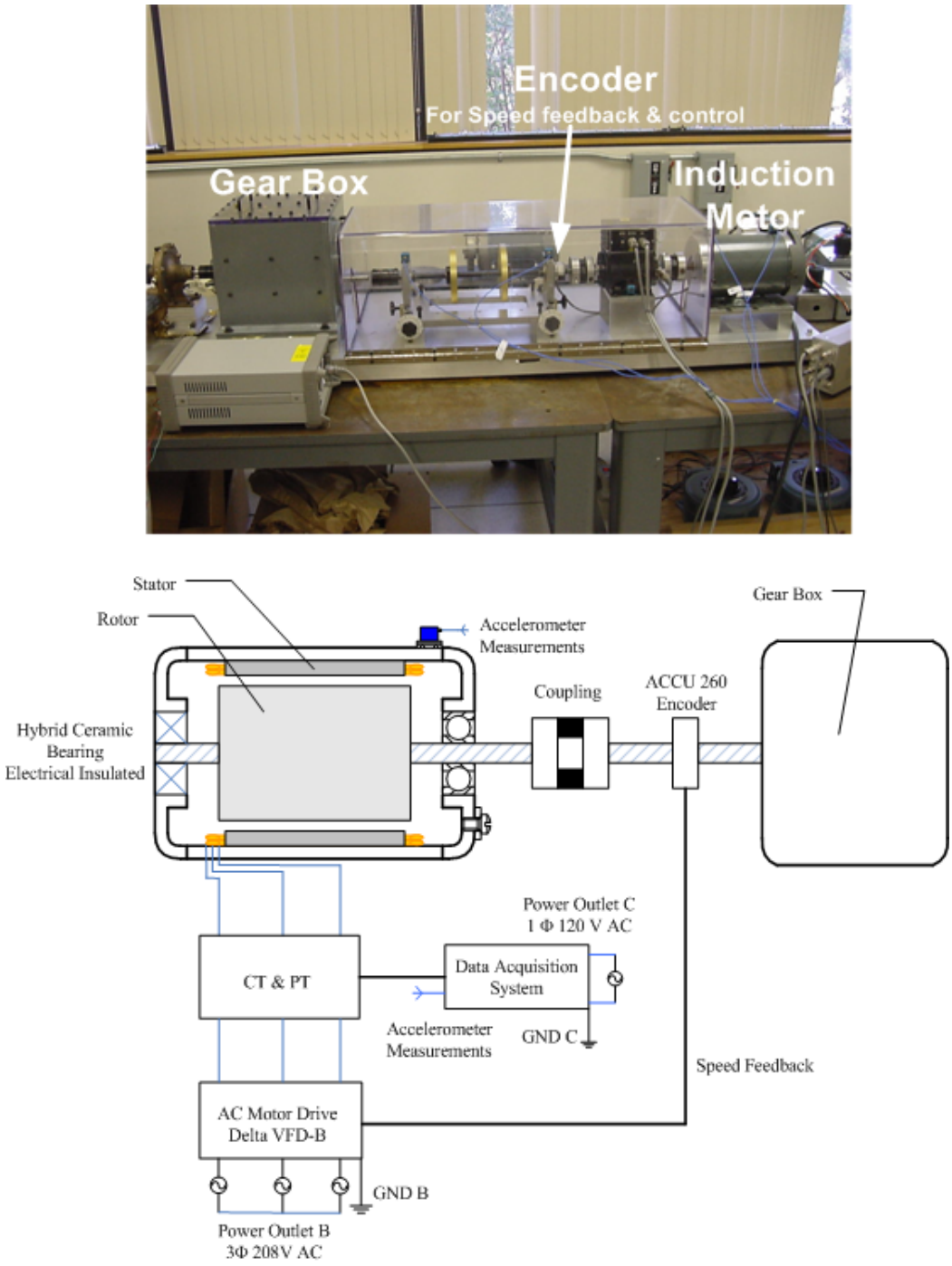

Fig. 5. Experimental Setup of the Motor-Gearbox Test-bed.

SCXI-1141 8 channel low pass filter module, and a SCXI-1305 AC/DC coupling BNC terminal block. The DAQ card has the capability of sampling 16 channel analog inputs with 12 bit hardware and 16 bit software resolution. The sampling mode is set to be multiplexed. The accelerometer input module has a built-in 4-pole Bessel low pass filter, whose bandwidth is set to 5000 Hz, the same as the bandwidth of the accelerometer. The SCXI-1141 low pass filter module has a built-in 8th order elliptical filter whose cutoff frequency is automatically set by the DAQ card. Low pass filtering is required to avoid aliasing. The BNC terminal block is plugged into the NI SCXI 1141 module.

A Virtual Instrument (VI) program that runs under the NI LabView ver. 6.1.4 saves the nine channels (three voltages, three currents and three axis vibration signals) of the experimental measurements into data files. The sampling rate, the number of sampled points, can be varied according to the needs of the experiments.

c. Experimental Setup for Shaft Current Injection

The test motor has a type 6203 fan-side bearing and a type 6205 load-side bearing. In the experimental method used in this research, a new 6205 bearing is placed in the test motor and AC currents are injected into the motor shaft to damage this bearing. The shaft current setup is depicted in Figure 4. In this setup, an external voltage source is applied to the motor shaft via a carbon brush. This causes a current to flow from the shaft through the load-side bearing. Two power resistors are placed in series with the voltage source to limit the shaft current. The 6203 fan-side bearing is a hybrid ceramic bearing, which is electrically insulated from the stator so that the shaft current is forced to flow from the shaft through the load-side test bearing to reach the stator frame.

The source providing the shaft voltage is a single-phase, variable transformer

supplied by 120V 60Hz utility power. This frequency and voltage level are chosen because of convenience and availability.

The magnitude of the shaft current applied to the test motor remains constant for a given experiment. The injected current values can be chosen between 0 to 14A, the maximum allowable current for the current injecting circuit. The shaft current produce voltage drops across the bearing and the brush, ranging from 0 to 3V at the time of injection. When the bearing is close to severe failure, it is observed that this voltage value increases with the degradation of the bearing since the grease film thickness decreases after the occurrence of the EDM. To damage the bearing, this voltage value should be larger than 1.8V in this experimental setup.

The severity of bearing failure is not affected by the magnitude of the shaft current. This observation agrees with the assertions made in [38]. However, the magnitude of the shaft current was found to have some relationship with the failure time of the bearing, which is different than the assertions made in [38].

In industry, two types of greases are used for bearing lubrication. One is the high resistivity mineral oil greases (in MΩ resistance). These types of greases act as capacitances and produce EDM currents and arcing or fritting on discharge. The other is the low resistivity lithium greases. These kinds of greases act as resistances. Currents of 189 mA will cause these kinds of greases to decompose into lithium iron oxide, leading to increased wear and bearing failure [40]. In this research, high resistivity grease is used since the goal of conducted experiments is to accelerate the bearing damage and EDM is reported by other researchers as a good tool for this purpose.

Using this method, the amount of time it takes for a bearing to fail is variable and depends on many factors. The first factor is the magnitude of the shaft current. Another significant factor is the type and amount of grease in the bearing. Using the

shaft current method, as stated in [38], the average failure time for a new bearing with the factory fill of grease is approximately 2-3 weeks. In order to further reduce the amount of time required to reach failure, some of the grease is removed from each test bearing, before it is installed in the test motor. To accomplish this, each bearing is soaked in a degreasing solution to remove all of the grease. Later, the bearing is repacked with a known amount of grease that was removed from the bearing initially. The factory fill of grease varies widely depending on manufacturer, bearing size, and type of grease. Nevertheless, a typical factory fill was observed to be approximately 20%-40% by volume. The test bearings are repacked with an approximate fill of 3%-5% by volume. By carefully controlling the amount of grease in the bearing and the magnitude of the shaft current, the average failure time could be reduced to anywhere from 8 to 30 hours.

In this research, the bearing reaches in-situ failure without interrupting the operation of the motor. This experimental method produce artificially accelerated bearing faults, and it provides bearing fault data that are more representative of measurements obtained from an actual installation compared to data from off-line bearing faults. Since the time required for the bearing to fail is significantly less than the bearing's expected natural life, the failure process of many bearings can be documented and studied. Throughout the failure process, the stator voltages, currents, and machine vibration are sampled. The data can then be used to evaluate the performance of any bearing condition monitoring scheme.

C. Chapter Summary

In this chapter, causes of the bearing faults and failures are explained. Amplitude modulation relationships of bearing single point defects and general roughness faults

are discussed. The in-situ bearing damage experimental setups are described.

CHAPTER III

PROPOSED BEARING FAULT DETECTION METHOD

A. Overview of the Higher Order Spectrum

One of the most fundamental and useful tools in digital signal processing has been the estimation of the power spectra density (PSD) of discrete-time deterministic and stochastic processes. The available power spectrum estimation techniques may be considered in a number of separate classes, namely, conventional (or "Fourier type") methods, maximum-likelihood method of Capon with its modifications, maximum-entropy and minimum-cross-entropy methods, minimum energy, methods based on autoregressive (AR), moving average (MA) and ARMA models, and harmonic decomposition methods such as Prony, Pisarenko, MUSIC, and Singular Value Decomposition. Research in this area has also led to signal modeling, and to extensions to multi-dimensional, multi-channel, and array processing problems. Each one of the aforementioned techniques has certain advantages, and limitations not only in terms of estimation performance, but also in terms of computational complexity. Therefore, depending on the signal environment, one has to choose the most appropriate method [43].

In power spectrum estimation, the process under consideration is treated as a superposition of statistically uncorrelated harmonic components and the distribution of power among these frequency components is then estimated. Only linear mechanisms governing the process are investigated because phase relationships between frequency components are suppressed. The information contained in the power spectrum is essentially present in the autocorrelation sequence. This is sufficient for the complete statistical description of a Gaussian process of known mean. However, there are prac-

tical situations where one must look beyond the power spectrum (autocorre1ation) to obtain information regarding deviations from Gaussianness and presence of non-linearities in the system that generates the signals. Higher order spectra (also known as polyspectra), defined in terms of higher order cumulants of the process, do contain such information [43]. Particular cases of higher order spectra are the third-order spectrum also called the bispectrum which is, by definition, the Fourier transform of the third-order cumulant sequence, and the trispectrum (fourth-order spectrum), which is the Fourier transform of the fourth-order cumulant sequence of a stationary random process. The power spectrum is, in fact, a member of the class of higher order spectra, i.e., it is the second-order spectrum.

1. Motivation for Using Higher Order Spectra in Fault Detection

The general motivation behind the use of higher order spectra in signal processing is threefold: 1) to extract information due to deviations from Gaussianness, 2) to estimate the phase of non-Gaussian parametric signals, and 3) to detect and characterize the nonlinear properties of mechanisms that generate time-series via phase relationships of their harmonic components [43].

In this research, the motivation for using higher order spectra is based on the fact that the nonlinear properties of mechanisms can be characterized via phase relationships of their harmonic components. Using the phase relation information between harmonic components, some motor faults can be detected.

In this research, the amplitude modulation detector is developed from the concept of the bispectrum. In the following section, the bispectrum estimation is reviewed.

2. Bispectrum Estimation

Bispectrum is one of the polyspectra, which is widely used in identifying the phase relationships between harmonic components.

Let $x(n)$ be a stationary, discrete, zero-mean random process. In this case, its third order cumulant sequence $c(\tau_1, \tau_2)$ will be identical to its third moment sequence (see equation (A.4) in Appendix (A)). Thus,

$$c(\tau_1, \tau_2) = E[x(n)x(n+\tau_1)x(n+\tau_2)], \tag{3.1}$$

where $E[.]$ denotes the expectation. The bispectrum is defined as (see equation (A.6) in Appendix (A)),

$$B(\omega_1, \omega_2) = \sum_{\tau_1=-\infty}^{\infty} \sum_{\tau_2=-\infty}^{\infty} c(\tau_1, \tau_2) \exp[-j(\omega_1\tau_1 + \omega_2\tau_2)]. \tag{3.2}$$

When a finite set of observation measurements is given, two chief approaches have been used to estimate the bispectrum, namely, the conventional ('Fourier type') and the parametric approach, which is based on autoregressive (AR), moving average (MA), and ARMA models [43].

In the proposed method, phase relationships between harmonic components are desired. The advantage of using the conventional approach to bispectrum estimation is its ability to provide good estimates of the phase coupling at harmonically related frequency pairs [43]. Therefore, the conventional estimation approach is used in this research.

The conventional bispectrum estimation method can be classified into the following two classes [43]:

1) Indirect class of techniques, which are approximations of the definition of the

bispectrum given by,

$$R(m,l) = E[x(n)x(n+m)x(n+l)], \tag{3.3}$$

$$B(\omega_1,\omega_2) = \sum_{m=-\infty}^{\infty}\sum_{n=-\infty}^{\infty} R(m,l)\exp[-j(\omega_1 m + \omega_2 l)]. \tag{3.4}$$

where $R(m,l)$ denotes the third moment sequence of $x(n)$.

2) Direct class of techniques, which approximate an equivalent definition of the bispectrum described by,

$$B(k_1,k_2) = E[X(k_1)X(k_2)X^*(k_1+k_2)]. \tag{3.5}$$

where $X(k)$ is the DFT of $x(n)$.

B. Amplitude Modulation Detector

1. From Bispectrum to Amplitude Modulation Detector (AMD)

The bispectrum estimator searches only for the presence of a summation frequency, which can be seen clearly from equation (3.5). However, bearing fault signature frequencies and the supply fundamental frequency are modulated as $|f_e \pm m f_v|$. This modulation relationship not only contains a summation relationship, but also contains a subtraction relationship. Assume two biased signals as follows,

$$x_1(n) = A + \cos(2\pi 60 n + \phi_1) \tag{3.6}$$

$$x_2(n) = B + \cos(2\pi 20 n + \phi_2) \tag{3.7}$$

where, ϕ_1 and ϕ_2 are arbitrary phase angles. The multiplication result of these two signals is,

$$\begin{aligned} x(n) &= x_1(n)x_2(n) \\ &= AB + B\cos(2\pi 60n + \phi_1) + A\cos(2\pi 20n + \phi_2) \\ &\quad + \cos(2\pi 60n + \phi_1)\cos(2\pi 20n + \phi_2) \\ &= AB + B\cos(2\pi 60n + \phi_1) + A\cos(2\pi 20n + \phi_2) \\ &\quad + \frac{1}{2}\cos(2\pi 80n + \phi_1 + \phi_2) + \frac{1}{2}\cos(2\pi 40n + \phi_1 - \phi_2). \end{aligned} \tag{3.8}$$

In this signal, the 20Hz and 60Hz components are modulated with each other. This modulation relationship can be detected using the phase coupling property. However, the bispectrum not only correctly identifies that the 80Hz is produced by the 20Hz and 60Hz components, but it also incorrectly suggests that the 20Hz and the 40Hz components are interacting to generate the 60Hz component (i.e., $60 = 20+40$), shown in Figure 6(a). This makes the bispectrum less useful in finding the amplitude modulation relationship.

In order to correctly identify the modulation relationship between frequency components, a modified bispectrum detector, used by Stack in vibration analysis [22], is utilized. This Amplitude Modulation Detector (AMD) is defined as follows,

$$\widehat{AMD}(k_1, k_2) = E[X(k_1 + k_2)X(k_1 - k_2)X^*(k_1)X^*(k_1)]. \tag{3.9}$$

Figure 6(b) shows the result for the example above using the AMD. By considering both sidebands created by amplitude modulation, AMD is more appropriate in finding the amplitude modulation components.

The amplitude modulation contains the plus and minus relationships. The above example shows the difference between the bispectrum and AMD estimators. In the

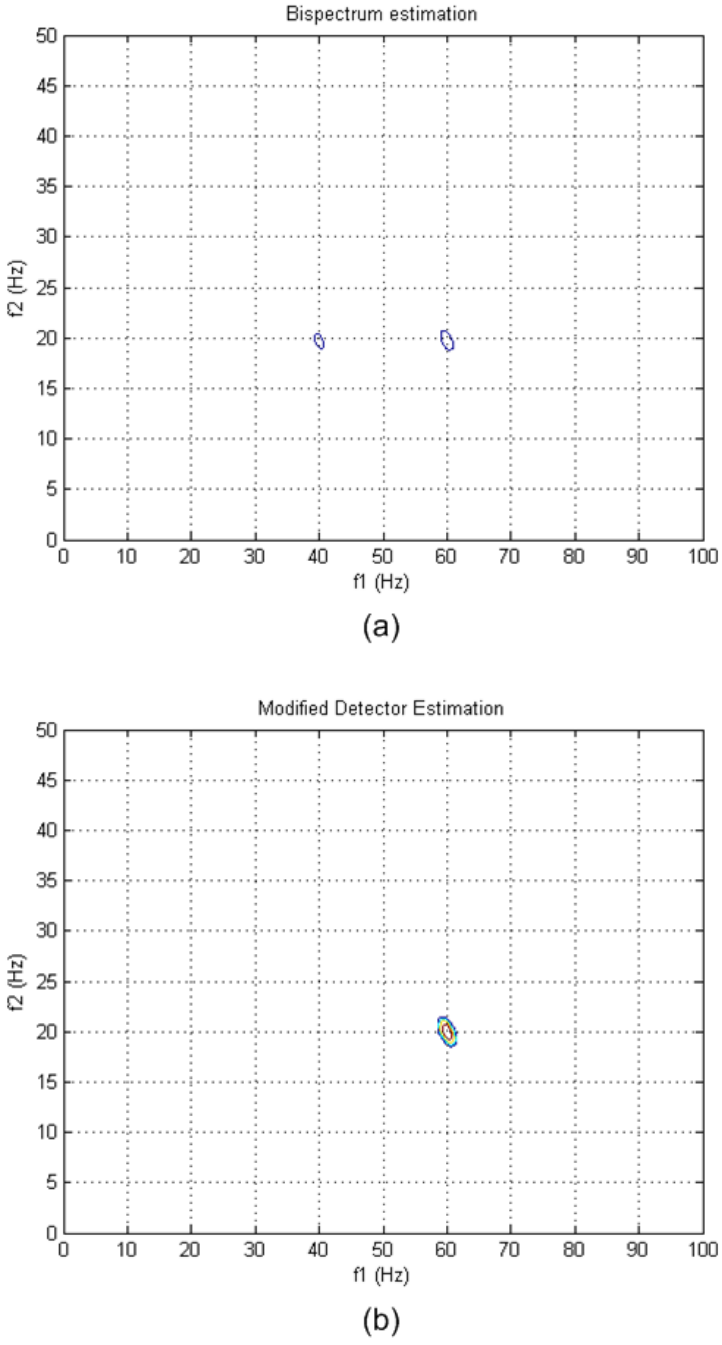

Fig. 6. (a)Incorrect Detection of the Amplitude Modulation Relationship Using Bispectrum; (b)Correct Detection of the Amplitude Modulation Relationship Using the AMD.

bispectrum estimator, only one of the two sidebands, the plus relationship is considered, while in the AMD estimator, both plus and minus relationships are considered. This makes the AMD a more effective amplitude modulation estimator.

Most importantly, in the bispectrum calculation, the career frequency, the modulated frequencies, and resulting sidebands are all used, while in AMD calculation, only the career frequency and resulting sidebands are needed. In this research, tools are desired to isolate spatial harmonics that are modulated by the fundamental frequency of the supply. In power systems, the fundamental frequency of the supply is not biased. Hence, in the signal spectrum, only the fundamental frequency and the sidebands appear, and the spatial harmonics that are modulated with the fundamental frequency do not show up actually. In these types of applications, the bispectrum estimator cannot be used because the information of the spatial harmonics are not available.

All in all, AMD is more suitable to detect the amplitude modulation relationships encountered in this application than the bispectrum.

2. Development of the Amplitude Modulation Detector

To implement the Amplitude Modulation Detector estimation in computers, two important issues need to be addressed. One is the frequency resolution, the other is the expectation procedure.

a. One Dimensional Amplitude Modulation Detector

The AMD spectrum is a two dimensional matrix. The frequency resolution of AMD can be calculated by $\Delta = \frac{f_s}{N}$ [43], where f_s is the sampling rate and N is the sample numbers. A good frequency resolution will lead to a rather huge AMD matrix, which cannot be implemented easily using computers.

In this research, we are interested only in the frequency components that are modulated with some specified frequency; for example, the supply fundamental frequency. Therefore, it is possible to use only one dimensional AMD estimation. That is to only calculate AMD spectra that are modulated with the supply fundamental frequency.

b. Expectation on AMD to Distinguish Fault Signature Frequencies

The Amplitude Modulation Detector works as the phase coupling detector. If frequency components have phases that are coupled with each other, AMD components calculated will have zero phases and peaks will be exhibited at those frequencies indicating this phase relationship. To illustrate this, let's expand equation (3.9) as,

$$E[|X(k_1+k_2)|e^{j\angle(k_1+k_2)}|X(k_1-k_2)|e^{j\angle(k_1-k_2)}|X^*(k_1)|e^{-j\angle(k_1)}|X^*(k_1)|e^{-j\angle(k_1)}]. \quad (3.10)$$

After grouping magnitude and phase terms together, we get,

$$E[|X(k_1+k_2)||X(k_1-k_2)||X^*(k_1)||X^*(k_1)|e^{j(\angle(k_1+k_2)+\angle(k_1-k_2)-\angle(k_1)-\angle(k_1))}]. \quad (3.11)$$

If there is phase coupling between the frequency components k_1 and k_2, then

$$\angle(k_1+k_2) = \angle(k_1) + \angle(k_2), \quad (3.12)$$

$$\angle(k_1-k_2) = \angle(k_1) - \angle(k_2). \quad (3.13)$$

By substituting equations (3.12) and (3.13) into equation (3.11), we see that the phase part of equation (3.11) equals zero. Equation (3.11) will equal the expected value of the product of the magnitudes. Therefore, if significant frequency components exist at k_1, k_1+k_2 and k_1-k_2, the detector will exhibit a peak at $AMD(k_1,k_2)$, indicating that frequencies k_1 and k_2 are modulated components.

On the other hand, if there is no phase coupling between the frequency components k_1 and k_2, equations (3.12) and (3.13) are not valid and AMD components calculated will have random phases from sample to sample. The expectation operation will then cause these AMD components to approach zero after a sufficient number of samples are averaged together. Therefore, the AMD spectrum will not exhibit a peak at $AMD(k_1, k_2)$ in the absence of phase coupling.

C. Effect of Power Supply

1. Power Supply Mains

For induction motors, stator voltages can be considered as the system input, while stator currents can be considered as the system output. As the system input, the stator voltage affects the stator current heavily, especially in the practical industrial environment where 'clean' power input is usually not available. Because of this, fault signature in stator current spectrum may be masked by frequency components originating from the stator voltage.

In the laboratory environment, clean power input can be provided using big transformers. However, in most practical industrial environments where the power supply system is not big enough compared with the rated power of machines, motor input voltages are affected by other equipment under the same power supply. Noise related harmonics produced in that equipment are interacting with motor input voltages and affect the stator currents in an unpredictable way.

One experiment was conducted to illustrate effects of noise related harmonics in motor voltages. In this experiment, the motor is in healthy condition with 0% load. Data are collected every minute.

The voltage Root Mean Square (RMS), the voltage imbalance, the voltage Total

Harmonic Distortion (THD), and the voltage Signal to Noise Ratio (SNR) are calculated for the data collected (see Appendix (B)). Table II lists test results for the first ten data sets. The experimental results show that the voltage RMS, imbalance, and THD values do not change much. But, the SNR changes more than 300%.

Table II. Motor Input Voltage Variables, Averaging Three Line Voltages

Data Sets	RMS	Imbalance (10^{-3})	THD (10^{-2})	SNR (10^{2})
1	3.611319	3.724	2.7888	5.596
2	3.610595	3.661	2.7753	5.605
3	3.612443	4.033	2.7867	4.423
4	3.612354	4.076	2.784	3.045
5	3.615914	4.172	2.7219	5.488
6	3.612687	4.048	2.782	5.219
7	3.610440	4.167	2.7599	3.715
8	3.611955	4.114	2.7715	1.553
9	3.610664	4.099	2.7761	1.313
10	3.611990	4.130	2.7658	2.026

In Figure 7, two voltage spectra, calculated from data 1 and 4 in Table II are shown. In these two voltage spectra, although differences in the integer harmonics are small, differences in the inter-harmonics are rather big. Corresponding current spectra are shown in Figure 8. It is obvious that the entire current noise level in data set 1 is lower than that in data set 4. It is reasonable to conclude that differences between two current spectra come from differences between two voltage spectra.

Bearing faults alter stator current inter-harmonics. If the effect of the voltage is

not removed, changes in the current spectrum caused by the voltage input may mask the fault information. This will be shown in the next chapter.

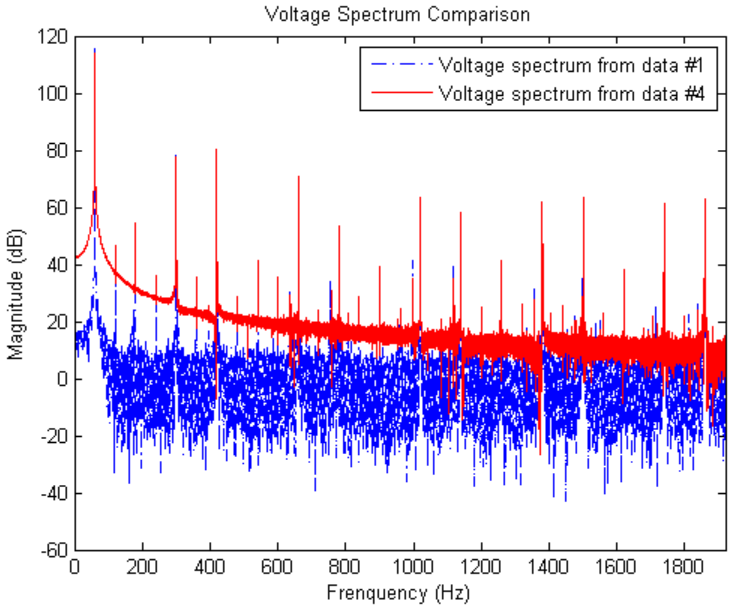

Fig. 7. Voltage Spectrum Comparison.

2. Voltage Source Inverter

a. Overview of Voltage Source Inverters

Voltage source inverters allow a variable frequency supply to be obtained from a dc supply. Figure 9 shows a VSI employing transistors. Any other self-commutated device can be used instead of a transistor. Generally, MOSFET is used in low voltage and low power inverters. IGBT (Insulated Gate Bipolar Transistor) and power transistors are used up to medium power levels. GTO (Gate Turn Off Thyristor) and IGCT (Insulated Gate Commutated Thyristor) are used for high power levels [44].

VSIs can be operated as a stepped wave inverter or a pulse width modulated

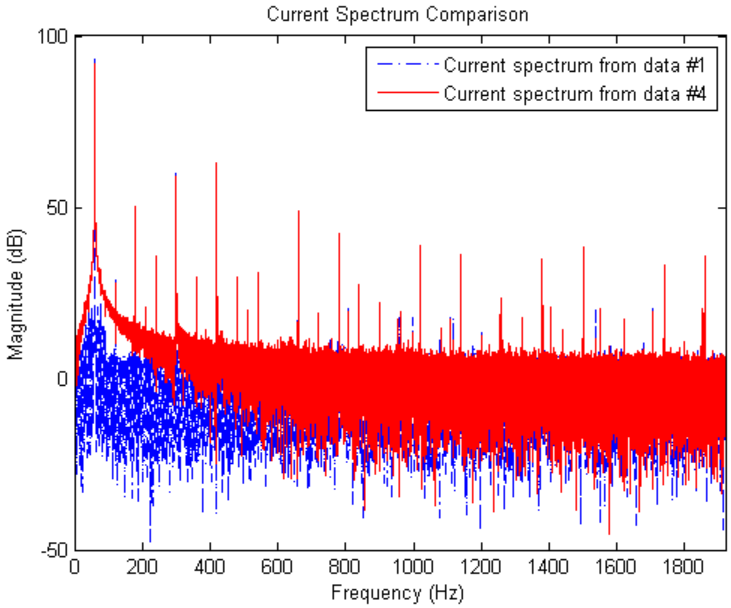

Fig. 8. Current Spectrum Comparison.

(PWM) inverter. When operated as a stepped wave inverter, transistors are switched in the sequence of their numbers with a time difference of T/6 and each transistor is kept on for the duration T/2, where T is the time period of one cycle. Frequency of inverter operation is varied by varying T and the output voltage of the inverter is varied by varying DC input voltage. When supply is DC, variable DC input voltage is obtained by connecting a chopper between DC supply and the inverter. When supply is AC, variable DC input voltage is obtained by connecting a controlled rectifier between AC supply and the inverter. A large electrolytic filter capacitor C is connected in the DC link to make inverter operation independent of the rectifier or chopper and to filter out harmonics in DC link voltage [44].

The main drawback of stepped wave inverter is the large harmonics of low frequency in the output voltage. When inverter is operated as a PWM inverter, har-

monics are reduced, low frequency harmonics are eliminated, associated losses are reduced, and smooth motion is obtained at low speeds. Figure 10 shows output voltage waveform for sinusoidal PWM. This voltage waveform is not pure sinusoidal, but a combination of square waves. Since output voltage can be controlled by PWM, no arrangement is required for the variation of input DC voltage [44]. Hence, the inverter can be directly connected when the supply is DC or through a diode rectifier when the supply is AC, as shown in Figure 9. In this research, a PWM inverter is used.

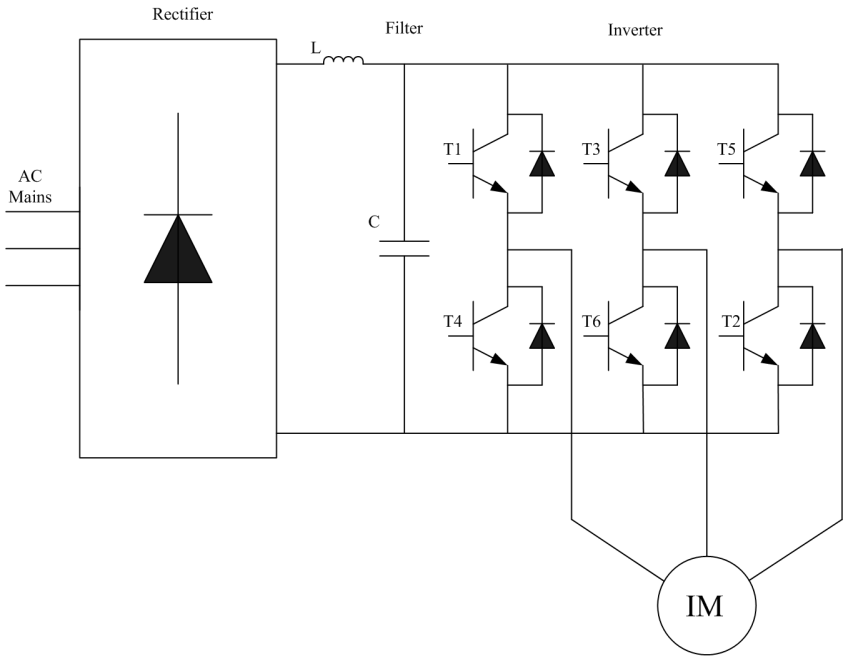

Fig. 9. VSI Controlled Induction Motor Drive.

b. Constant V/Hz Control for Induction Motors

For induction motor fault detection, inverter control schemes need to be investigated. Several control schemes are used in PWM voltage source inverters, the V/Hz control,

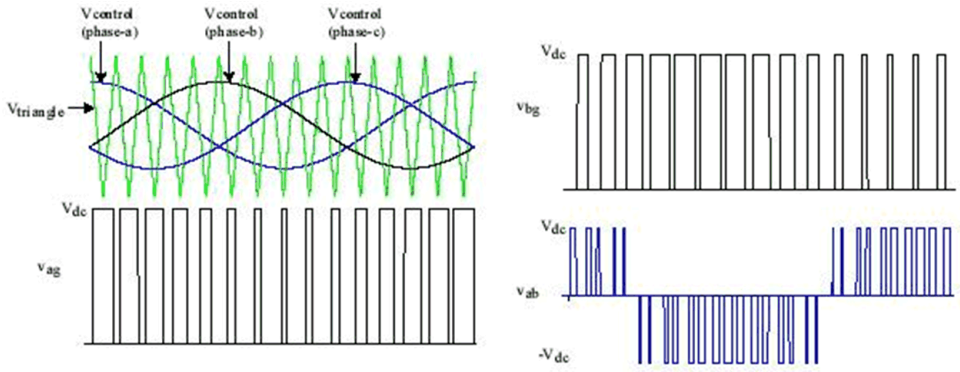

Fig. 10. Voltage PWM Wave Forms.

the Field Orientation Control (FOC), and the Direct Torque Control (DTC). The V/Hz control is used in this research because of its wide applicability in industry.

Assume the voltage applied to a three phase AC induction motor is sinusoidal $v(t) = V_M sin(\omega t)$, and neglect the voltage drop across the stator resistor. The flux ϕ in the core of the induction motor can be found from Faraday's Law [45],

$$v(t) = -N\frac{d\phi}{dt}, \tag{3.14}$$

$$\begin{aligned} \phi(t) &= \frac{1}{N}\int v(t)dt \\ &= \frac{1}{N}\int V_M \sin(\omega t)dt \\ &= -\frac{V_M}{\omega N}\cos(\omega t) \\ &= -\frac{V_M}{2\pi f N}\cos(\omega t), \end{aligned} \tag{3.15}$$

where N is the number of winding, V_M is the voltage magnitude and f is the frequency.

Induction motors are normally designed to operate near the saturation point on their magnetization curves, so the increase in flux due to a decrease in frequency will cause excessive magnetization currents to flow in the motor. To avoid excessive

magnetization currents, it is customary to decrease the applied stator voltage in direct proportion to the decrease in frequency whenever the frequency falls below the rated frequency of the motor.

From equation (3.15), it follows that if the ratio V/f remains constant with the change of f, then the flux remains constant too and the torque is independent of the supply frequency. In actual implementation, the ratio between the magnitude and frequency of the stator voltage is usually based on the rated values of these variables or motor ratings. However, when the frequency and, hence, the voltage are low, the voltage drop across the stator resistance cannot be neglected and must be compensated. At frequencies higher than the rated value, the constant V/Hz principle has to be violated in order to avoid insulation breakdown. The stator voltage must not exceed its rated value. This principle is illustrated in Figure 11.

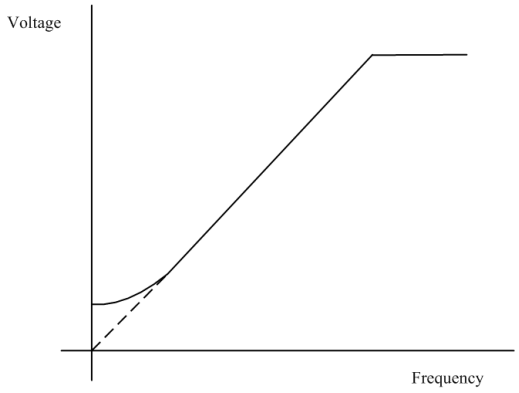

Fig. 11. Voltage versus Frequency under the Constant V/Hz Principle.

Since the stator flux is maintained constant, independent of the change in supply frequency, the torque developed depends on the slip speed [46]. So, by regulating the slip speed, the torque and speed of an AC induction motor can be controlled with the constant V/Hz principle.

Both open-loop and closed-loop control of the speed of an AC induction motor can be implemented based on the constant V/Hz principle. Open-loop speed control is used when accuracy in speed response is not a concern such as in HVAC (Heating, Ventilation, and Air Conditioning), fan, or blower applications. In this case, the supply frequency is determined based on the desired speed and the assumption that the motor will roughly follow its synchronous speed. Figure 12 shows how the frequency f and the output voltage V of the inverter are proportionately adjusted with the speed reference. The speed reference signal is normally passed through a filter that only allows a gradual change in the frequency f [46].

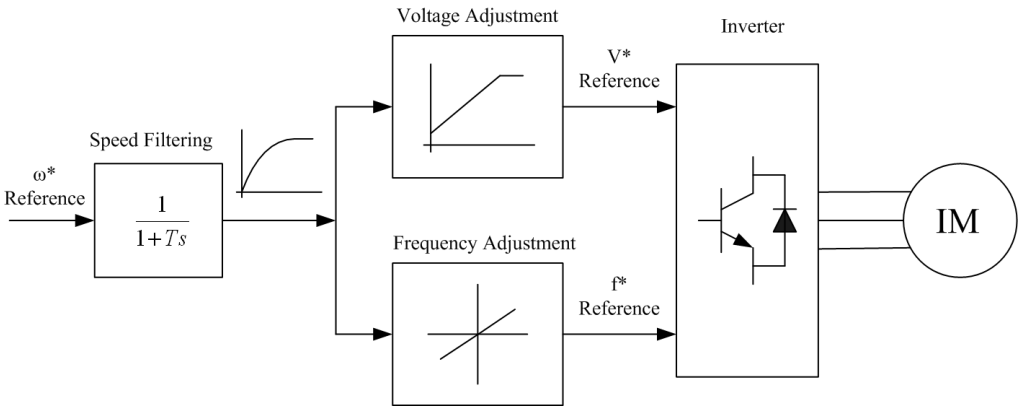

Fig. 12. Open-loop Constant V/Hz Controller.

When accuracy in speed response is a concern, closed-loop speed control can be implemented with the constant V/Hz principle through regulation of slip speed, as illustrated in Figure 13. In this scheme, the slip limiter is used so that the motor is allowed to follow the change in the supply frequency without exceeding the rotor current and torque limits. The motor speed is sensed and added to a limited speed error (or limited slip speed) to obtain the frequency.

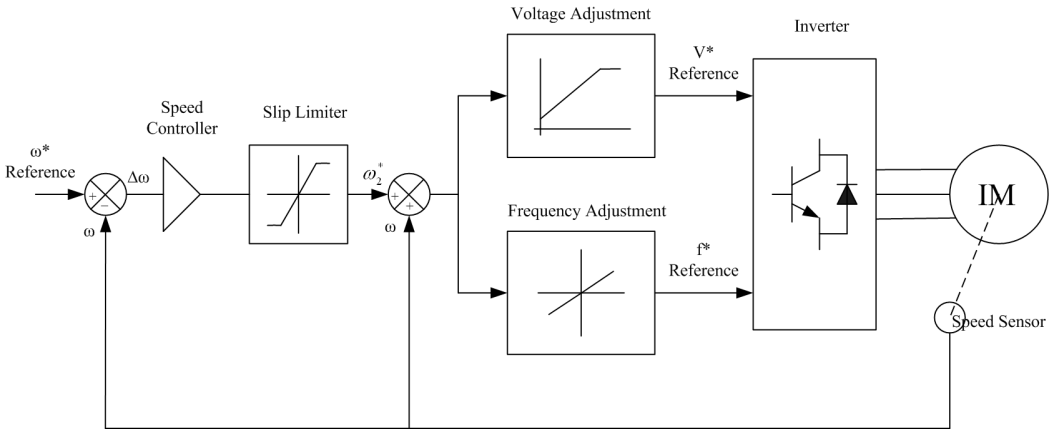

Fig. 13. Closed-loop Constant V/Hz Controller.

c. Motor Bearing Fault Detection under VSI Operation

Voltage source inverters are widely used in industry. When the motor is driven by a voltage source inverter, the motor input voltages are isolated from outside devices since most noise outside of the system usually can not pass through the DC line in the inverter, as shown in Figure 9. Hence, input voltage variations from supply mains do not affect stator currents in motors energized by VSI. However, fault detection of induction motors energized by VSI faces two problems,

- The symptoms of internal faults of induction motors may be masked by the control of the drive system.
- Harmonics from the inverter are much richer than that from power supply mains. This makes the fault detection difficult.

The control of the drive system affects the bearing fault detection in two aspects. One is the control scheme itself, the other is the speed feedback loop.

For voltage source inverters, controlled variables are finally utilized to adjust the voltage fundament frequency supplied by the VSI. In the proposed method, the current fundamental frequency, which comes from the voltage supplied by the VSI, is used for the AMD estimation. This fundamental frequency is adjusted according to the inverter speed set point and the speed feedback loop. For motors working in the steady state operation condition, the fundamental frequency does not change so that the VSI control schemes do not affect the bearing fault detection.

The bandwidth of the speed feedback loop usually is a degree of freedom set by the user. Extra frequency components may be introduced into current spectra because of the speed feedback loop. These frequency components are unpredictable. The closed-loop experiment conducted in this research show that the bearing fault signatures are not masked by the VSI speed feedback control.

The biggest problem in motor bearing fault detection using VSI is the rich harmonics. The VSI outputs are not pure sinusoidal, as shown in Figure 10. Inverters switching on and off produces large inter-harmonics in the voltage spectra. These inter-harmonics are injected into current spectra, which causes problems when trying to detect motor bearing faults.

The motor stator voltage and current spectra are shown in Figures 14 and 15. Also in these two figures, narrow frequency band spectra are shown so that inter-harmonics can be seen clearly. Because of these big inter-harmonics, motor bearing fault signatures may be masked. This is the main reason that very few papers have been published in the VSI driven motor fault detection area.

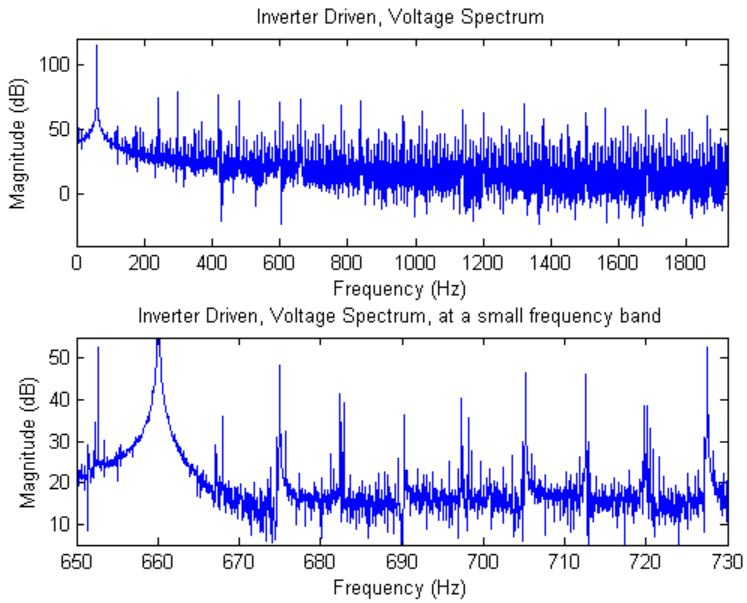

Fig. 14. Top: VSI Driven Voltage Spectrum; Bottom: Narrow Frequency Band of the Voltage Spectrum.

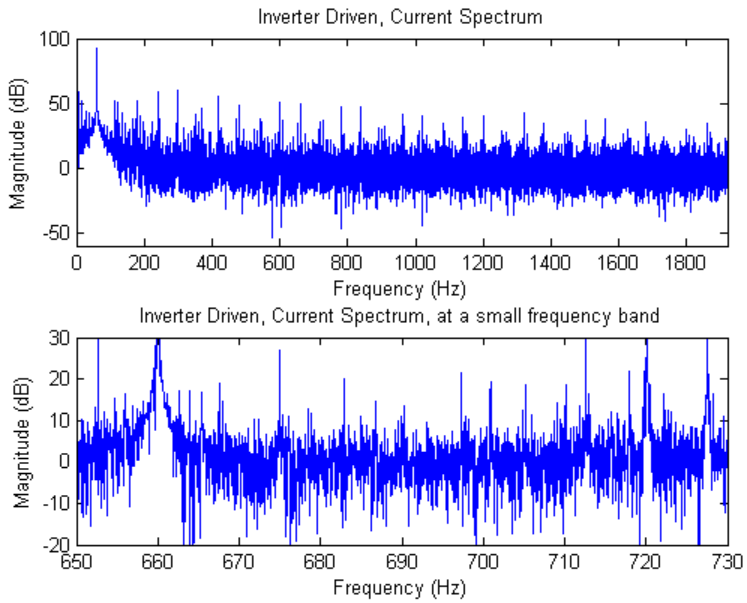

Fig. 15. Top: VSI Driven Current Spectrum; Bottom: Narrow Frequency Band of the Current Spectrum.

D. Electrical AMD Indicators

1. Modulation Model

General induction motor voltage equations in terms of machine variables can be expressed as,

$$v_{abcs} = r_s i_{abcs} + p\lambda_{abcs}, \tag{3.16}$$

$$v_{abcr} = r_r i_{abcr} + p\lambda_{abcr}. \tag{3.17}$$

where p is the derivative calculator; the s subscript denotes variables and parameters associated with the stator circuits, and the r subscript denotes variables and parameters associated with the rotor circuits; and,

$$(f_{abcs})^T = \begin{bmatrix} f_{as} & f_{bs} & f_{cs} \end{bmatrix},$$

$$(f_{abcr})^T = \begin{bmatrix} f_{ar} & f_{br} & f_{cr} \end{bmatrix}.$$

For a magnetically linear system, the flux linkages may be expressed,

$$\begin{bmatrix} \lambda_{abcs} \\ \lambda_{abcr} \end{bmatrix} = \begin{bmatrix} L_s & L_{sr}(\theta_m(t)) \\ L_{sr}^T(\theta_m(t)) & L_r \end{bmatrix} \begin{bmatrix} i_{abcs} \\ i_{abcr} \end{bmatrix}, \tag{3.18}$$

where $\theta_m(t)$ is the mechanical rotating angle of the rotor. The winding inductances, L_s, L_r and $L_{sr}(\theta_m(t))$ are complex functions of angular rotor positions and other machine design parameters. They are given in [47].

For a squirrel cage induction motor, $v_{abcr} = 0$. Substituting equation (3.18) into equations (3.16) and (3.17), we get,

$$v_{abcs} = r_s i_{abcs} + L_s(pi_{abcs}) + (pL_{sr}(\theta_m(t)))i_{abcr} + L_{sr}(\theta_m(t))(pi_{abcr}), \tag{3.19}$$

$$0 = r_r i_{abcr} + (pL_{sr}^T(\theta_m(t)))i_{abcs} + L_{sr}^T(\theta_m(t))(pi_{abcs}) + L_r(pi_{abcr}). \tag{3.20}$$

At steady state, equations (3.19) and (3.20) can be expressed in the time phasor form as follows,

$$\tilde{V}_s(t) = (r_s + j\omega_s L_s)\tilde{I}_s(t) + (j\omega_s L_{sr}(\theta_m(t)))\tilde{I}_r(t), \tag{3.21}$$

$$0 = j\omega_r L_{sr}^T(\theta_m(t))\tilde{I}_s(t) + (r_r + j\omega_r L_r)\tilde{I}_r(t). \tag{3.22}$$

The detailed derivation can be found in [47].

In equation (3.22), assuming that $(r_r + j\omega_r L_r)$ is invertible, the time phasor $\tilde{I}_r(t)$ can be expressed by,

$$\tilde{I}_r(t) = -\frac{j\omega_r L_{sr}^T(\theta_m(t))}{r_r + j\omega_r L_r}\tilde{I}_s(t). \tag{3.23}$$

Substituting equation (3.24) into equation (3.21), we have,

$$\tilde{V}_s(t) = (r_s + j\omega_s L_s + \frac{\omega_s\omega_r L_{sr}(\theta_m(t))L_{sr}^T(\theta_m(t))}{r_r + j\omega_r L_r})\tilde{I}_s(t). \tag{3.24}$$

Assuming $(r_s + j\omega_s L_s + \frac{\omega_s\omega_r L_{sr}(\theta_m(t))L_{sr}^T(\theta_m(t))}{r_r + j\omega_r L_r})$ is invertible, we obtain the following relationship between stator voltages and currents,

$$\tilde{I}_s(t) = [r_s + j\omega_s L_s + \frac{\omega_s\omega_r L_{sr}(\theta_m(t))L_{sr}^T(\theta_m(t))}{r_r + j\omega_r L_r}]^{-1}\tilde{V}_s(t). \tag{3.25}$$

$$\tilde{I}_s(t) = [Z(\theta_m(t))]^{-1}\tilde{V}_s(t). \tag{3.26}$$

In general, equation (3.26) is linear in terms of the voltages and currents. However, this relation is representative of a non-linear system, i.e. a modulator, as the inverse of the impedance is made of time-varying and nonlinearly coupled terms. Assuming the voltage to be a single frequency signal, the current will be composed of frequencies beyond the single input voltage frequency, made up of modulated components. This frequency shifts are indicative of a nonlinear system.

Based on this, an induction motor at steady state can be modeled as a modulator as shown in Figure 16, where $u(n)$ is the system input, the stator voltage; $a(n)$ is an

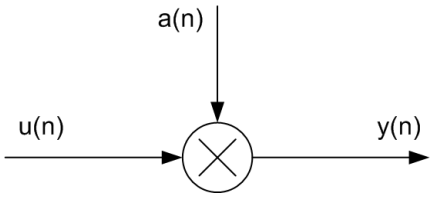

Fig. 16. The Induction Motor Modulator Model.

unknown signal which contains the spatial frequencies of the motor, represented by $[Z(\theta_m)]^{-1}$; and $y(n)$ is the system output, the stator current.

Assuming $a(n)$ to be periodic, it can be written as,

$$a(n) = A_0 + \sum_{i=1}^{k} A_i \cos(\omega_i n + \phi_i). \tag{3.27}$$

The system output is given by,

$$y(n) = a(n)u(n) = [A_0 + \sum_{i=1}^{k} A_i \cos(\omega_i n + \phi_i)]u(n). \tag{3.28}$$

In the frequency domain, the corresponding system output is,

$$Y(\omega) = A_0 U(\omega) + \frac{1}{2}\sum_{i=1}^{k} A_i[e^{-j\phi_i}U(\omega+\omega_i) + e^{j\phi_i}U(\omega-\omega_i)]. \tag{3.29}$$

A special frequency phasor is defined as,

$$a_i \equiv A_i e^{-j\phi_i}. \tag{3.30}$$

Equation (3.29) can be written as,

$$Y(\omega) = A_0 U(\omega) + \frac{1}{2}\sum_{i=1}^{k}[a_i U(\omega+\omega_i) + a_i^* U(\omega-\omega_i)]. \tag{3.31}$$

The AMD estimation can be re-written as,

$$\widehat{AMD}(\omega) \;=\; Y(\omega_0+\omega)Y(\omega_0-\omega)Y^*(\omega_0)Y^*(\omega_0). \tag{3.32}$$

where ω_0 is the fundamental supply frequency.

Based on equation (3.31), equation (3.32) can be written as,

$$Y^*(\omega_0) = A_0 U^*(\omega_0) + \frac{1}{2}\sum_{i=1}^{k}[a_i^* U^*(\omega_0 + \omega_i) + a_i U^*(\omega_0 - \omega_i)], \tag{3.33}$$

$$Y(\omega_0 + \omega) = A_0 U(\omega_0 + \omega) + \frac{1}{2}\sum_{i=1}^{k}[a_i U(\omega_0 + \omega + \omega_i) + a_i^* U(\omega_0 + \omega - \omega_i)], \tag{3.34}$$

$$Y(\omega_0 - \omega) = A_0 U(\omega_0 - \omega) + \frac{1}{2}\sum_{i=1}^{k}[a_i U(\omega_0 - \omega + \omega_i) + a_i^* U(\omega_0 - \omega - \omega_i)]. \tag{3.35}$$

Let T_1 and T_2 be the summation terms in equations (3.34) and (3.35),

$$T_1(\omega) = \sum_{i=1}^{k}[a_i U(\omega_0 + \omega + \omega_i) + a_i^* U(\omega_0 + \omega - \omega_i)], \tag{3.36}$$

$$T_2(\omega) = \sum_{i=1}^{k}[a_i U(\omega_0 - \omega + \omega_i) + a_i^* U(\omega_0 - \omega - \omega_i)]. \tag{3.37}$$

Obviously, these terms depend on the system input.

Suppose the system input contains a fundamental, the fundamental's integer harmonics, and noise. The representation of the system input in the frequency domain is as follows,

$$U(\omega) = \begin{cases} s_1, & \omega = \omega_0 \\ s_2, & \omega = 2\omega_0 \\ s_3, & \omega = 3\omega_0 \\ \vdots & \vdots \\ s_p, & \omega = p\omega_0 \\ m, & \forall\omega \neq l\omega_0 \end{cases} \tag{3.38}$$

where ω_0 and s_1 are the fundamental frequency and its magnitude, respectively; $s_2, s_3, \ldots, s_p$ are magnitudes of integer harmonics; m is the noise level, and $l = 1, 2, ..., p$.

Generally, for induction motor supply, the magnitude of the fundamental fre-

quency is far larger than the magnitude summation of all other frequencies. Hence, we have,

$$|s_1| >> \sum_{i=2}^{p} |s_i| + \int |m| d\omega. \tag{3.39}$$

At any frequency ω_s, $T_1(\omega_s)$ can be calculated based on the input, equation (3.38), as follows,

$$\begin{aligned} T_1(\omega_s) &= \sum_{i=1}^{k} [a_i U(\omega_0 + \omega_s + \omega_i) + a_i^* U(\omega_0 + \omega_s - \omega_i)] \\ &= a_s^* U(\omega_0) + a_s U(\omega_0 + 2\omega_s) + \sum_{i=1}^{s-1} [a_i U(\omega_0 + \omega_s + \omega_i) + a_i^* U(\omega_0 + \omega_s - \omega_i)] \\ &\quad + \sum_{i=s+1}^{k} [a_i U(\omega_0 + \omega_s + \omega_i) + a_i^* U(\omega_0 + \omega_s - \omega_i)]. \end{aligned} \tag{3.40}$$

Because $U(\omega)$ can take values from s_1 to s_k and m, the resulting expressions for equation (3.40) are not unique. Using b_i, c_{ji}, and Q_i as dummy variables, equation (3.40) can be written as,

$$\begin{aligned} T_1(\omega_s) &= a_s^* s_1 + b_1 m + b_2 s_2 + b_3 s_3 + \ldots + b_k s_k \\ &\quad + \sum_{i=1}^{Q1} c_{1i} m + \sum_{i=1}^{Q2} c_{2i} m + \sum_{i=s+1}^{Q3} c_{3i} m + \sum_{i=s+1}^{Q4} c_{4i} m \\ &= a_s^* s_1 + \sum_{i=2}^{p} b_i s_i + m(b_1 + \sum_{i=1}^{Q1} c_{1i} + \sum_{i=1}^{Q2} c_{2i} + \sum_{i=s+1}^{Q3} c_{3i} + \sum_{i=s+1}^{Q4} c_{4i}) \\ &= a_s^* s_1 + \sum_{i=2}^{p} b_i s_i + c_i m, \end{aligned} \tag{3.41}$$

where $c_i = b_1 + \sum_{i=1}^{Q1} c_{1i} + \sum_{i=1}^{Q2} c_{2i} + \sum_{i=s+1}^{Q3} c_{3i} + \sum_{i=s+1}^{Q4} c_{4i}$; a_i's are spatial harmonics in $a(n)$; b_1 and c_{ji} can take values among 0, a_i, a_i^* or summation of a_i and a_i^*; and $b_2, b_3, ..., b_k$ can take values among 0, a_i and a_i^*.

Compared to the magnitude of the fundamental frequency, a_i, b_i, c_{ji}, and m are very small. Further, assume a_s, b_i, and c_i have comparable values. Using equation

(3.39), equation (3.41) becomes,

$$T_1(\omega_s) \approx a_s^* s_1. \tag{3.42}$$

Following the same procedure, T_2 can be written as,

$$T_2(\omega_s) \approx a_s s_1. \tag{3.43}$$

Signature frequencies caused by bearing generalized faults are distributed in wide frequency bands. They are mostly located in inter-harmonics. Integer harmonics of the supply fundamental frequency usually have big magnitudes compared with other inter-harmonics. In order to detect variations in inter-harmonics, the integer harmonics must be removed from the final AMD spectrum. Hence, the integer harmonics of the fundamental frequency are not present in the spectrum of $a(n)$. Hence,

$$\omega_i \neq q\omega_0, \quad q = 1, 2, ..., p, \tag{3.44}$$

$$U(\omega_0 \pm \omega_i) = m, \tag{3.45}$$

where ω_i's are spatial harmonics in $a(n)$. Based on the above simplification, at frequency ω_s, equations (3.33), (3.34), and (3.35) can be re-written as,

$$\begin{aligned} Y^*(\omega_0) &= A_0 s_1^* + \frac{1}{2} m^* \sum_{i=1}^{k} [a_i^* + a_i] \\ &= A_0 s_1^* + m^* \sum_{i=1}^{k} A_i \cos\phi_i \\ &\approx A_0 s_1^*. \end{aligned} \tag{3.46}$$

The term, $m^* \sum_{i=1}^{k} A_i \cos\phi_i$, can be ignored compared with $A_0 s_1^*$, so,

$$\begin{aligned} Y(\omega_0 + \omega_s) &= A_0 m + \frac{1}{2} T_1 \\ &\approx A_0 m + \frac{1}{2} a_s^* s_1 \end{aligned}$$

$$\approx \frac{1}{2}a_s^* s_1, \tag{3.47}$$

and,

$$\begin{aligned} Y(\omega_0 - \omega_s) &= A_0 m + \frac{1}{2}T_2 \\ &\approx A_0 m + \frac{1}{2}a_s s_1 \\ &\approx \frac{1}{2}a_s s_1. \end{aligned} \tag{3.48}$$

The composite AMD estimator at frequency ω_s becomes,

$$\begin{aligned} \widehat{AMD}(\omega_s) &= Y(\omega_0 + \omega_s)Y(\omega_0 - \omega_s)Y^*(\omega_0)Y^*(\omega_0) \\ &\approx \frac{1}{4}A_0^2|a_s|^2|s_1|^4. \end{aligned} \tag{3.49}$$

Various forms of this AMD indicator are used in this research to obtain the experimental results presented in later chapters.

E. Mechanical Vibration Indicator

In this research, mechanical vibration signals are also collected with the electrical signals. The vibration signals are used for two purposes.

First, vibration signals are used to monitor the bearing damage process. During the experiment, vibration level is changing with the deterioration of the bearing. By looking at the vibration level, the experiment can be controlled.

Second, the vibration fault indicator is used as a reference for the fault detection capability of the electrical AMD indicator.

In this research, the aggregate RMS values of the vibration signals are calculated as the vibration indicator.

The RMS of vibration signal is defined as follows,

$$Indicator\_vib = \sqrt{\frac{1}{N}\sum_{i=1}^{N} x(i)^2}, \tag{3.50}$$

where $x(i)$ is the vibration sample and N is the total number of samples used in the RMS calculation.

F. Chapter Summary

Bearing failures can be captured in frequencies that are modulated with the fundamental frequency and all other harmonics of the supply. This modulation relationship can be isolated using the phase coupling between the bearing fault frequencies and the supply fundamental frequency. An Amplitude Modulation Detector (AMD), which is developed from the higher order spectrum estimation, can correctly capture the phase coupling and isolate these modulation relationships. This is the proposed approach for this research.

In this chapter, estimation procedures of the AMD are introduced. Effects of supply voltages on stator currents are discussed both for motors energized by power supply mains and VSI type drives. Based on this, the modulation model and electrical AMD indicator are derived. Moreover, a mechanical vibration indicator is also provided. This indicator is used to control the bearing damage experiments, and as a reference for testing the fault detection capability of the electrical AMD indicator.

CHAPTER IV

EXPERIMENTAL RESULTS

Experimental results are presented in this chapter. These experiments are grouped into six categories. The first group of experiments are used to test the effect of the shaft currents on the electrical indicator performance; the second group of experiments are used to test the effect of different load levels on the same indicators. Healthy bearing experiments are the third group used to test the variations of the healthy electrical indicators. Bearing damage experiments for motors energized by power supply mains and VSI are the fourth and fifth group, respectively. Finally, the effect of bearing faults on motor conversion efficiency is also presented in this chapter.

A. Effect of Shaft Currents on Indicator Performance

In this research, the motor load-side bearing is damaged using injected shaft currents. The effect of shaft currents on the indicator has to be investigated since this is a large current, around 6 to 12 A, compared with the motor stator current. However, it is difficult to exactly identify the effects of the this shaft currents on the motor magnetic field. In this research, indicators with shaft currents and without shaft currents are compared so that the effect of shaft currents on the fault indicator can be identified. Moreover, this comparison work is focused on the early stage of bearing damage because we are interested in detecting incipient faults.

Comparison experiments are conducted as follows: (1) collect healthy data; (2) inject the shaft current for around one hour so that the bearing is slightly damaged. This procedure is essential. In order to make comparisons, indicators have to deviate from the healthy range; (3) collect one hour of data with the shaft current; (4) remove the shaft current and collect one hour data; (5)repeat step (3) and step (4). These

procedures are summarized in Figure 17.

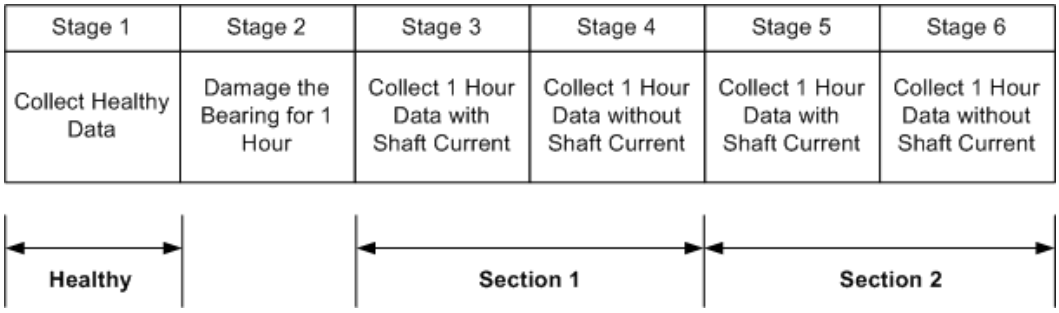

Fig. 17. Experimental Procedures for the Shaft Current Effect Comparison.

Two kinds of experiments are conducted. One driven by VSI, the other driven by the power supply mains. AMD indicators with and without the shaft current for experiment driven by VSI are shown in section 1 and section 2 of Figure 18. In each section, the indicator with the shaft current is rising because the bearing is damaged. The indicator without the shaft current is also rising. It is obvious that differences between these two indicators are small. The corresponding vibration RMS indicators are shown in Figure 19.

Indicators for motors energized by power supply mains are shown in Figure 20 and the vibration RMS indicators are shown in Figure 21. Data with and without the shaft current are collected following the same procedures as in the experiment above. It is also obvious from this experiment that these indicators are quite close.

Observations from these experiments can be summarized as follows,

1. The shaft current has some effect on the fault indicators, but this effect is not significant. It does not appear to distort the fault detection results.

2. Because of experimental procedures followed, the bearing damage process is heavily slowed down. In one experiment, the bearing is damaged just a little

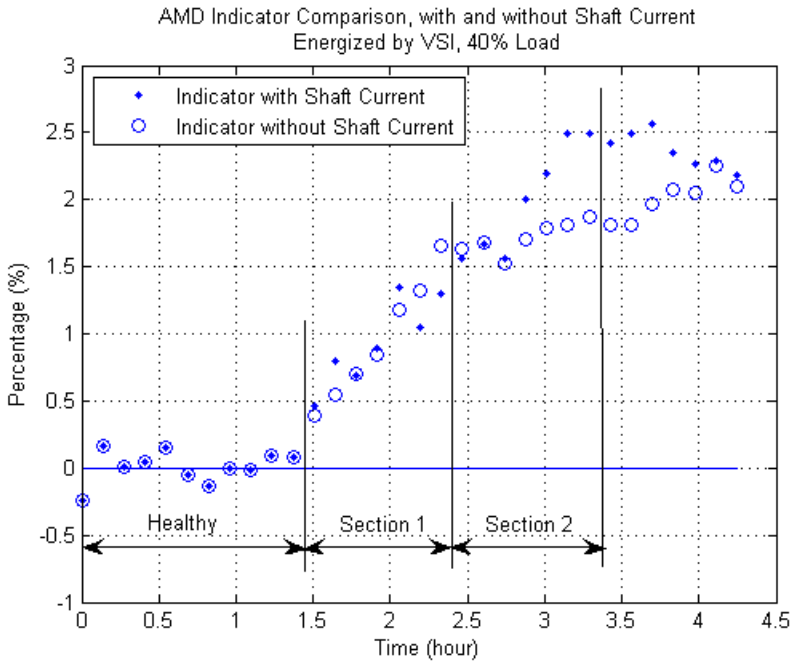

Fig. 18. AMD Indicators Comparison; Motor Energized by VSI.

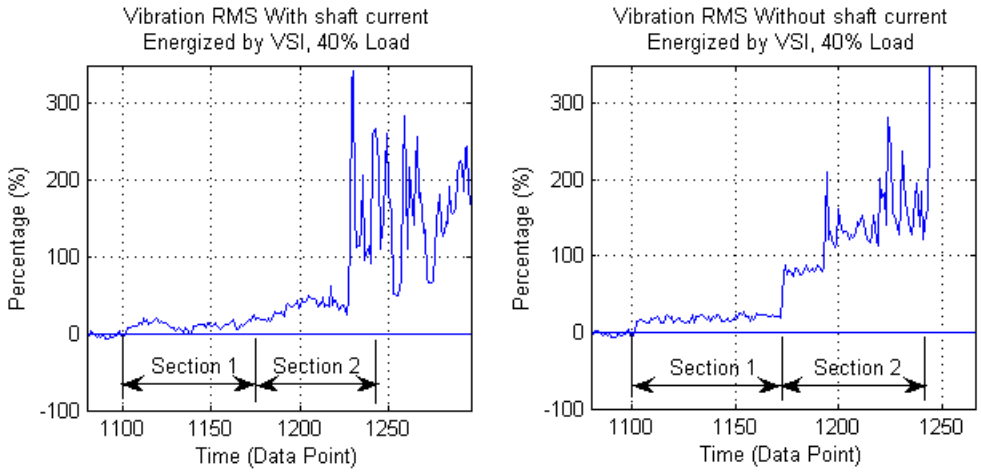

Fig. 19. Vibration RMS Comparison; Motor Energized by VSI.

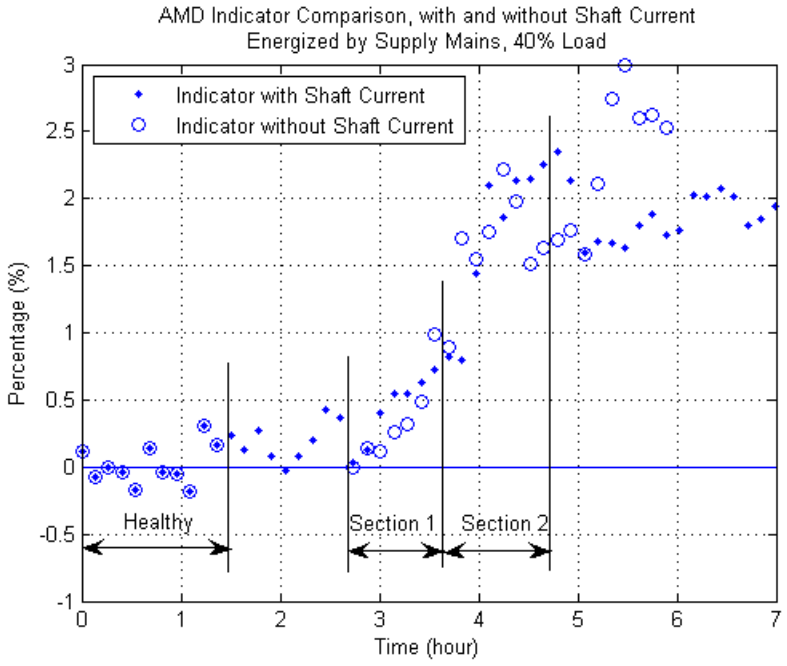

Fig. 20. AMD Indicators Comparison; Motor Energized by Power Supply Mains.

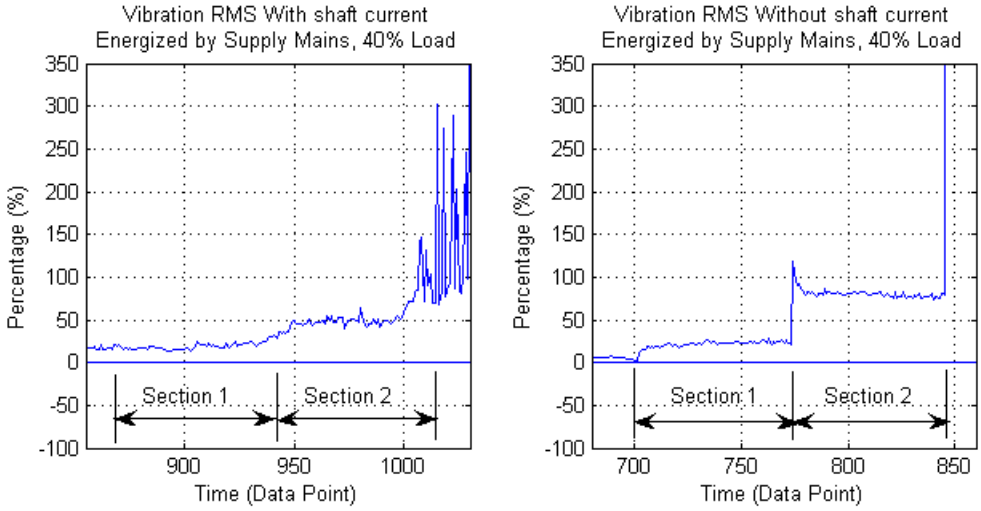

Fig. 21. Vibration RMS Comparison; Motor Energized by Power Supply Mains.

bit 16 hours after injecting the shaft current. The reason is that when the shaft current is injected, the bearing is getting damaged. But once the shaft current is removed, the damage process usually stops, and sometimes, the bearing roughness caused by the shaft current can be smoothed out, which heavily slows down the bearing damage process.

To entirely avoid the shaft current effect, the experiment procedure described above has to be used, i.e., to collect data, with and without the shaft current alternately. But, this procedure will lead to unwanted variation on the damage process and may cause the experiment to fail. Most importantly, the shaft current does not distort the fault detection result significantly. Therefore, most experiments conducted in this research are with the shaft current. But in performing closed-loop experiments data without the shaft current present are collected.

B. Effect of Different Load Levels on Indicator Performance

The proposed method is load dependent. To demonstrate this point, three experiments are conducted. Healthy bearings are used and motors are energized by the power supply mains in these experiments. Load levels used are roughly 36%, 38% and 40%. Figure 22 shows the AMD indicators for these three experiments. Deviations can be clearly seen among these AMD indicators. Although load level changes are small, 2%, deviations between AMD indicators are 3% to 4%. Stator current RMS values and voltage RMS values are shown in Figures 23 and 24 for these three experiments. When the load level changes, the magnitude of the stator current fundamental frequency changes accordingly, while the magnitude of the voltage fundamental frequency remains practically the same. This is the main reason for the deviations of the AMD indicators.

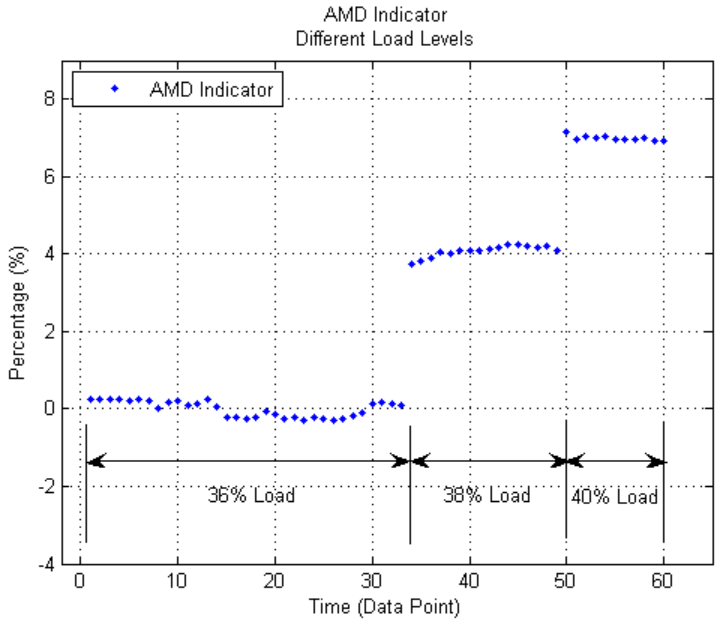

Fig. 22. AMD Indicator for Different Load Levels; Motor Energized by Power Supply Mains.

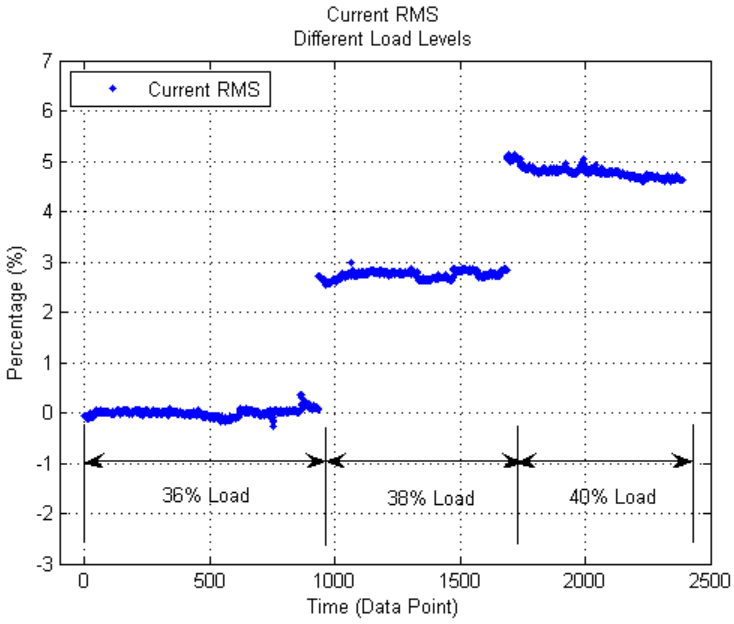

Fig. 23. Current RMS for Different Load Levels; Motor Energized by Power Supply Mains.

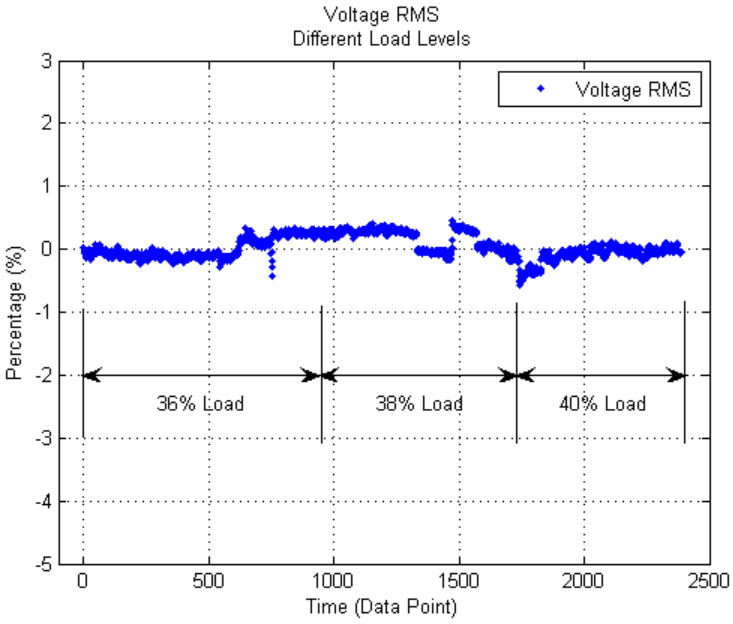

Fig. 24. Voltage RMS for Different Load Levels; Motor Energized by Power Supply Mains.

All experiment results shown in the following sections are related to specified machine operating load levels.

C. Effect of Power Supply on Indicator Performance

As the input, voltages play a very important role in motor fault detection. Without considering the voltage inputs, the current AMD variations are large even for the healthy data; and the Bearing faults cannot be detected.

Figure 25 and figure 26 show the electrical indicator and current AMD plot for a healthy experiment where the motor is energized by power supply mains. The load is 20% and the bearing is healthy. It is clear that the variation of the electrical indicator is rather small, 0.5%-0.6%, while the variation of the current AMD is very large, about 15%.

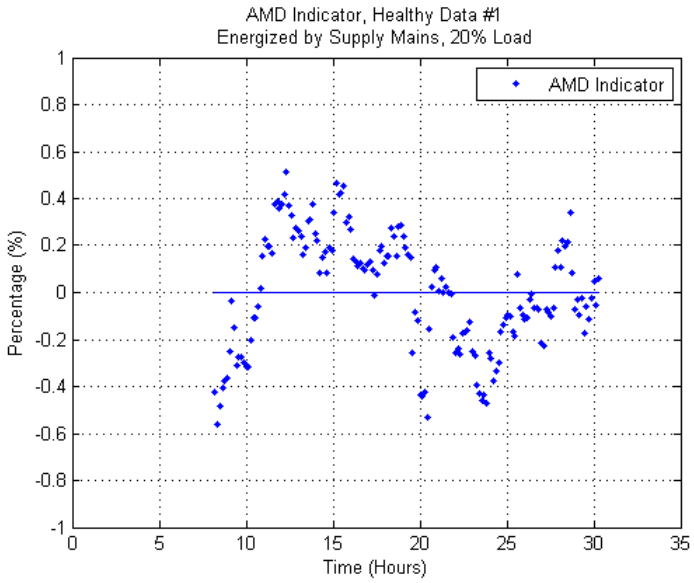

Fig. 25. Electrical AMD Indicator for Healthy Data Set #1; Motor Energized by Power Supply Mains.

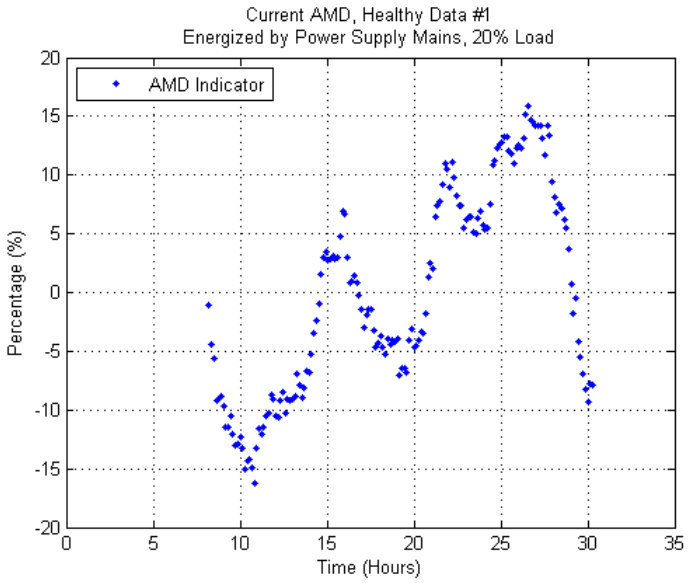

Fig. 26. Current AMD for Healthy Data Set #1; Motor Energized by Power Supply Mains.

Figure 27 shows a vibration indicator curve for an experiment where the motor is energized by the power supply mains. The load level is 0%. The bearing fault can be detected at around 6.5 hours after the experiment started using the mechanical vibration indicator. Figure 28 shows the corresponding current AMD curve. It is obvious that the current AMD alone does not have any pattern, and it cannot be used to detect the bearing fault. Figure 29 shows the cross-AMD of voltage and current. This apparent random variation of these indicators prevent their use in fault detection.

In another experiment, the motor is energized by VSI. The bearing fault can be detected at around 23.5 hours after the experiment started using the mechanical vibration indicator, as shown in Figure 30. Figure 31 and Figure 32 show the corresponding current AMD and voltage AMD, respectively. The percentage changes of the current AMD and voltage AMD are very small both in the healthy section and

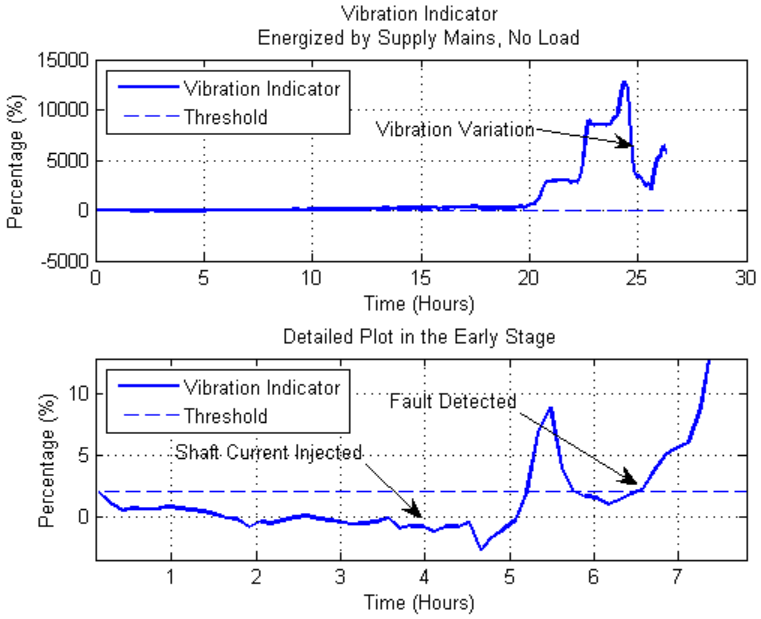

Fig. 27. Vibration Indicator for Motors Energized by Supply Mains; No Load.

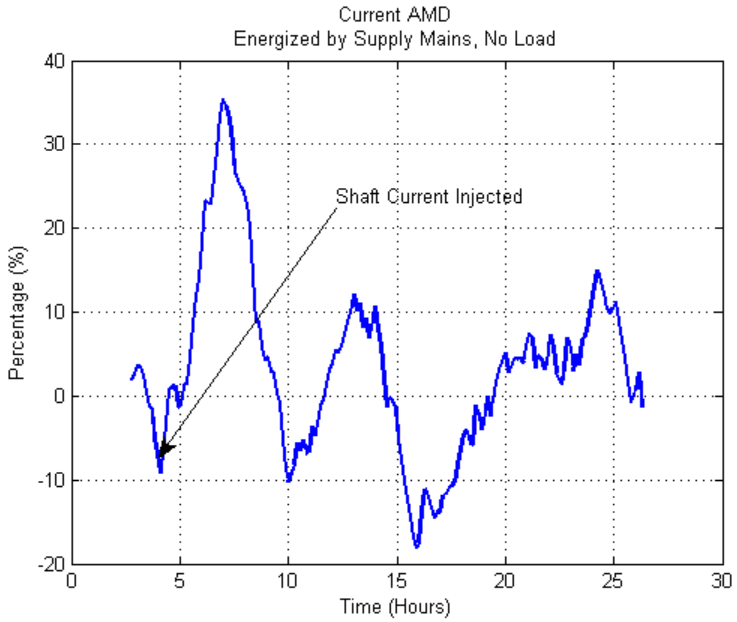

Fig. 28. Current AMD for Motors Energized by Supply Mains; No Load.

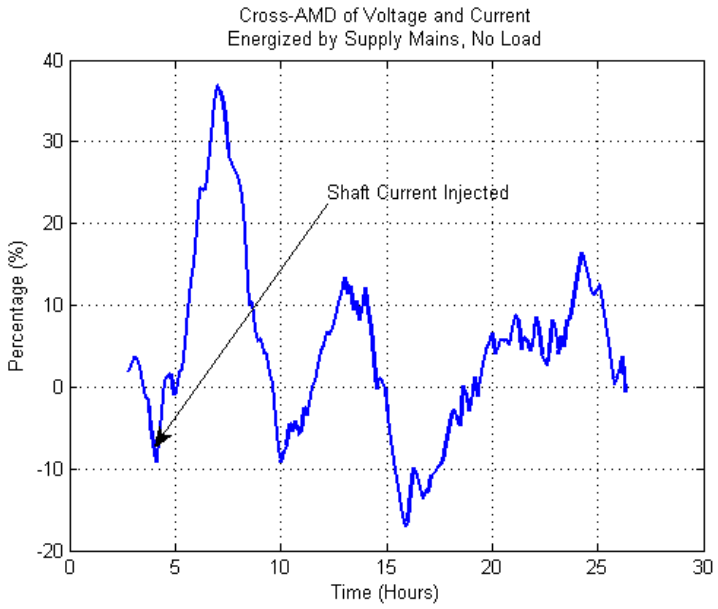

Fig. 29. Cross-AMD of Voltage & Current for Motors Energized by Supply Mains; No Load.

in the faulty section. It is reasonable to conclude that the unpredictable manners of the AMD curves come from the random variation of the inter-harmonics. Thus, the current AMD or voltage AMD alone cannot be used for fault detection purposes.

D. Healthy Baseline and Bearing Fault Detection Threshold

Healthy bearing experiments are conducted to decide the bearing fault detection threshold. Bearings used in these experiments are healthy with full amounts of grease.

Three healthy experiments are conducted when the motors are energized by power supply mains. Each of these experiments lasted 30 hours, 29 hours, and 24 hours, respectively. The same 20% load level is used. The healthy AMD indicators are shown in Figure 33. In this figure, the y axis is the absolute value of the AMD indicators. The percentage changes with respect to means are shown separately in

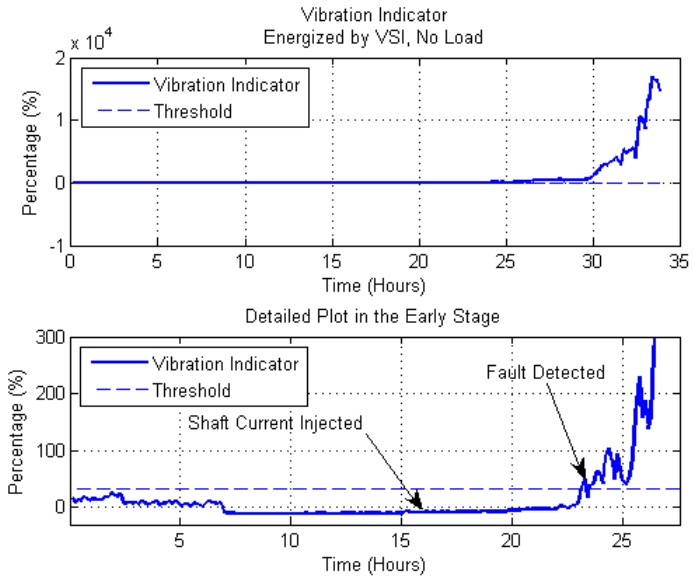

Fig. 30. Vibration Indicator for Motors Energized by VSI; No Load.

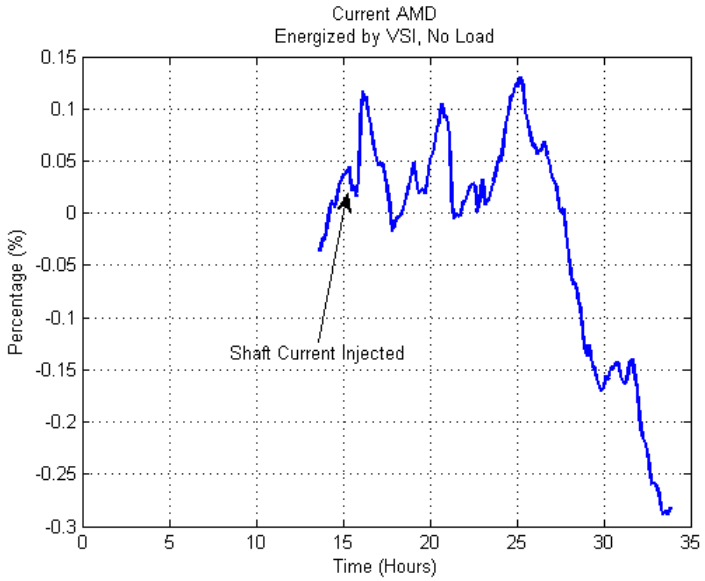

Fig. 31. Current AMD for Motors Energized by VSI; No Load.

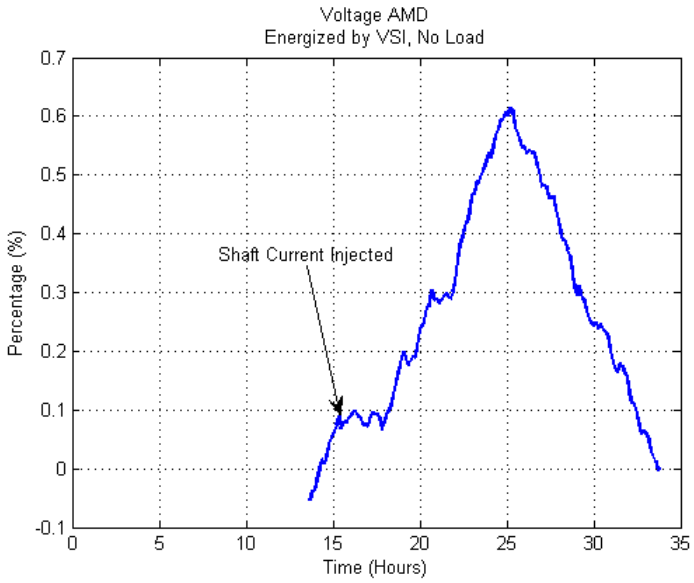

Fig. 32. Voltage AMD for Motors Energized by VSI; No Load.

Figures 25, 34, and 35. It is shown that the deviations from the maximum values to means are 0.51%, 0.41%, and 0.2% for these three healthy data sets, respectively.

To roughly identify the statistical distribution of the healthy AMD indicators, these three data sets are combined together and the distribution fits are calculated. Figure 36 shows the normal distribution fit for these three healthy data sets. In this figure, the x axis is the percentage change with respect to the mean of all data. It is shown that the normal distribution roughly fits the healthy AMD indicators.

Three healthy experiments are also conducted where the motors are energized by VSI. Each of these experiments lasted 22.2 hours, 22.5 hours, and 22.5 hours, respectively. The same load level, 20% load, is used. Healthy AMD indicators are shown in Figure 37. In this figure, the y axis is the absolute value of AMD indicators. The percentage changes with respect to means are shown separately in Figures 38, 39, and 40. It is shown that the deviations from the maximum values to means are 0.66%,

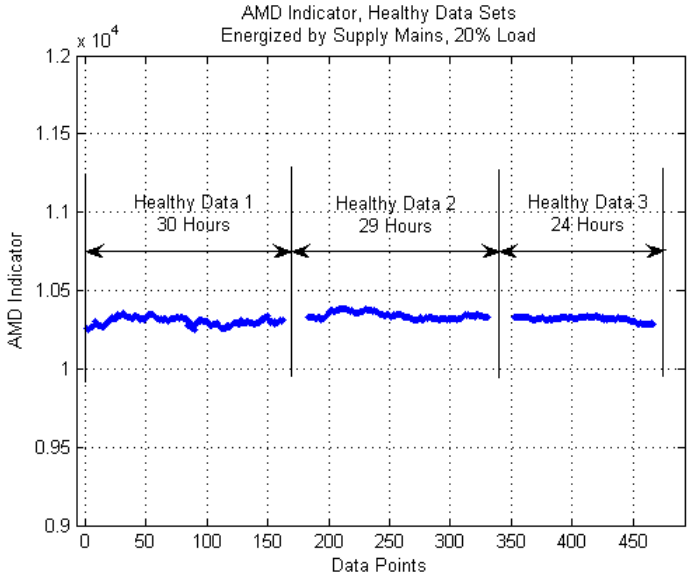

Fig. 33. AMD Indicator for Healthy Data Set #1, #2, and #3; Motor Energized by Power Supply Mains.

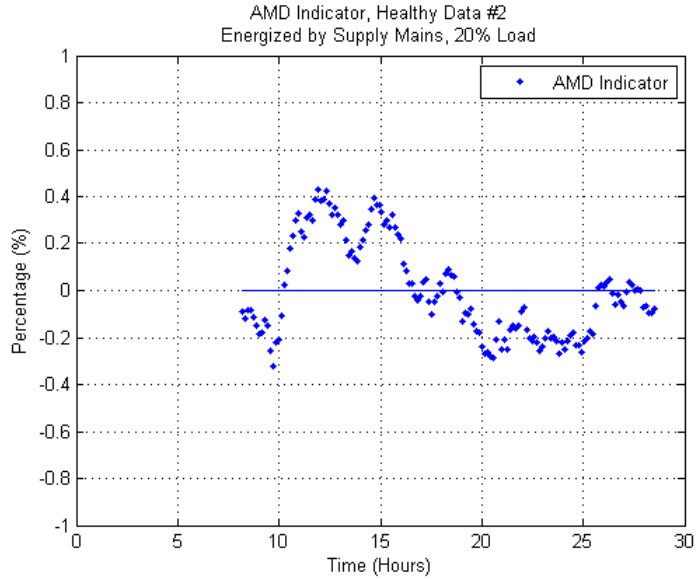

Fig. 34. AMD Indicator for Healthy Data Set #2; Motor Energized by Power Supply Mains.

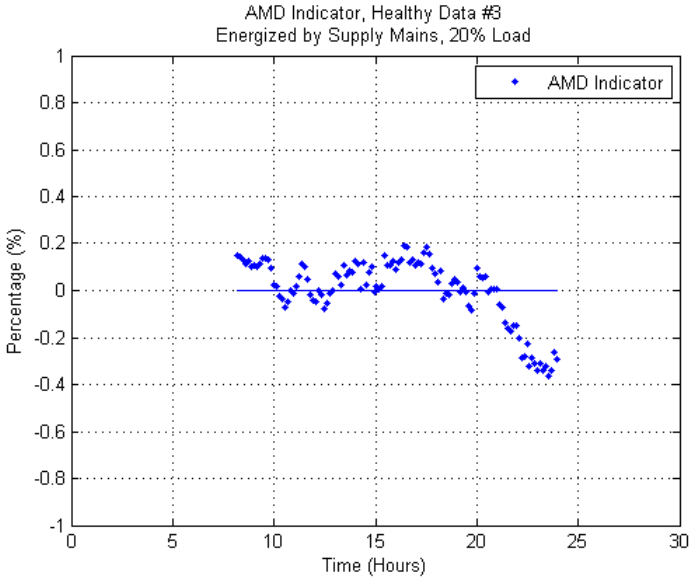

Fig. 35. AMD Indicator for Healthy Data Set #3; Motor Energized by Power Supply Mains.

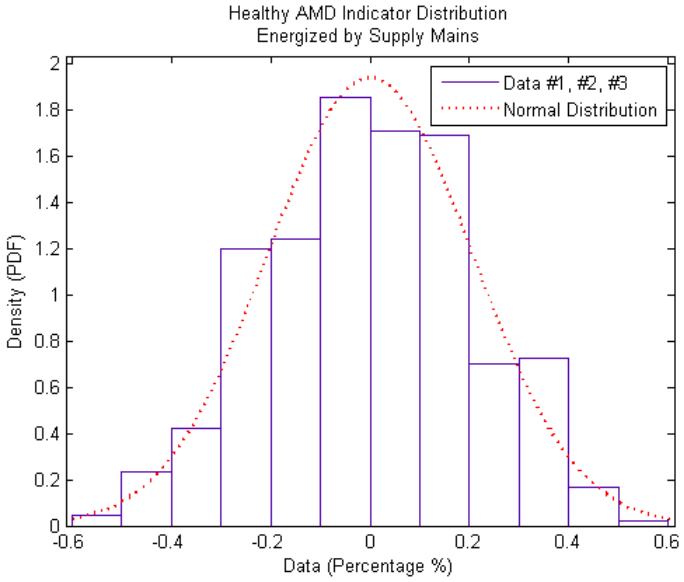

Fig. 36. Normal Distribution Fit for the Healthy AMD Indicators; Motor Energized by Power Supply Mains.

1.6% and 0.61% for these three healthy data sets. The variation in healthy data #2 is rather large compared to the others. During the bearing damage experiment, the generator is mounted on a steel plate where the motor is also mounted. When the shaft current is injected on the motor shaft, the generator cage is also energized. For some reasons, the generator load-side bearing is slightly damaged, even though there is no obvious closed circuit through the generator rotor shaft, bearing, and cage. Actually, when collecting healthy data #2, noise originated from the generator. After replacing the generator load-side bearing, this noise disappeared. Then, healthy data #3 is collected with the new installed generator load-side bearing. The AMD indicator for healthy data #3 has small variation, as shown in Figure 40.

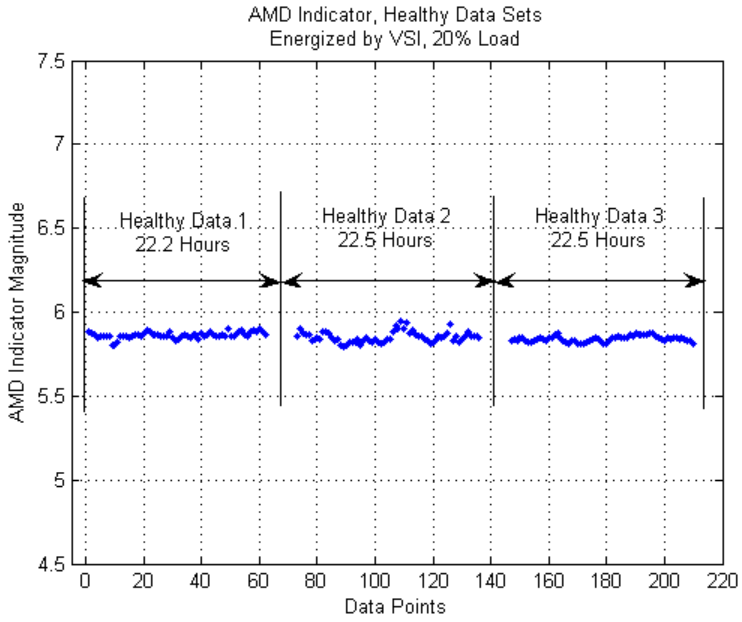

Fig. 37. AMD Indicator for Healthy Data #1, #2, and #3; Motor Energized by a VSI.

These three healthy data sets are combined together and the distribution fittings are calculated. Figure 41 shows the normal distribution fit for these three healthy

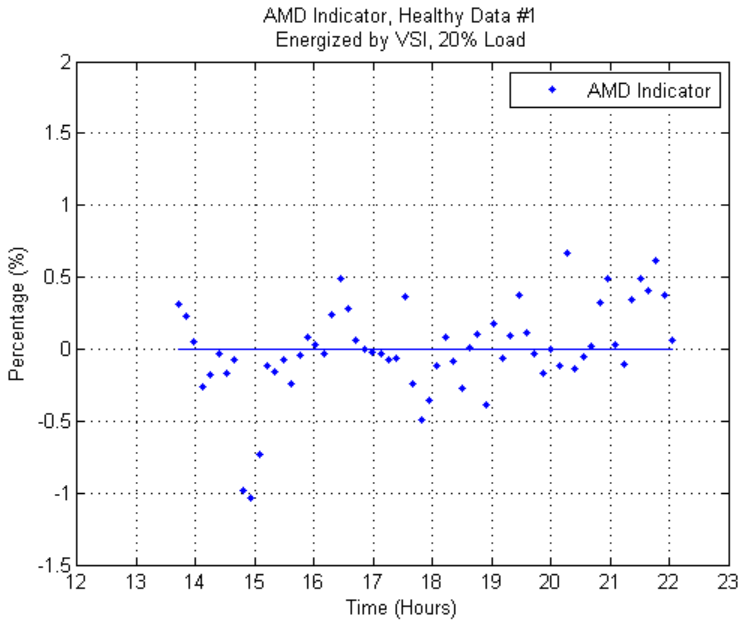

Fig. 38. AMD Indicator for Healthy Data Set #1; Motor Energized by a VSI.

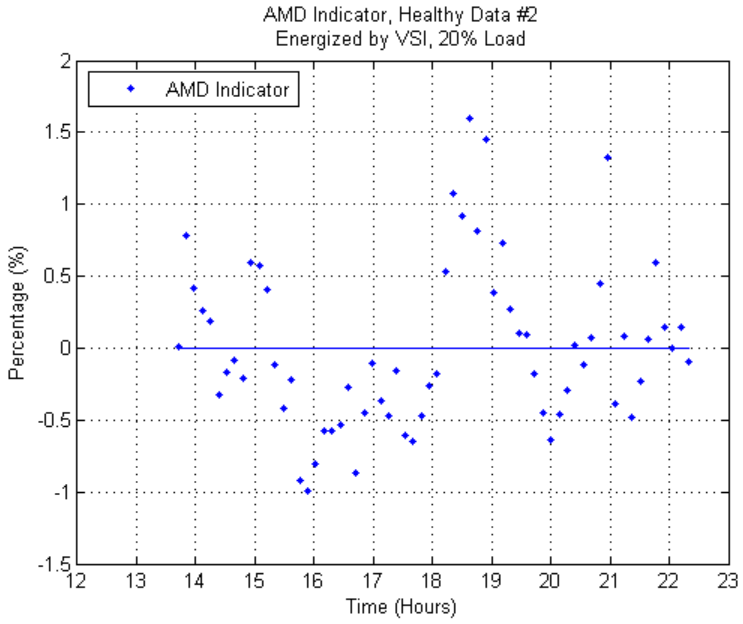

Fig. 39. AMD Indicator for Healthy Data Set #2; Motor Energized by a VSI.

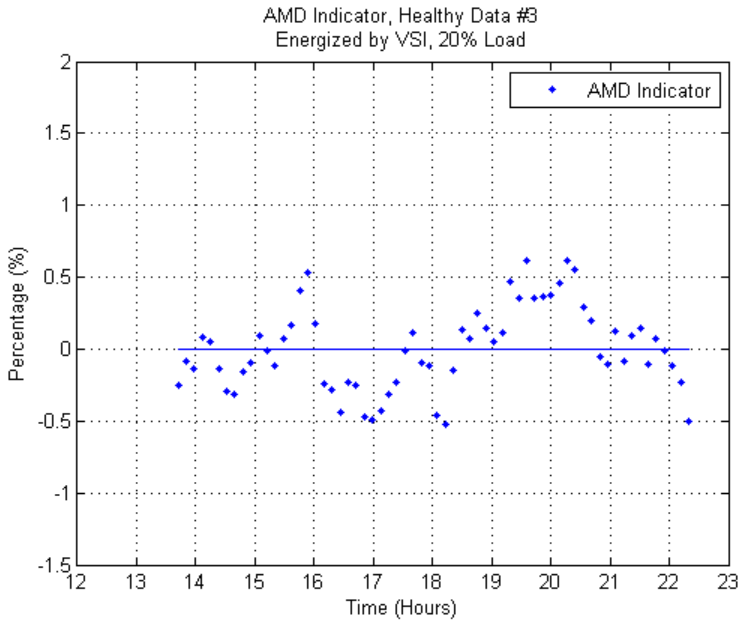

Fig. 40. AMD Indicator for Healthy Data Set #3; Motor Energized by a VSI.

data sets. In this figure, the x axis is the percentage change with respect to the mean of all data. It is shown that the normal distribution roughly fits healthy AMD indicators. There are several outliers in Figure 41, which result from healthy data #2.

The percentage variations of healthy AMD indicators are very small and percentage deviations from healthy to faulty indicators are also not big because large amounts of data are averaged in the proposed method. It is not easy to set a fixed threshold for the fault detection purpose in a practical environment, because the healthy baseline may vary in different motors and different loads. Most importantly, bearing damage experiments are conducted continually in this research and the proposed method should be used in the similar continuous monitoring manner in practice. Therefore, it is reasonable to use adaptive thresholds for different continuous monitoring ex-

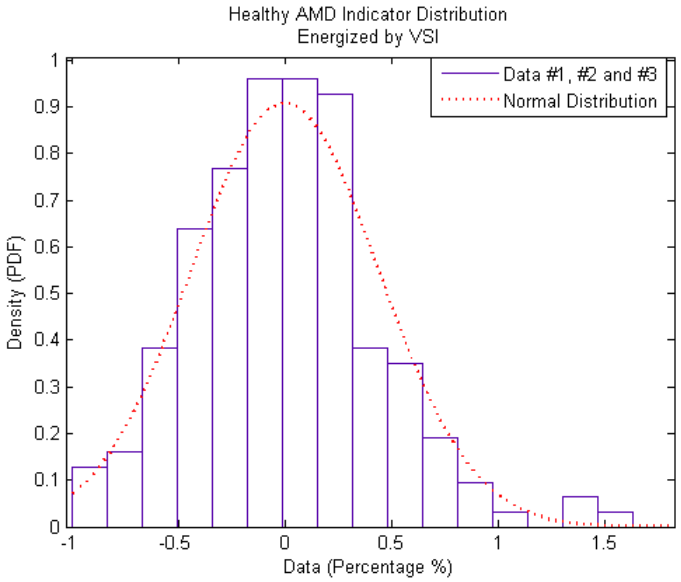

Fig. 41. Normal Distribution Fit for the Healthy AMD Indicators; Motor Energized by a VSI

periments. These adaptive thresholds are decided according to healthy data in each experiment.

Because the healthy AMD indicators are roughly normally distributed, three times the standard deviation of the healthy data in each experiment is used as the bearing fault detection threshold in AMD indicators. This way, the false alarms are limited to less than 1% since three times standard deviation accounts for 99% of the samples in the normal distribution. The mechanical vibration indicators are used as a reference for the electrical AMD indicators. In order to compare these two types of indicators, the same three times standard deviation thresholds are also used in the vibration indicators for fault detection purposes.

E. Experimental Results for Motors Energized by Power Supply Mains

The generator test bed is used in experiments energized by power supply mains. Different level of loads are used, including 0% load, 20% load, and 40% load. Because of the limitation on the generator field excitation current, load levels higher than 40% are not used.

1. Experiments with Motor at No Load Conditions

The first experimental results for no load condition are shown in Figures 42 and 43. The shaft current is injected at 4 hours after the experiment started. Using the three times of standard deviation threshold discussed above, the bearing fault can be detected at around 6.5 hours using the mechanical vibration indicator, which is shown in Figure 42, and around 4.6 hours using the electrical AMD indicator, which is shown in Figure 43.

In the vibration indicator, large variations show up after the experiment ran for about 24 hours, which is shown in Figure 42. The reason is that when the bearing is damaged very heavily, the vibration rises to a very high level, which exceeds the limitation of the vibration sensor so that the sensed vibration signals display an unreasonable manner. In follow-on experiments, bearings are not damaged too much so that the vibration levels are kept to a rather low level to avoid damaging the experimental setup.

The second experimental results for the no load condition are shown in Figures 44 and 45. The shaft current is injected at 3.9 hours after the experiment started. Using the three times of standard deviation threshold discussed above, the bearing fault can be detected using the vibration indicator at around 5.5 hours, as shown in Figure 44. The electrical AMD indicator detects the fault at around 5.5 hours too,

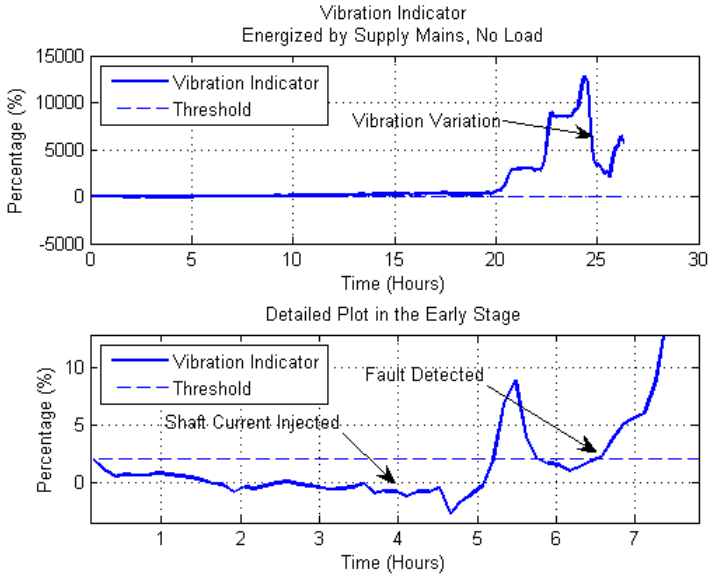

Fig. 42. Vibration Indicator of Data Set #1 for Motors Energized by Power Supply Mains; No Load.

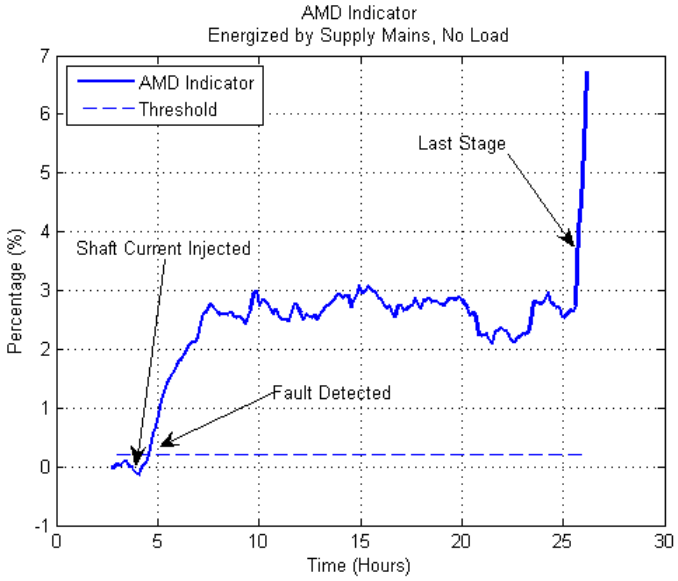

Fig. 43. AMD Indicator of Data Set #1 for Motors Energized by Power Supply Mains; No Load.

which is shown in figure 45.

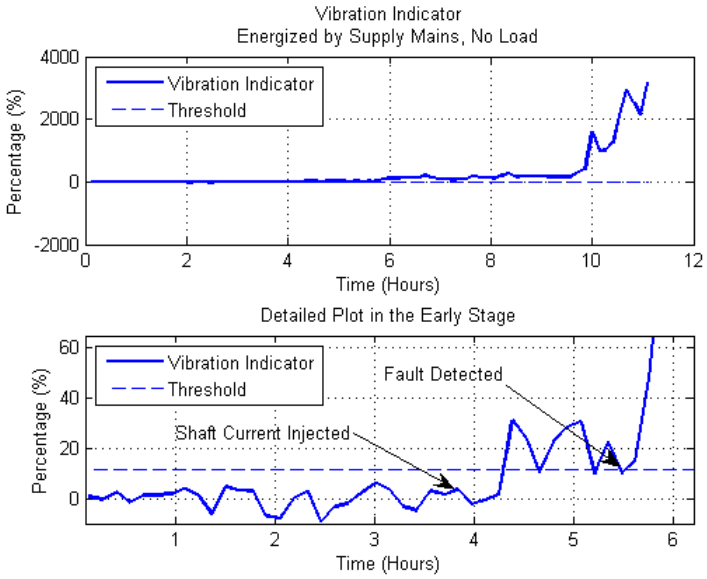

Fig. 44. Vibration Indicator of Data Set #2 for Motors Energized by Power Supply Mains; No Load.

2. Experiments with Motor at 20% Load Conditions

In the generator test bed, a synchronous generator is used to load the induction motor. This generator is modified from a CS-130 alternator by removing the voltage rectifier and voltage regulator. An external power supply is used to energize the generator magnetic field. Because of the output current limitation of the power supply, the generator field current cannot exceed 2 A. Hence, the maximum load that this generator can provide to the induction motor is 40%.

The first experimental results with 20% load level are shown in Figures 46 and 47. In this experiment, the shaft current is injected at around 8.7 hours after the experiment started. The bearing fault can be detected at 9.2 hours using the me-

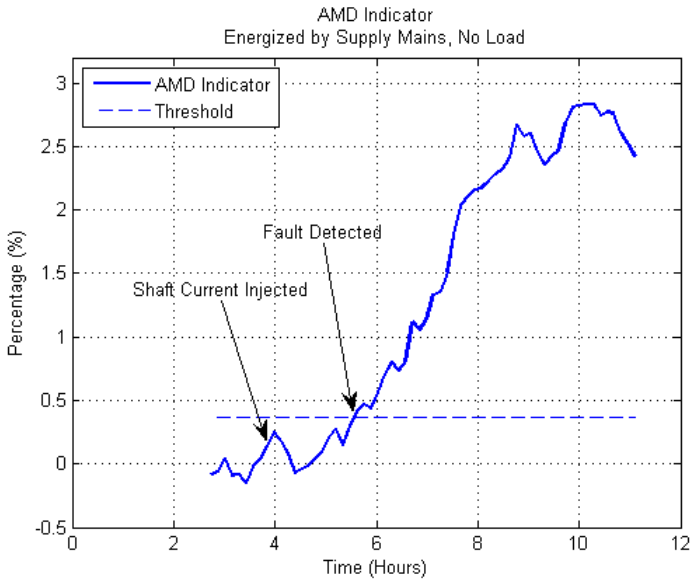

Fig. 45. AMD Indicator of Data Set #2 for Motors Energized by Power Supply Mains; No Load.

chanical vibration indicator, as shown in Figure 46, and 9.3 hours using the electrical AMD indicator, as shown in Figure 47.

The second set of experimental results are shown in Figures 48 and 49. In this experiment, the shaft current is injected at around 10.8 hours after the experiment started. The bearing fault can be detected at 11.8 hours using the mechanical vibration indicator, as shown in Figure 48, and 12.5 hours using the electrical AMD indicator, as shown in Figure 49.

3. Experiments with Motor at 40% Load Conditions

The first set of experimental results with 40% load are shown in Figures 50 and 51. In this experiment, the shaft current was injected at around 9.2 hours after the experiment started. The bearing fault can be detected at 9.7 hours using the mechanical vibration indicator, as shown in Figure 50, and 10.1 hours using the

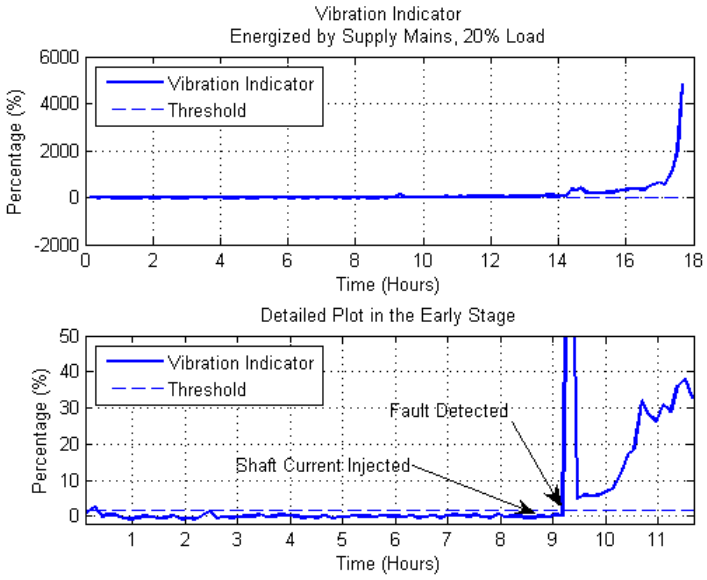

Fig. 46. Vibration Indicator of Data Set #1 for Motors Energized by Power Supply Mains; 20% Load.

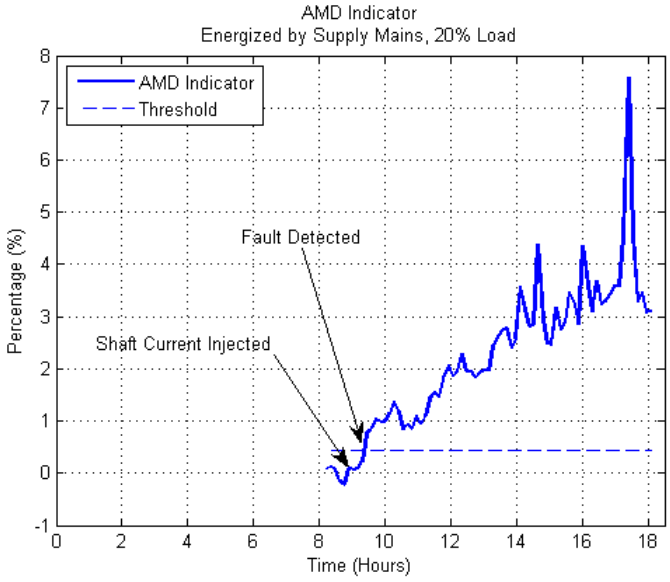

Fig. 47. AMD Indicator for of Data Set #1 for Motors Energized by Power Supply Mains; 20% Load.

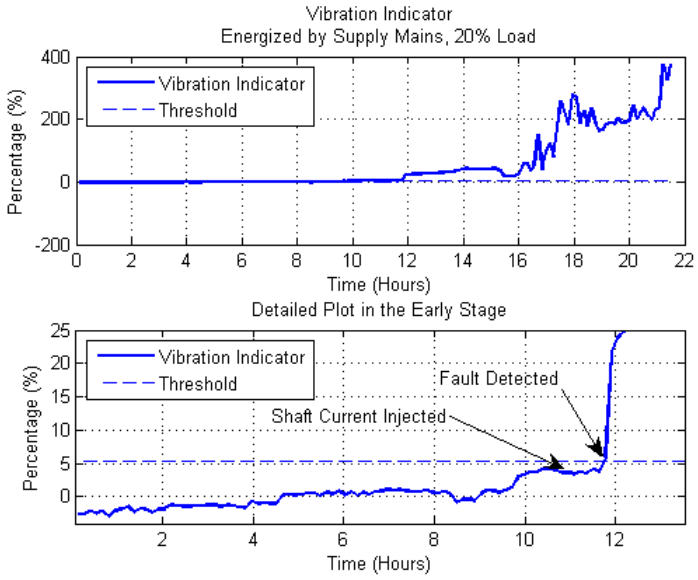

Fig. 48. Vibration Indicator of Data Set #2 for Motors Energized by Power Supply Mains; 20% Load.

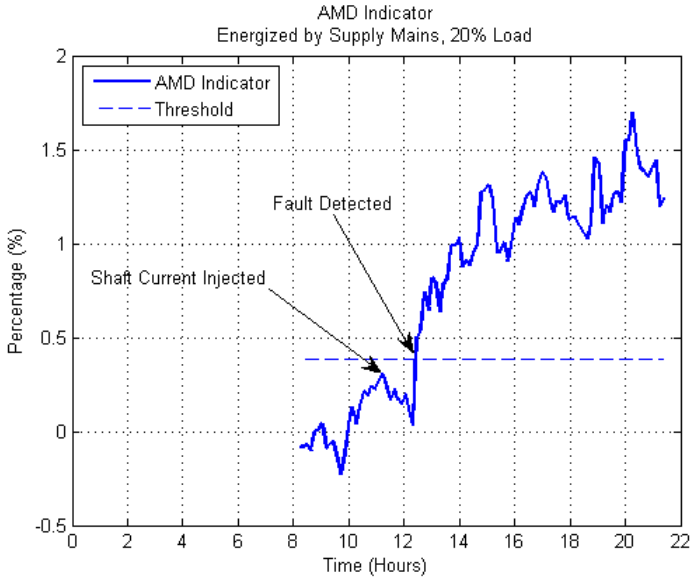

Fig. 49. AMD Indicator for of Data Set #2 for Motors Energized by Power Supply Mains; 20% Load.

electrical AMD indicator, as shown in Figure 51.

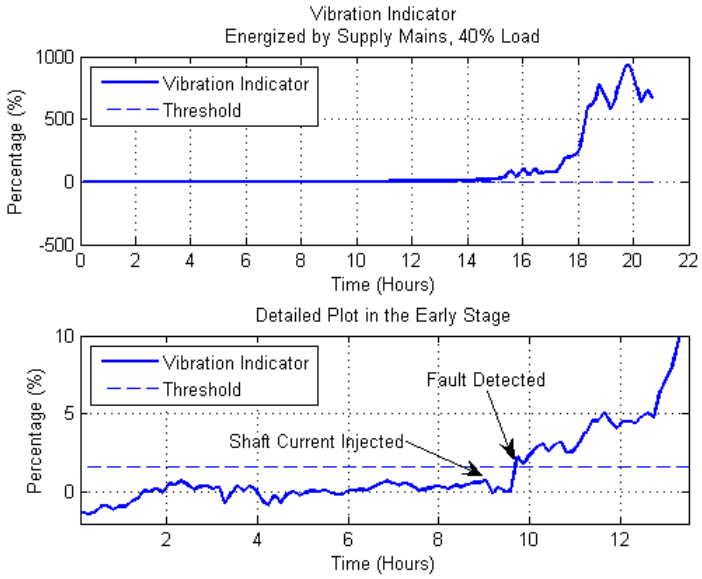

Fig. 50. Vibration Indicator of Data Set #1 for Motors Energized by Power Supply Mains; 40% Load.

The second set of experiment results are shown in Figures 52 and 53. In this experiment, the shaft current is injected at around 8.8 hours after the experiment started. The bearing fault can be detected at 9.6 hours using the mechanical vibration indicator, as shown in Figure 52, and 9.8 hours using the electrical AMD indicator, as shown in Figure 53.

4. Summary of Experiments for Motors Energized by Power Supply Mains

All experiments where the motors are energized by the power supply mains are summarized in Table III. Differences between electrical AMD indicator detection times and mechanical vibration indicator detection times are calculated in this table. The means of these time differences are -0.95 hours, +0.4 hours, and +0.63 hours, re-

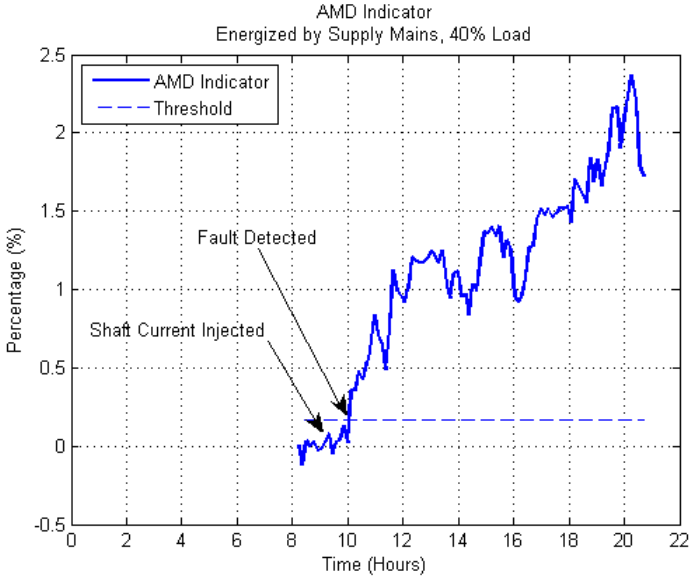

Fig. 51. AMD Indicator of Data Set #1 for Motors Energized by Power Supply Mains; 40% Load.

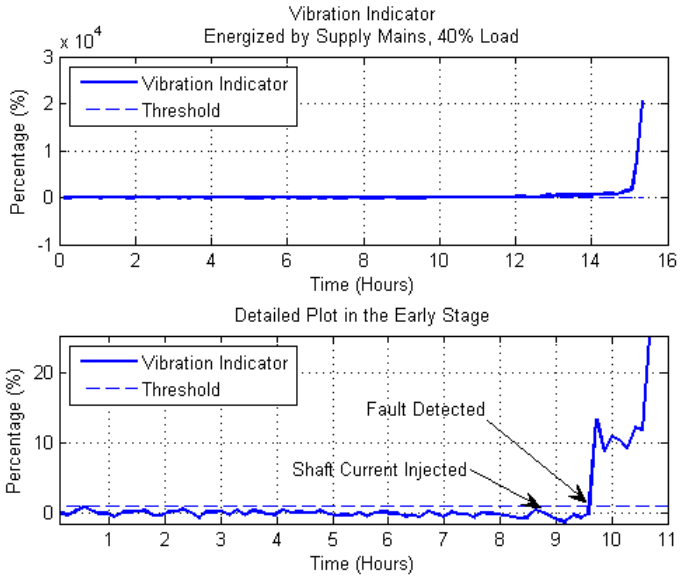

Fig. 52. Vibration Indicator of Data Set #2 for Motors Energized by Power Supply Mains; 40% Load.

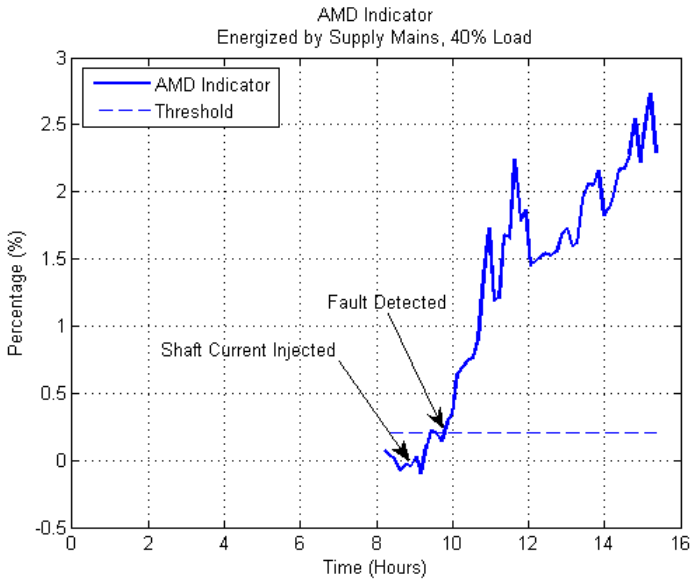

Fig. 53. AMD Indicator of Data Set #2 for Motors Energized by Power Supply Mains; 40% Load.

spectively for 0%, 20% and 40% load levels. Here, the negative sign indicates that the AMD indicator detects bearing faults earlier than the vibration indicator, while the positive sign means that the AMD indicator detects bearing faults later than the vibration indicator.

Bearing damage experiments conducted in this research used shaft currents to accelerate the bearing damage process. Usually, the total experiment time from the shaft current injection time to the bearing being heavily damaged is around 22 hours (as shown in Figure 43). In practical industral environment, bearing life spans are usually 6 to 9 months. Assume the life of the bearing is 7 months, a one-hour experiment time then roughly equals 9.5 days. Therefore, means of fault detection time differences between electrical AMD indicators and mechanical vibration indicators can be roughly estimated as -9 days (earlier detection), +3.8 days (later detection) and +6 days (later detection), for 0%, 20% and 40% load levels, respectively.

Table III. Summary of Experiments for Motors Energized by Power Supply Mains.

Load	Data Sets	Vibration Indicator (Hours)	AMD Indicator (Hours)	Difference* (Hours)
No Load	I	6.5	4.6	-1.9
	II	5.5	5.5	0
	III	N/A	13.1	N/A
Mean		-	-	-0.95
20% Load	I	9.2	9.3	+0.1
	II	11.8	12.5	+0.7
Mean		-	-	+0.4
40% Load	I	9.7	10.1	+0.4
	II	9.6	9.8	+0.2
	III	11.3	12.6	+1.3
Mean		-	-	+0.63

* The difference of the fault detection time between the vibration and AMD Indicators.

F. Experimental Results for Motors Energized by a VSI

When motors are energized by a VSI, the rich current inter-harmonics are the biggest problem for fault detection. To detect bearing faults, the VSI AMD indicator is used.

The actual VSI supply fundamental is not purely sinusoidal, but the combination of square waves. In the VSI AMD indicator calculation, the special frequencies, which are modulated with a frequency band around the supply fundamental, are calculated. By doing this, the variation of the VSI AMD indicator is bigger than that of the power supply main AMD indicator because the frequency band around the supply fundamental contains more non-stationary inter-harmonics.

In this research, experiments are conducted with V/Hz open-loop and V/Hz closed-loop VSI operation. These results are summarized in the following sections.

1. Speed Set-point Regulation Using a VSI Operating in Open-loop V/Hz Control Mode

a. Experiments with Motor at No Load Conditions

The first set of experimental results for the no load condition are shown in Figures 54 and 55. The shaft current is injected at 15.5 hours after the experiment started. The bearing fault can be detected at around 23.5 hours using the mechanical vibration indicator, as shown in Figure 54, and around 16.3 hours using the electrical AMD indicator, as shown in Figure 55. There are abnormal variations in the vibration signals in this experiment. In the healthy section, the vibration signal goes down, which leads to late detection in the vibration indicator compared with the AMD indicator. One possible reason is the bearing roughness. Initially, the test bearing had some kinds of roughness on the contacting surface. After a period of time running, this roughness was smoothed out because only 4% to 5% grease was filled in the

bearing. Actually, the behavior of the non-fully filled bearings is not predictable. In some cases, the vibration levels are increased even though no shaft current is injected.

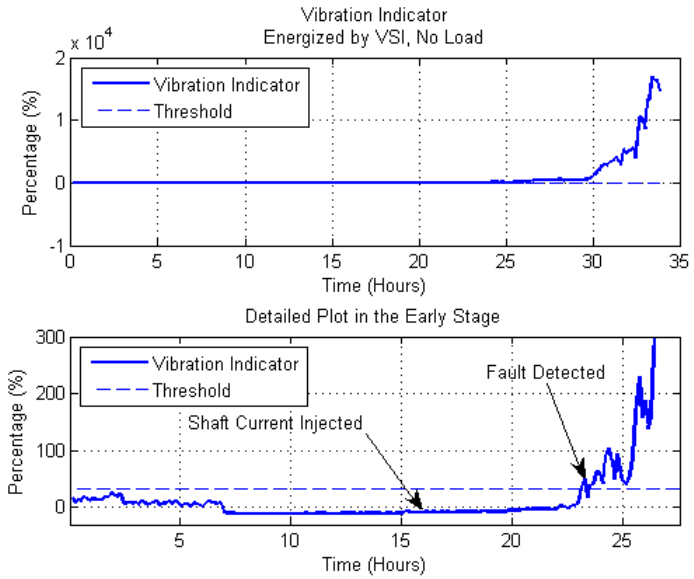

Fig. 54. Vibration Indicator of Data Set #1 for Motors Energized by a VSI; No Load.

The second set of experimental results are shown in Figures 56 and 57. In this experiment, the healthy data are not long enough. Only 11.5 hour healthy data are collected. After that, the shaft current is injected. From Figure 56, we see that the bearing fault can be picked up at 17.3 hours using the mechanical vibration indicator. From Figure 57, we see that the bearing fault is detected at around 14.9 hours using the electrical AMD indicator.

b. Experiments with Motor at 20% Load Conditions

The first set of experimental results are shown in Figures 58 and 59. In this experiment, the shaft current is injected at around 15.9 hours after the experiment started.

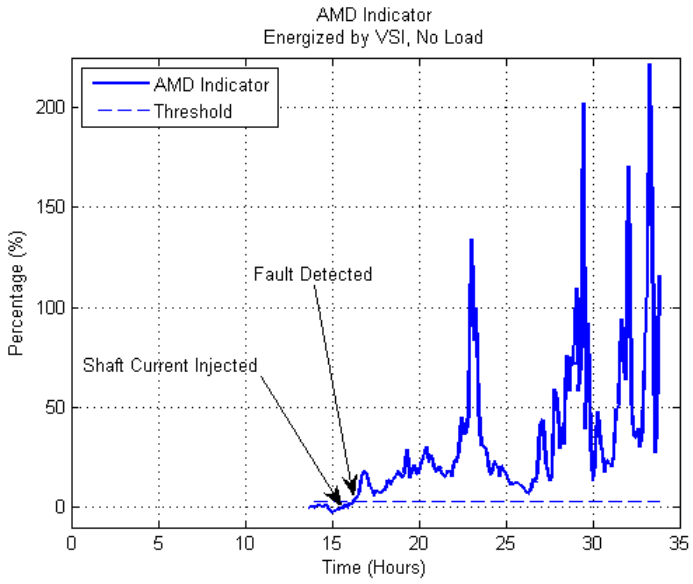

Fig. 55. AMD Indicator of Data Set #1 for Motors Energized by a VSI; No Load.

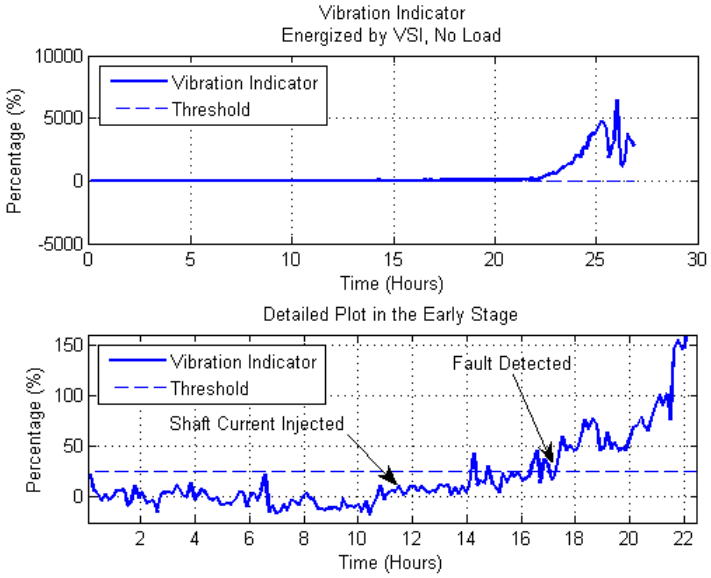

Fig. 56. Vibration Indicator of Data Set #2 for Motors Energized by a VSI; No Load.

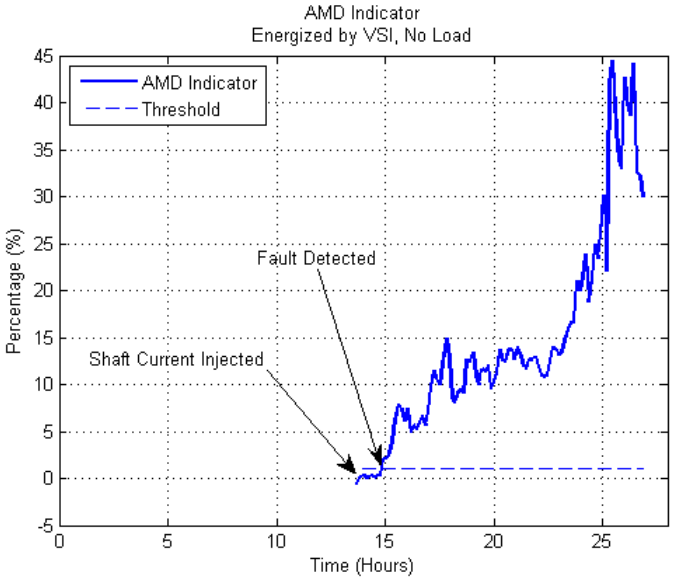

Fig. 57. AMD Indicator of Data Set #2 for Motors Energized by a VSI; No Load.

The bearing fault can be detected at 20.1 hours using the mechanical vibration indicator, as shown in Figure 58, and 18 hours using the electrical AMD indicator, as shown in Figure 59.

The second set of experimental results are shown in Figures 60 and 61. In this experiment, the shaft current is injected at around 14.1 hours after the experiment started. The bearing fault can be detected at 15.5 hours using the mechanical vibration indicator, as shown in Figure 60, and 14.8 hours using the electrical AMD indicator, as shown in Figure 61.

c. Experiments with Motor at 40% Load Conditions

The first set of experimental results are shown in Figures 62 and 63. In this experiment, the shaft current was injected at around 15 hours after the experiment started. The bearing fault can be detected at 16.1 hours using the mechanical vibration indi-

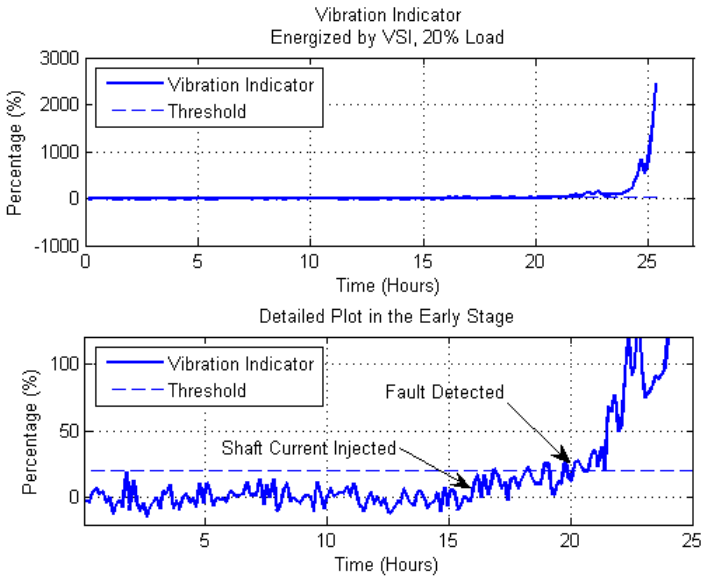

Fig. 58. Vibration Indicator of Data Set #1 for Motors Energized by a VSI; 20% Load.

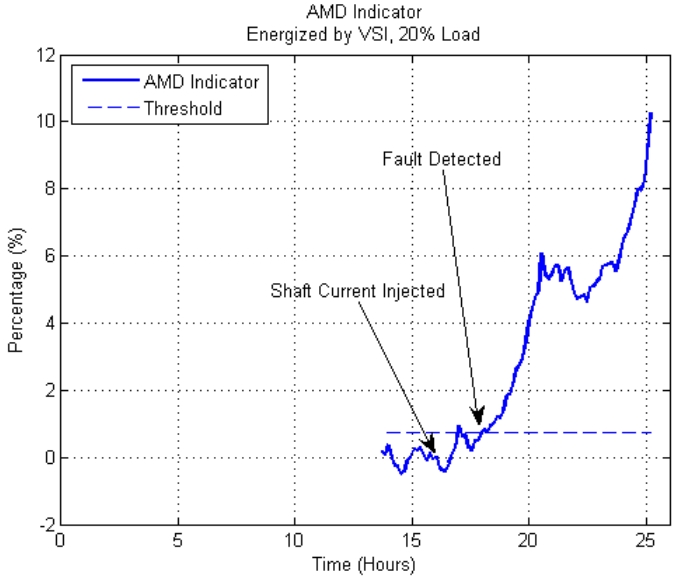

Fig. 59. AMD Indicator of Data Set #1 for Motors Energized by a VSI; 20% Load.

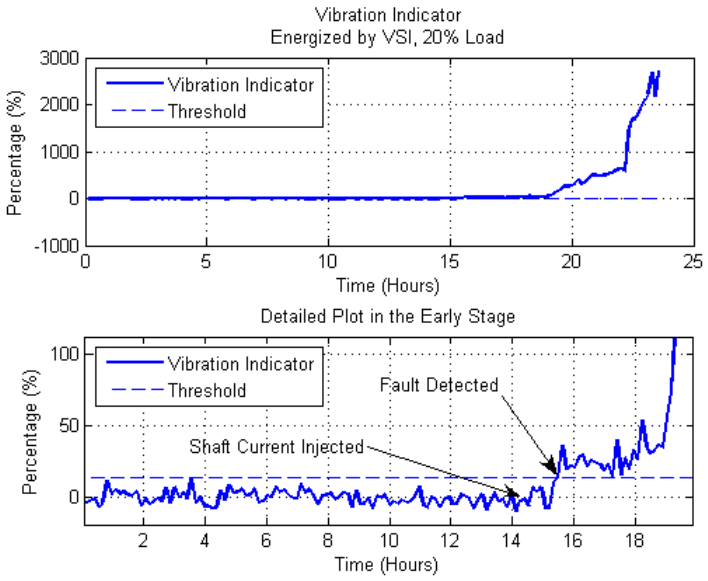

Fig. 60. Vibration Indicator of Data Set #2 for Motors Energized by a VSI; 20% Load.

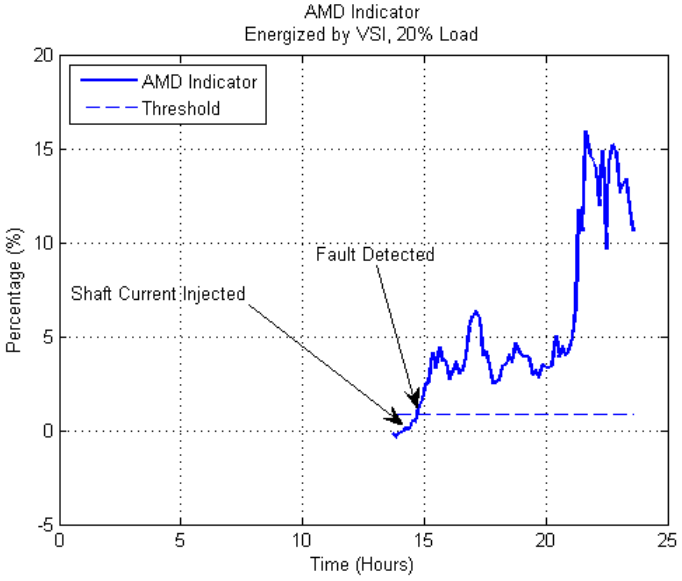

Fig. 61. AMD Indicator of Data Set #2 for Motors Energized by a VSI; 20% Load.

cator, as shown in Figure 62, and 18.9 hours using the electrical AMD indicator, as shown in Figure 63.

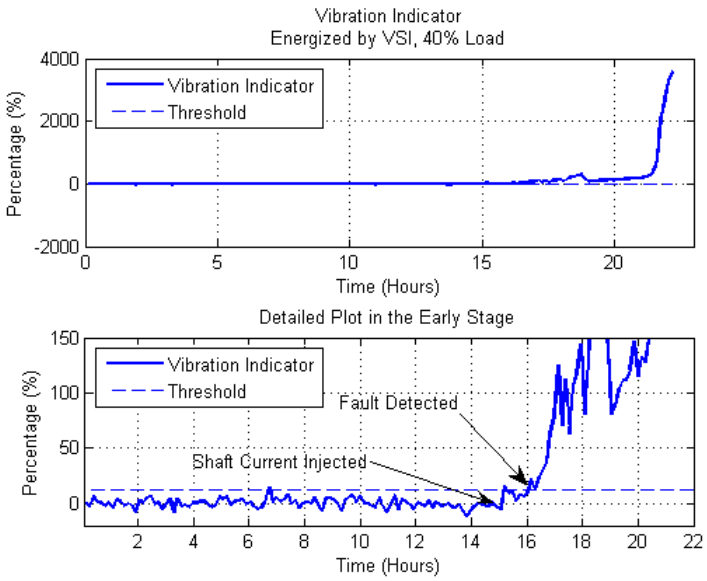

Fig. 62. Vibration Indicator of Data Set #1 for Motors Energized by a VSI; 40% Load.

The second set of experimental results are shown in Figures 64 and 65. In this experiment, the shaft current is injected at around 15 hours after the experiment started. The bearing fault can be detected at 18.9 hours using the mechanical vibration indicator, as shown in Figure 64, and 18.7 hours using the electrical AMD indicator, as shown in Figure 65.

d. Summary of Experiments for Motors Energized by a VSI Operating in Open-loop V/Hz Control Mode

All experiments using VSI in open-loop control operating mode are summarized in Table IV. Time differences between electrical AMD indicator detection times and mechanical vibration indicator detection times are calculated in this table. Means

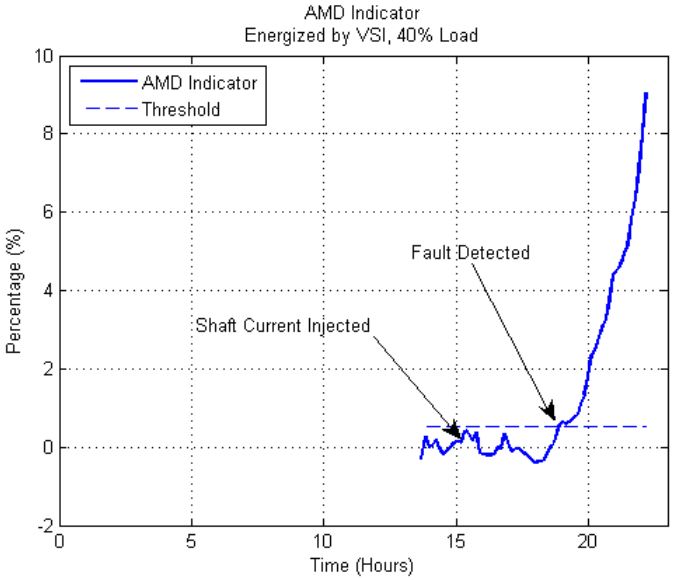

Fig. 63. AMD Indicator of Data Set #1 for Motors Energized by a VSI; 40% Load.

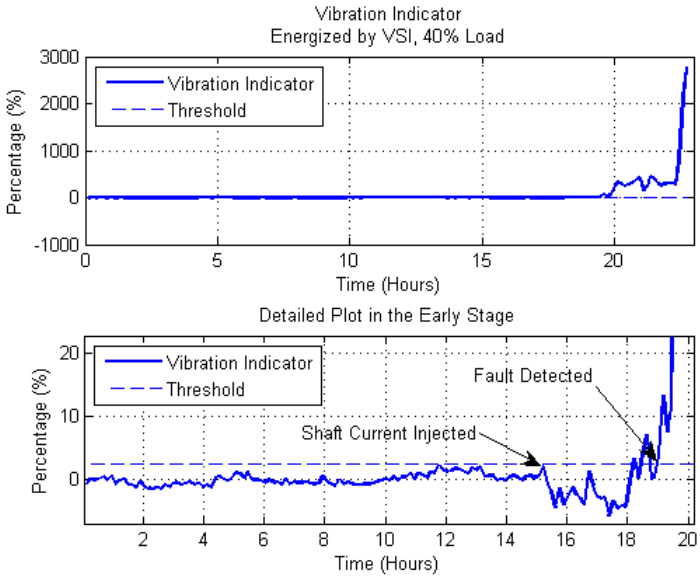

Fig. 64. Vibration Indicator of Data Set #2 for Motors Energized by a VSI; 40% Load.

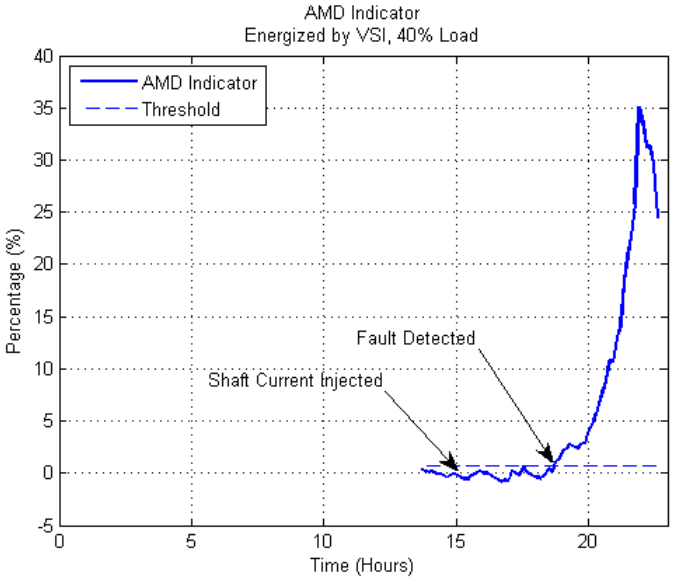

Fig. 65. AMD Indicator of Data Set #2 for Motors Energized by a VSI; 40% Load.

of differences are -3.67 hours, -1.4 hours, and +0.87 hours, respectively, for 0%, 20% and 40% load levels. Here, the negative sign means that the AMD indicator detects bearing faults earlier than the vibration indicator, while the positive sign means that the AMD indicator detects bearing faults later than the vibration indicator.

Bearing damage experiments conducted in this research use shaft currents to accelerate the bearing damage process. If we assume one hour experiment time equals 9.5 real days, as in cases of experiments energized by power supply mains, means of fault detection time differences between electrical AMD and mechanical vibration indicators can be roughly estimated as -34.8 days (earlier detection), -13.3 days (earlier detection), and +8.2 days (later detection) for 0%, 20%, and 40% load levels, respectively.

Table IV. Summary of Experiments for Motors Energized by a VSI Operating in Open-loop V/Hz Control Mode.

Load	Data Sets	Vibration Indicator (Hours)	AMD Indicator (Hours)	Difference* (Hours)
No Load	I	23.5	16.3	-7.2
	II	17.3	14.9	-2.4
	III	N/A	15	N/A
	IV	8.2	6.8	-1.4
Mean		-	-	-3.67
20% Load	I	20.1	18	-2.1
	II	15.5	14.8	-0.7
Mean		-	-	-1.4
40% Load	I	16.1	18.9	+2.8
	II	18.9	18.7	-0.2
	III	16.2	16.2	0
Mean				+0.87

* The difference of the fault pick up time between the vibration and AMD indicators.

2. Speed Set-point Regulation Using a VSI Operating in Closed-loop V/Hz Control Mode

The synchronous generator test bed, as shown in Figure 4, cannot be used in performing experiments with the VSI using speed feedback control since there is not enough space to install an encoder. So, the gearbox test bed, shown in Figure 5, is used.

a. Experimental Procedures

Usually, the total time of the bearing damage experiment is around 26 to 32 hours. Because the gearbox cannot endure such a long running time, different experimental procedures are used for the closed-loop control experiments, which is shown in Figure 66. Firstly, the healthy data is collected. Then, the gearbox and other devices on the test bed are disconnected from the motor, and the shaft current is injected to damage the motor bearing. In this procedure, data are not collected. Finally, after the bearing is damaged to some degree, the shaft current is removed, the gearbox is connected, and the faulty data are collected.

Stage 1	Stage 2	Stage 3
Collect Healthy Data	Disconnect the gearbox; Damage the bearing with shaft current; No data collection.	Remove the shaft current; Connect the gearbox; Collect faulty data.

Fig. 66. Closed-loop Control Experimental Procedures.

Usually, VSI works at different speed set points. In this research, two speed set points are used to test the proposed method, the 60Hz and the 40Hz. In the 60Hz set point, the gearbox can load the motor at 45% of full rated load. In the 40Hz set

point, the motor rotating speed drops, while the load torque keeps constant so that the actual motor load level drops to around 41%.

b. Experiments at 60Hz Set Point

Two experiments are conducted at 60Hz set points. The first set of experimental results are shown in Figures 67 and 68. In the electrical AMD indicator, shown in Figure 68, the left part is the healthy data, while the right part is the faulty data. Although this is not a continuous experiment, an increasing trend is shown from the healthy to the faulty indicators. This is because the healthy and fault data are processed continuously and the later indicator points are calculated based on the earlier indicator points. The clear deviation from healthy AMD indicators to the faulty AMD indicators shows that the bearing fault can be detected when the motor is driven by a VSI with speed feedback control.

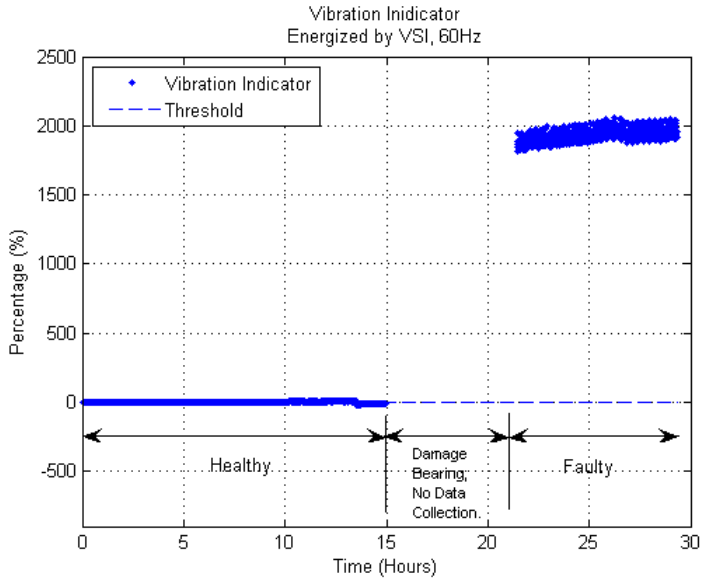

Fig. 67. Vibration Indicator of Data Set #1 for the V/Hz Closed-loop Control; 60Hz Fundamental; 45% Load.

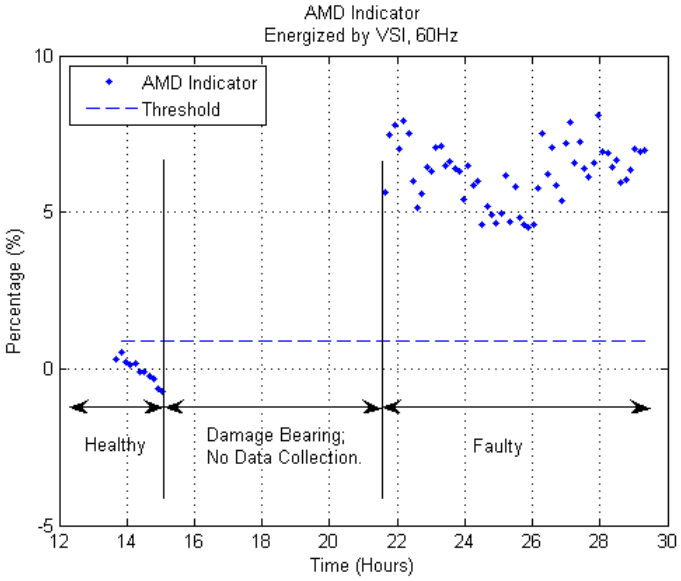

Fig. 68. AMD Indicator of Data Set #1 for the V/Hz Closed-loop Control; 60Hz Fundamental; 45% Load.

The second set of experimental results are shown in Figures 69 and 70. Also in these figures, the left part is the healthy data, while the right part is the faulty data. The clear deviation from healthy AMD indicators to faulty AMD indicators shows that the bearing fault can be detected when the motor is energized by a VSI with speed feedback control.

c. Experiments at 40Hz Set Point

Two experiments are conducted at 40Hz set points. The first set of experimental results are shown in Figures 71 and 72. Also in these figures, the left part is the healthy data, while the right part is the faulty data. The clear deviation from healthy AMD indicators to faulty AMD indicators shows that the bearing fault can be detected when the motor is energized by a VSI operating with speed feedback control.

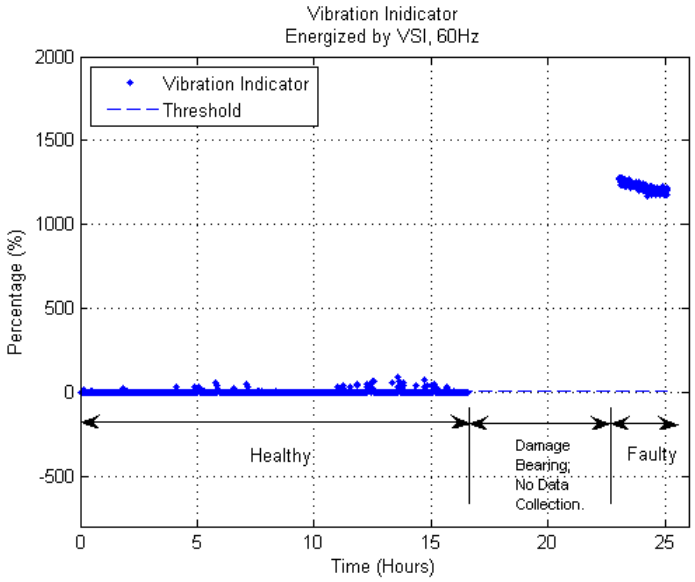

Fig. 69. Vibration Indicator of Data Set #2 for the V/Hz Closed-loop Control; 60Hz Fundamental; 45% Load.

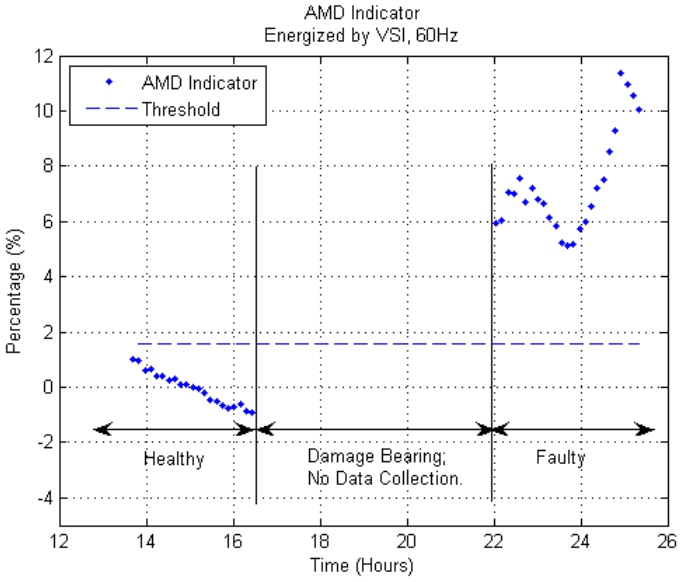

Fig. 70. AMD Indicator of Data Set #2 for the V/Hz Closed-loop Control; 60Hz Fundamental; 45% Load.

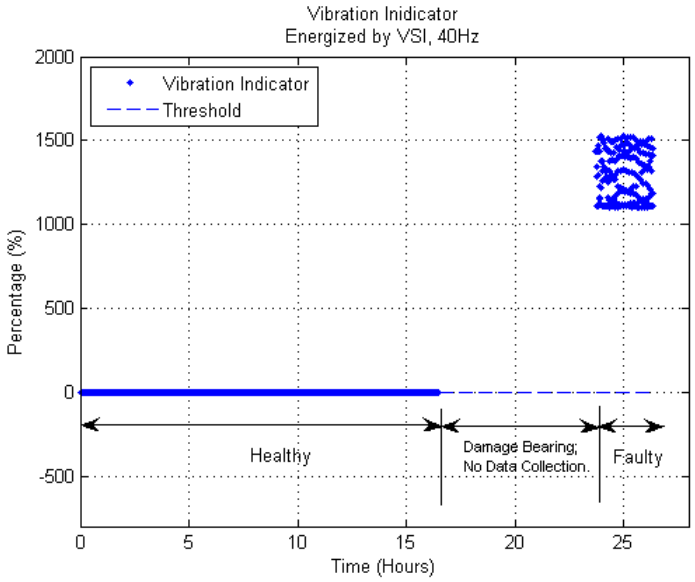

Fig. 71. Vibration Indicator of Data Set #1 for the V/Hz Closed-loop Control; 40Hz Fundamental; 41% Load.

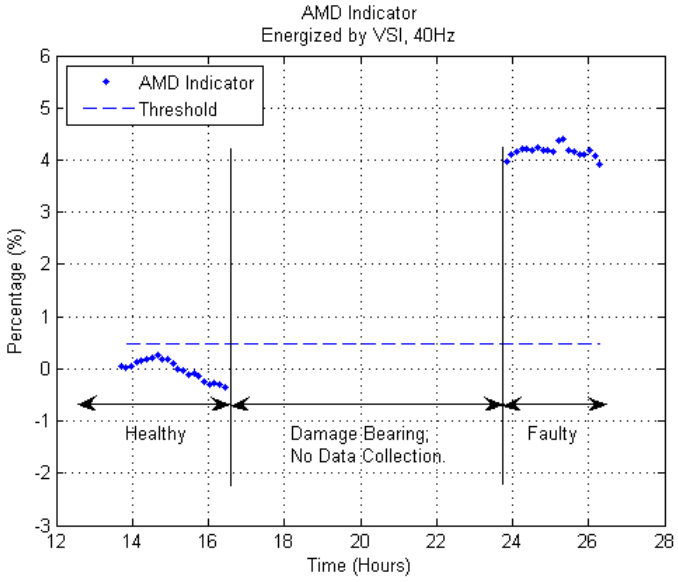

Fig. 72. AMD Indicator of Data Set #1 for the V/Hz Closed-loop Control; 40Hz Fundamental; 41% Load.

The second set of experimental results are shown in Figures 73 and 74. Also in these figures, the left part is the healthy data, while the right part is the faulty data. The clear deviation from healthy AMD indicators to faulty AMD indicators shows that the bearing fault can be detected when the motor is energized by a VSI operating with speed feedback control.

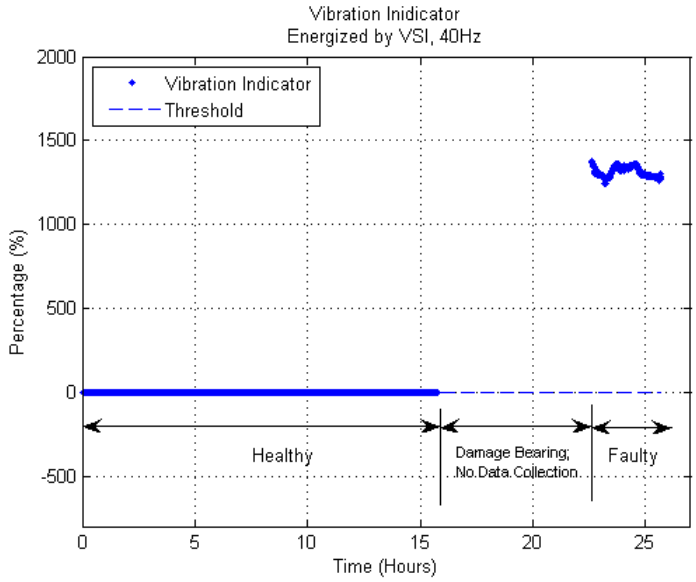

Fig. 73. Vibration Indicator of Data Set #2 for the V/Hz Closed-loop Control; 40Hz Fundamental; 41% Load.

3. Speed Set-point Tracking Using a VSI Operating in Closed-loop V/Hz Control Mode

In the experiments shown in previous sections, motors are operated at steady state conditions. To investigate the effect of motor transient operation condition on the proposed method, two closed-loop control experiments are conducted.

Transient motor operating conditions are achieved by changing the motor speed

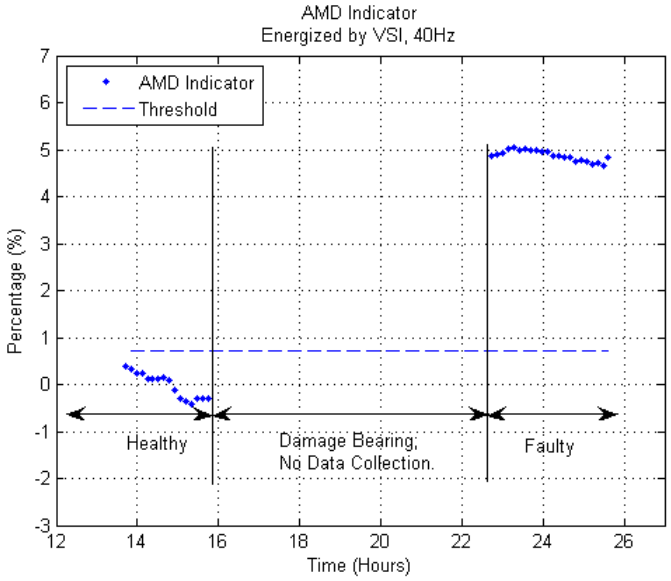

Fig. 74. AMD Indicator of Data Set #2 for the V/Hz Closed-loop Control; 40Hz Fundamental; 41% Load.

set points. First, healthy data are collected at one speed set point; for example, 40Hz or 60Hz. Then, the bearing is damaged using the shaft current. During this bearing damage procedure, there is no data collection. After the bearing is damaged, the motor is operated at different speed set points and data are collected. The followed experimental procedures are shown in Figure 75.

	Stage 1	Stage 2	Stage 3	Stage 4	Stage 5	Stage 6
Speed Set Points	At the speed set point #1	At the speed set point #1	At the speed set point #1	Speed set point was changed from #1 to #2.	Speed set point was changed back to #1	Speed set point was changed from #1 to #2
Operations	Collect healthy data	Damage the bearing using the shaft curret. No data collection	Remove shaft current. Collect faulty data	Collect faulty data in the transient & at speed #2	Collect faulty data in the transient & at speed #1	Collect faulty data in the transient & at speed #2

Fig. 75. Transient Experimental Procedures.

In the first set of experiments, the initial speed set point is 40Hz. Speed set points are changed between 40Hz and 60Hz in transient operating conditions. Vibration indicators are shown in Figure 76. Figure 77 is the detailed plot of the transient operation in Figure 76.

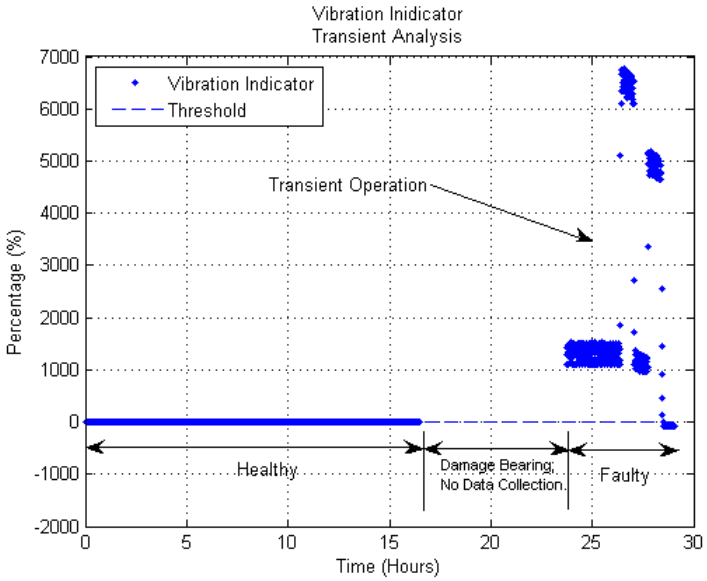

Fig. 76. Vibration Indicator of Data Set #1 for Transient Operation; Closed-loop Control.

In Figure 77, vibration indicators are labeled from '{1}' to '{5}'. The meaning of these numbers are listed in Figure 78. When the entire data set, i.e., data sections from '{1}' to '{5}', are used to calculate the AMD indicator, abnormal results are obtained, as shown in Figure 79. The large deviations between faulty sections and the healthy section comes from the transient data, not from the bearing fault itself. The transient data heavily affect the application of AMD indicators. However, when only using data sections that are in the same speed set point, i.e., sections '{1}', '{2}', and '{4}', the AMD indicator gives reasonable results, as shown in Figure 80.

In the second set of experiments, the initial speed set point is 60Hz. Speed

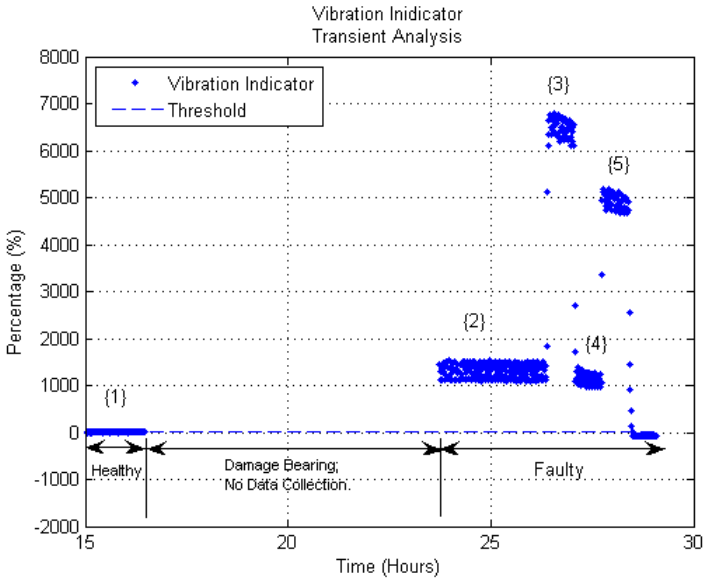

Fig. 77. Vibration Indicator of Data Set #1 for Transient Operation; Closed-loop Control.

Labels	{1}	{2}	{3}	{4}	{5}
Sections	Healthy data at 40Hz speed	Faulty data at 40Hz speed	Faulty data at 60Hz speed	Faulty data at 40Hz speed	Faulty data at 60Hz speed

Fig. 78. Transient Sections in Data Set #1; Closed-loop Control.

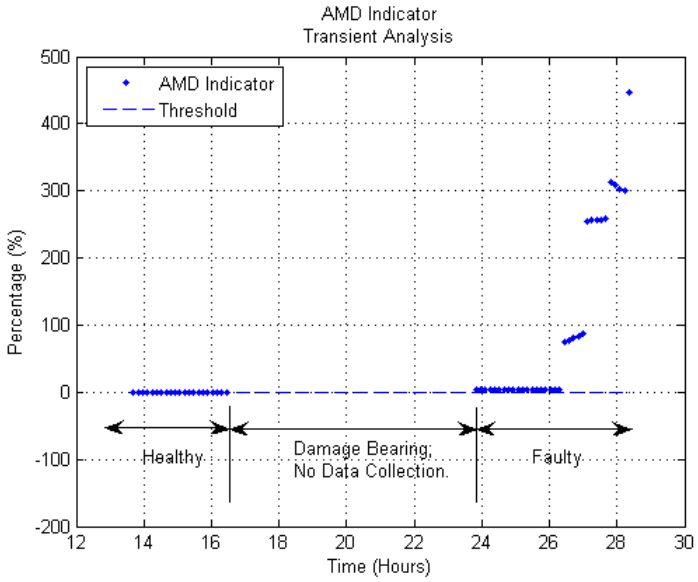

Fig. 79. Incorrect Detection Using AMD Indicator for Transient Operation Data Set #1; Closed-loop Control.

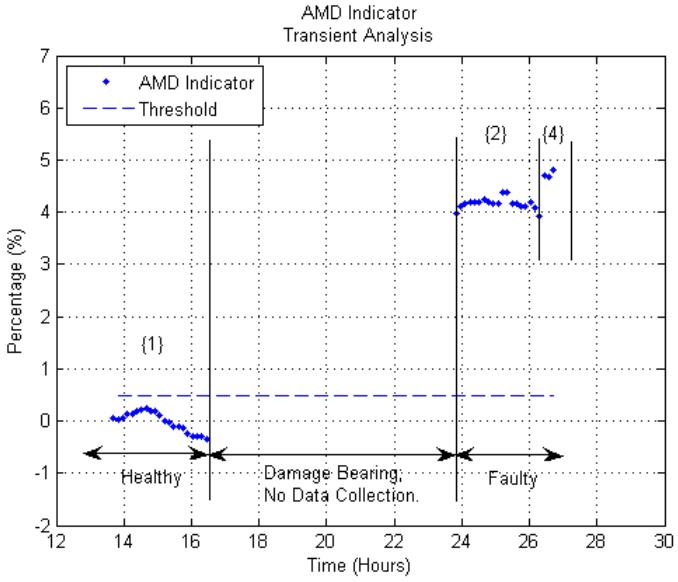

Fig. 80. Correct Detection Using AMD Indicator for Transient Operation Data Set #1; Closed-loop Control.

set points are changed between 60Hz and 40Hz in transient operation conditions. Vibration indicators are shown in Figure 81. Figure 82 is the detailed plot of the transient operation of Figure 81.

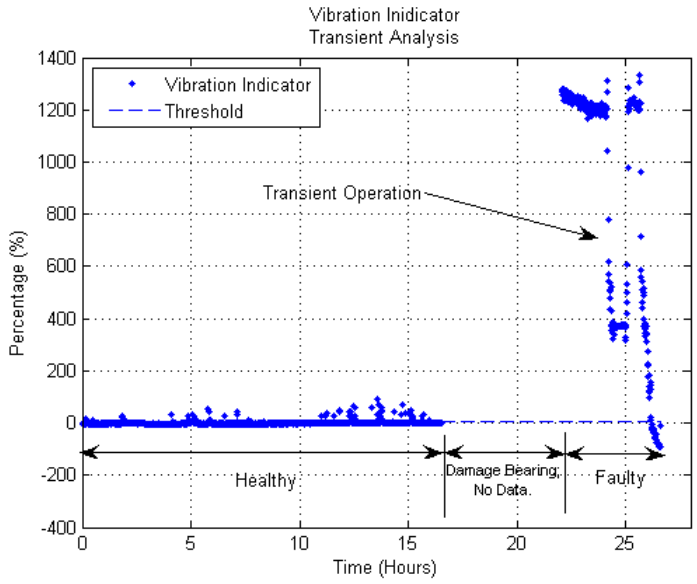

Fig. 81. Vibration Indicator of Data Set #2 for Transient Operation; Closed-loop Control.

In Figure 82, vibration indicators are labeled from '{1}' to '{4}'. The meaning of these numbers are listed in Figure 83. When the entire data set, i.e., data sections from '{1}' to '{4}', are used to calculate the AMD indicator, abnormal results are obtained, as shown in Figure 84. Also, the large deviations between faulty sections and the healthy section come from the transient data, not from the bearing fault itself. When only using data sections, that are in the same speed set point, i.e., sections '{1}', '{2}' and '{4}', the AMD indicator gives reasonable results, as shown in Figure 85.

When motors are operating at different speeds, the magnitude and location of the fundamental frequency changes according to the VSI speed set points. The mag-

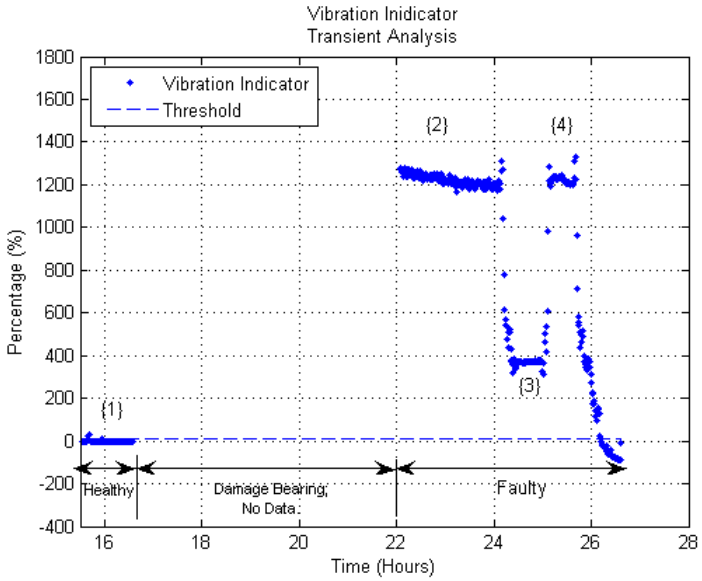

Fig. 82. Vibration Indicator of Data Set #2 for Transient Operation; Closed-loop Control.

Labels	{1}	{2}	{3}	{4}
Sections	Healthy data at 60Hz speed	Faulty data at 60Hz speed	Faulty data at 40Hz speed	Faulty data at 60Hz speed

Fig. 83. Transient Sections in Data Set #2; Closed-loop Control.

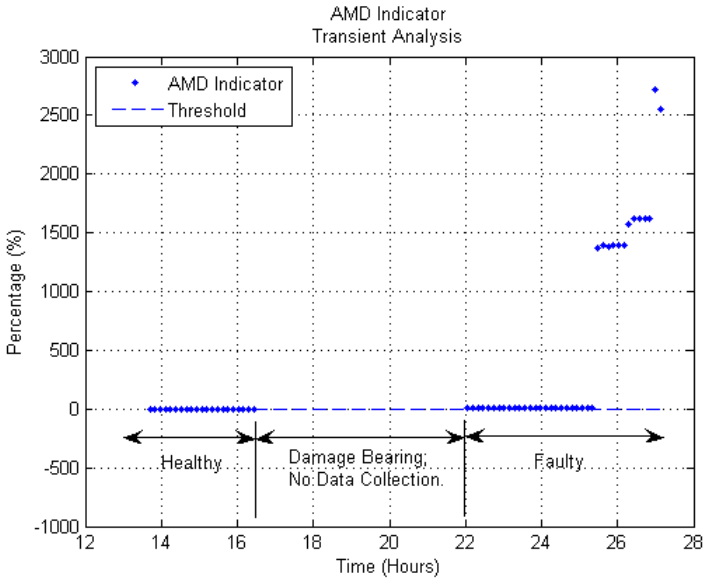

Fig. 84. Incorrect Detection Using AMD Indicator for Transient Operation Data Set #2; Closed-loop Control.

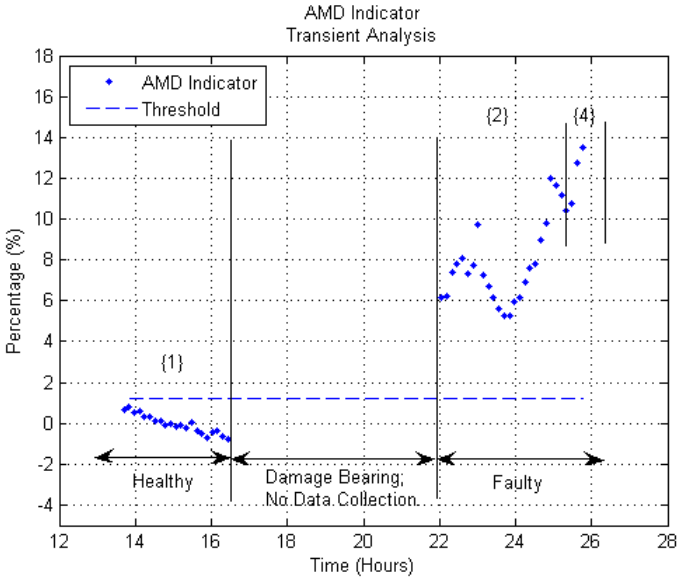

Fig. 85. Correct Detection Using AMD Indicator for Transient Operation Data Set #2; Closed-loop Control.

nitudes and locations of integer harmonics of the fundamental frequency and other inter-harmonics also change. In applying the proposed fault detection method, these variations must be accounted.

G. Effect of Bearing Faults on Motor Efficiency

When the bearing is damaged, the motor losses caused by the increased friction will be larger. This decreases the motor efficiency.

The motor efficiency is calculated as follows,

$$Efficiency = \frac{Torque \times Speed}{\sqrt{3} \times V_{rms} \times I_{rms} \times PF}. \tag{4.1}$$

where V_{rms} and I_{rms} are RMS values of the line voltage and the line current, respectively. PF is the power factor.

The gearbox test-bed is used to conduct an efficiency experiment. The motor torque is measured by an AC100V Torque Detector, and the motor speed is measured by a MP981 encoder. The experiment procedure of the efficiency experiment is the same with the closed-loop experiment procedures listed in Figure 66.

The vibration indicator and the AMD indicator for this experiment are shown in Figures 86 and 87. The motor efficiency is shown in Figure 88. It can be seen that the motor efficiency decreases from around 79.8% in healthy condition, to around 76.5% in faulty condition.

H. Chapter Summary

The experimental results are shown in this chapter. These experiments are based on,

- different power supplies, supply mains, and VSI;
- different load levels, 0%, 20%, 40%, 41%, and 45% loads;

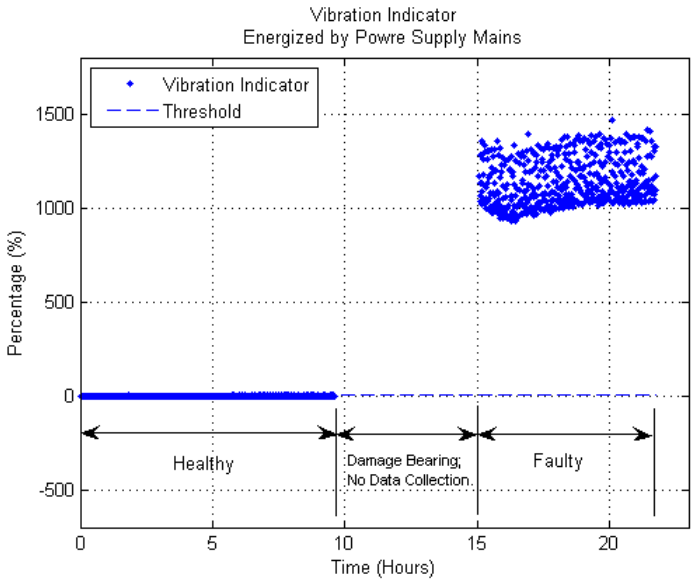

Fig. 86. Vibration Indicator for Motor Energized by Power Supply Mains.

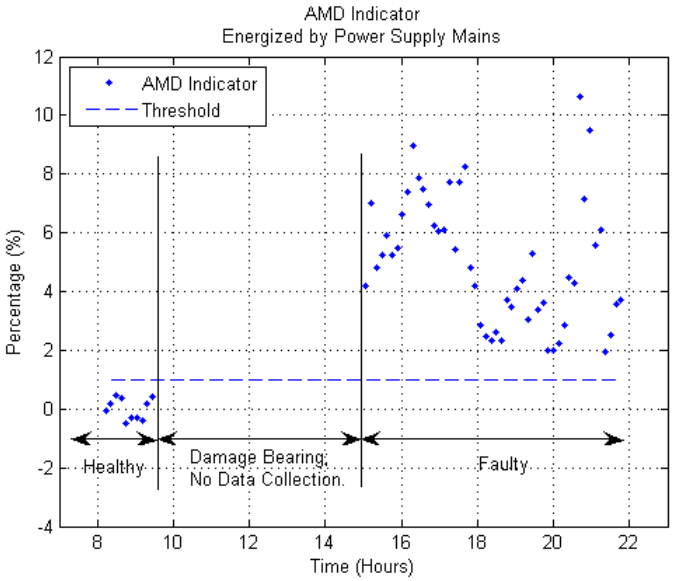

Fig. 87. Electrical AMD Indicator for Motor Energized by Power Supply Mains.

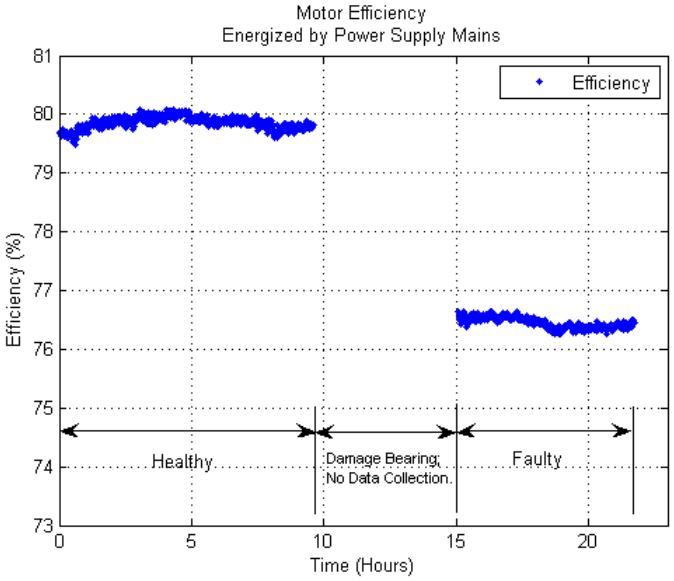

Fig. 88. Motor Efficiency for Motor Energized by Power Supply Mains.

- different VSI control methods, open-loop, and closed-loop controls;
- different motor operation conditions, steady state, and transient operations; and,
- different fault indicators, electrical AMD indicators, and mechanical vibration indicators.

The mechanical vibration indicator can effectively detect mechanical faults of induction motors. It is used as the fault detection capability reference for the electrical AMD indicators. Experimental results show that electrical AMD indicators developed in this research can effectively detect incipient bearing faults in motors with a constant load level. When motors are operating at steady state, experimental results show that the fault detection rate is 100%.

The proposed method cannot be directly used in motors working in transient operation conditions. To use this method in transient operation, additional steps are needed to detect the steady state regions.

The damaged bearing increases motor losses. Experimental result show that the motor efficiency drops significantly when the bearing is damaged.

CHAPTER V

SUMMARY AND CONCLUSIONS

A new approach for rolling element bearing fault detection is proposed. In this chapter, this research is summarized, and future research work is suggested.

A. Summary of Research

The objective of this research is to develop a data driven approach for bearing fault detection of induction motors energized by power supply mains and VSI type drives. In the proposed method, only motor terminal voltages and currents are utilized for fault detection purposes.

To develop a bearing fault detection scheme, bearing faults are often staged in an off-line manner. That is, disassembling the bearing, damaging it separately and then assembling the machine. The act of disassembling, reassembling, remounting, and realigning the test motor significantly alters the current and vibration characteristics of the machine, which is one of the difficulties in developing a bearing fault monitoring scheme. In this research, in-situ bearing damage experiments are conducted so that the life span of the bearing can be simulated in an accelerated manner and a bearing fault detection scheme can be developed and tested.

Bearing faults can be categorized into single point defects and generalized roughness defects. In both single point defect and generalized roughness bearing faults, the damaged bearing leads to radial motion between the stator and the rotor. This kind of motion varies the air gap of the machine, so that the original amplitude modulation relationships in the healthy motor are changed when bearings are damaged. In single point defect bearing defects, the fault related frequencies can be determined using the bearing geometric dimensions, while in generalized roughness bearing defects,

the fault related frequencies are located in wide frequency bands and are not easily predictable. Moreover, the damaged bearing impedes the rotor rotation and imposes extra load on the motor. Although this extra load itself is small and ignorable, the load fluctuations of the motor are increased. These load fluctuations are also modulated by frequency components in input voltages. Because the fundamental frequency is dominated in the voltage spectrum, amplitude modulation relationships between spatial harmonics and all other voltage harmonics are masked. Only the amplitude modulation relationship between spatial harmonics and the voltage fundamental frequency can be used for the fault detection purpose.

Bearing faults can be captured easily in frequencies that are modulated with the fundamental frequency of the supply. This modulation relationship can be isolated using the phase coupling between the bearing fault frequencies and the supply fundamental frequency. An Amplitude Modulation Detector (AMD), developed from the estimation of the higher order spectrum, can correctly capture the phase coupling and isolate these modulation relationships. This is the proposed approach in this research.

Induction motors are commonly energized by power supply mains or VSI type drives. The system power supply plays a very important role in induction motor bearing fault detection. Variations in the power supply definitely change the stator current spectrum and mask bearing fault information. To negate the effects of the power supply, bearing fault indicators are developed using stator currents and the voltages.

In Chapter II, causes of bearing faults and failures are explained. Amplitude modulation relationships of bearing single point defects and generalized roughness faults are discussed. The in-situ bearing damage experiment setups used in this research are described. Practical experiment issues, such as shaft currents, grease

amount, and experiment time, are discussed.

In Chapter III, estimation procedures for the AMD are introduced. Effects of supply voltages on stator currents are explored. Based on this, a modulation model and electrical AMD indicator are derived. Moreover, a mechanical vibration indicator is provided. This indicator is used as a reference for the fault detection capability of the electrical indicator.

In Chapter IV, experimental results are shown based on power supply mains and VSI, different load levels, different VSI control schemes, and different motor operating conditions. Taking the mechanical vibration indicator as a reference for fault detection, the proposed method is shown as effective in detecting incipient bearing faults in induction motors.

B. Conclusions

The conclusions drawn from this research are summarized as follows:

1. The developed approach can effectively detect incipient bearing faults in induction motors energized by power supply mains and VSI type drives. This approach is load dependent. If motors are operated at near steady state conditions, then experimental results show that the bearing fault detection rate is 100% and there are no false alarms.

2. The developed approach is intended for motors operated at steady-state conditions. If transient conditions are encountered, then the data must be preprocessed to segment the steady-state regions.

C. Recommendations for Future Research

The fault detection method developed in this research is demonstrated to be an effective way for detecting rolling element bearing faults. Based on the research reported in this dissertation, some possible topics for future research are:

1. Load independence - The proposed method is load dependent. To negate the load effects of the bearing fault detection method is one of the most important topics for future research.

2. Other types of motor faults - The proposed method not only could detect bearing faults, but it could also detect other types of motor faults that introduce some form of modulation relationships in the spectrum of motor terminal signals. Hence, further tests on other types of motor faults are needed.

3. Diagnosis - Distinguishing the bearing faults from other types of motor faults.

4. Prognostics - Predicting the remaining operational life of damaged bearing.

REFERENCES

[1] R. R. Schoen and T. G. Habetler, "Effects of Time-Varying Loads on Rotor Fault Detection in Induction Machines," *IEEE Transactions on Industry Applications*, vol. 31, no. 4, pp. 900–906, July 1995.

[2] P. F. Albrecht, J. C. Appiarius, R. M. McCoy, E. L. Owen, and D. K. Sharma, "Assessment of the Reliability of Motors in Utility Applications - Updated," *IEEE Transactions on Energy Conversion*, vol. EC-1, no. 1, pp. 39–46, March 1986.

[3] IAS Motor Reliability Working Group, "Report of Large Motor Reliability Survey of Industrial and Commercial Installations, Part I," *IEEE Transactions on Industry Applications*, vol. IV-21, no. 4, pp. 853–864, July 1985.

[4] M. E. H. Benbouzid, "What Stator Current Processing-Based Technique to Use for Induction Motor Rotor Faults Diagnosis," *IEEE Transactions on Engergy Conversion*, vol. 18, no. 2, June. 2003.

[5] P. J. Tavner and J. Penman, *Condition Monitoring of Electrical Machines*, Letchworth, UK: Research Studies Press, 1987.

[6] K. Kim, A.G. Parlos and R.M. Bharadwaj, "Sensorless Fault Diagnosis of Induction Motors," *IEEE Transactions on Industrial Electronics*, vol. 50, no. 5, pp. 1038-1051, Oct., 2003.

[7] P. M. Frank, "Robust Model-Based Fault Detection in Dynamic Systems," in *On-Line Fault Detection and Supervision in the Chemical Process Industries*, P. S. Dhurjati and G. Stephanopoulos, Oxford, UK: Pergamon Press, 1993, vol. 1, pp. 1–13.

[8] G. B. Kliman and J. Stein, "Methods of Motor Current Signature Analysis," *Electric Machines and Power Systems*, vol. 20, no. 5, pp. 463–474, September 1992.

[9] J. R. Cameron, W. T. Thomson, and A. B. Dow, "On-Line Current Monitoring of Induction Motors - A Method for Calculating the Level of Air-Gap Eccentricity," in *IEEE 3rd International Conference on Electric Machines and Drives*, pp. 173–177, IEE Publication no. 282, November 1987.

[10] A. J. Marques-Cardoso and E. S. Saraiva, "Computer-Aided Detection of Air-Gap Eccentricity in Operating Three-Phase Induction Motors, by Park's Vector Approach," *IEEE Transactions on Industry Applications*, vol. 29, no. 5, pp. 165–171, September 1993.

[11] P. Torasso and L. Console, *Diagnostic Problem Solving*, Oxford, UK: North Oxford Academic, 1989.

[12] L. F. Pau, "Survey of Expert Systems for Fault Detection, Test Generation, and Maintenance," *Expert Systems*, vol. 3, no. 2, pp. 100–111, April 1986.

[13] S. L. Fulton and C. O. Pepe, "An Introduction to Model-Based Resoning," *AI Expert*, pp. 48–55, Jan. 1990.

[14] A. S. Willsky, "A Survey of Design Methods for Failure Detection in Dynamic Systems," *Automatica*, vol. 12, pp. 601–611, 1976.

[15] R. Isermann and P. Ball, "Trends in the Appication of Model-Based Fault Detection and Diagnosis of Technical Processes," in *Proc. of the 13th IFAC World Congress*, pp. 1–12, Piscataway, NJ: IEEE Press, 1996.

[16] R. O. Duda and P. E. Hart, *Pattern Classification and Scene Analysis*, New York: John Wiley & Sons, 1973.

[17] T. Asakura, T. Kobayashi, and S. Hayashi, "A Study of Fault Diagnosis System Using Neural Networks," in *Proc. of the 29th ISCIE International Symposium on Stochastic Systems Theory and Its Applications*, pp. 19–24, Tokyo, Japan, 1998.

[18] D. M. Himmelblau, "Use of Artificial Neural Networks to Monitor Faults and for Troubleshooting in the Process Industries," in *IFAC Symposium On-Line Fault Detection and Supervision in the Chemical Process Industry*, pp. 89–99, Oxford, UK: Pergamon Press, 1992.

[19] S. Becker, "Unsupervised Learning Procedures for Neural Networks," *International Journal of Neural Systems*, vol. 2, no. 1, pp. 17–33, Spring 1991.

[20] J.R. Stack, "Fault Classification and Fault Signature Production for Rolling Element Bearings in Electric Machines," *IEEE Transactions on Industry Applications*, vol. 40, no. 3, May/June 2004.

[21] R. R. Schoen, "Motor Bearing Damage Detection Using Stator Current Monitoring," *IEEE Transactions on Inductry Applications*, vol. 31, no. 6, Nov./Dec. 1995.

[22] J.R. Stack, "An Amplitude Modulation Detector for Fault Diagnosis in Rolling Element Bearings," *IEEE Transactions on Industrial Electronics*, vol. 51, no. 5, Oct. 2004.

[23] R. R. Obaid, Thomas G. Habetler, and J.R. Stack, "Stator Current Analysis for Bearing Damage Detection in Induction Motors," *Symposium on Diagnostics for*

Electric Machines, Power Electrionics and Drives, Atlanta, GA, 24-26 Aug. 2003.

[24] I. Y. Onel, K.B. Dalci and I. Senol, "Detection of Outer Raceway Bearing Defects in Small Induction Motors Using Stator Current Analysis," *Sadhana*, vol. 30, Part. 6, pp. 713-722, Dec. 2005.

[25] M. Blodt, P. Granjon, B. Raiso and G. Rostaing, "Models for Bearing Damage Detection in Induction Motors Using Stator Current Monitoring," *IEEE International Symposium*, vol. 1, pp. 383-388, May 2004.

[26] B. Yazici and, G. B. Kilman, "An Adaptive Statistical Time-frequency Method for Detection of Broken Bars and Bearing Faults in Motors Using Stator Current," *IEEE Transaction on Industry Applications*, vol. 35, pp. 442-452, Mar./Apr. 1999.

[27] L. Eren and M. J. Devaney, "Bearing Damage Detection via Wavelet Packet Decomposition of the Stator Current," *IEEE Transaction on Instrumentation and Measurement*, vol. 53, no. 2, Apr. 2004.

[28] J.R. Stack, "Bearing Fault Detection via Autoregressive Stator Current Modeling," *IEEE Transactions on Industry Applications*, vol. 40, no. 3, May/June 2004.

[29] D.N.Zmood and D.G.Holmes, "Improved Voltage Regulation for Current Source Inverters," *In Conference Record of the 2000 IEEE Industry Applications Conference Thirty-fifth IAS Annual Meeting*, Rome, Italy, vol. 4, pp. 2353-2360, 2000.

[30] R. Wieser, M. Schagginger, C. Kral, and F. Pirker, "The Integration of Machine Fault Detection into an Indirect Field Oriented Induction Machine Drive Control

Scheme, the Vienna Monitoring Method", *Industry Applications Conference*, Chicago, IL, vol. 1, pp. 12-15, Oct. 1998.

[31] R. Wieser, C. Kral, F. Pirker, and M. Schagginger, "Online Rotor Cage Monitoring of Inverter Fed Induction Machines by Means of an Improved Method", *IEEE Transactions on Power Electronics*, vol. 14, no. 5, Sept. 1999.

[32] C. Kral, R. Wieser, F. Pirker, and M. Schagginger, "Sequences of Field Oriented Control for the Detection of Faulty Rotor Bars in Induction Machines - the Vienna Monitoring Method", *IEEE Transactions on Inductrial Electronics*, vol. 47, no. 5, Oct. 2000.

[33] A. Bellini, F. Filippetti, G. Franceschini, and C. Tassoni, "Classification of Diagnostic Indexes for Field Oriented Induction Motor Drives", *Symposium on Diagnostics for Electric Machines, Power Electronics and Drives*, Atlanta, GA, 24-26, Aug. 2003.

[34] A. Bellini, F. Filippetti, G. Franceschini, and C. Tassoni, "Closed Loop Control Impact on the Diagnosis of Induction Motors Faults", *IEEE Transactions on Industry Applications*, vol. 36, no. 5, Sept.-Oct. 2000.

[35] C.M Chen and K.A. Loparo, "Electric Fault Detection for Vector Controlled Induction Motors Using the Discrete Wavelet Transform". *Proceedings of the American Control Conference*, Philadelphia, PA, June 1998.

[36] R. M. Tallam, T.G. Habetler and R.G. Harley, "Stator Winding Turn-fault Detection for Closed Loop Induction Motor Drives", *IEEE Transactions on Industry Applications*, vol. 39, Issue: 3, May-June 2003, p720 - 724.

[37] J. Blattner, H. Gutt and V. Schlechter, "Sensorless Detection of Rotor Cage

Defects for Inverter Fed Induction Motors", *Industrial Electronics Society, Proceedings of the 24th Annual Conference of the IEEE*, vol. 4, pp. 2311 - 2315, Aug.- Sept. 1998.

[38] J.R. Stack, "Experimentally Generating Faults in Rolling Element Bearings Via Shaft Current," *IEEE Transactions on Industry Applications*, vol. 41, no. 1, Jan/Feb 2005.

[39] H. Prashad, "Diagnosis of Rolling-element Bearings Failure by Localized Electrical Current between Track Surfaces of Races and Rolling-elements," *Journal of Tribology*, vol. 124, no. 3, pp. 468- 473, July 2002.

[40] D.F. Busse, J.M. Erdman, R.J. Kerkman, D.W. Schlegel, and G.L. Skibinski, "The Effects of PWM Voltage Source Inverters on the Mechanical Performance of Roller Bearings," *IEEE Transactions on Industry Applications*, vol. 33, no. 2, pp. 567-576, Mar./Apr. 1997.

[41] J.M. Erdman, R.J. Kerkman, D.W. Schlegel, and G.L. Skibinski, "Effect of PWM Inverts on AC Motor Bearing Currents and Shaft Voltages," *IEEE Transactions on Industry Applications*, vol. 32, no. 2, pp. 250-259, Mar./Apr. 1996.

[42] J.W. Choi, "Analysis of Electrical Signatures in Synchronous Generators Characterized by Bearing Faults," M.S. Thesis, Mechanical Engineering, Texas A&M University, College Station, Texas, Aug. 2006.

[43] C.L. Nikias and M.R. Raghuveer, "Bispectrum Estimation: A Digital Signal Processing Framework," *Proceedings of the IEEE.*, vol. 75, no. 7, July 1987.

[44] G.K.Dubey, *Fundamentals of Electrical Drives*, 2nd, Pangbourne, UK, Alpha Science International Ltd., 2001.

[45] S.J.Chapman, *Electric Machinery Fundamentals*, 3rd, New York, NY, McGraw-Hill, 1999.

[46] M.H.Rashid, *Power Electronics Handbook*, Burlington, MA, Academic Press, 2001.

[47] P. C. Krause, O. Wasynczuk and S. D. Sudhoff, *Analysis of Electric Machinery*, New York, NY, IEEE Press, 1995.

APPENDIX A

DEFINITIONS OF HIGHER ORDER CUMULANTS AND SPECTRA

In this section, a brief overview of higher order spectra is presented. Detailed information on this topic can be found in [43] and [**?**].

Higher order spectra are defined in terms of cumulants and therefore are also called cumulant spectra. Given a set of n real random variables $x_1, x_2, ..., x_n$, their joint cumulants of order $r = k_1 + k_2 + ... + k_n$ are defined as

$$c_{k_1,...,k_n} = (-j)^r \frac{\partial^r ln\Phi(\omega_1, \omega_2, ..., \omega_n)}{\partial\omega_1^{k_1}\partial\omega_2^{k_2}...\partial\omega_n^{k_n}}|_{\omega_1=\omega_2=...=\omega_n=0}, \tag{A.1}$$

where $\Phi(\omega_1, \omega_2, ..., \omega_n) = E[e^{j(\omega_1 x_1 + ... + \omega_n x_n)}]$ is their joint characteristic function.

The joint moments of order r of the same set of random variables are given by

$$\begin{aligned} m_{k_1,...,k_n} &= E[x_1^{k_1} x_2^{k_2} ... x_n^{k_n}] \\ &= (-j)^r \frac{\partial^r \Phi(\omega_1, \omega_2, ..., \omega_n)}{\partial\omega_1^{k_1}\partial\omega_2^{k_2}...\partial\omega_n^{k_n}}|_{\omega_1=\omega_2=...=\omega_n=0}. \end{aligned} \tag{A.2}$$

Hence, the joint cumulants can be expressed in terms of the joint moments of the random variables.

By taking $X(n), n = 0, 1, 2, ...$ to be a real stationary random process with zero mean, $E[X(n)] = 0$, then the moment sequences of the process are related to its cumulants as given below:

Autocorrelation sequence:

$$E[X(n)X(n + \tau_1)] = m_2(\tau_1) = c_2(\tau_1), \tag{A.3}$$

Third order moment or cumulant sequence:

$$E[X(n)X(n+\tau_1)X(n+\tau_2)] = m_3(\tau_1,\tau_2) = c_3(\tau_1,\tau_2), \tag{A.4}$$

Fourth order moment sequence:

$$\begin{aligned} E[X(n)X(n+\tau_1)X(n+\tau_2)X(n+\tau_3)] &= m_4(\tau_1,\tau_2,\tau_3) \\ &= c_4(\tau_1,\tau_2,\tau_3) + c_2(\tau_1)c_2(\tau_3-\tau_2) \\ &\quad + c_2(\tau_2)c_2(\tau_3-\tau_1) + c_2(\tau_3)c_2(\tau_2-\tau_1). \end{aligned} \tag{A.5}$$

The N^{th} order spectrum $C(\omega_1,\omega_2,...,\omega_n)$ of the process $X(n)$ is defined as the Fourier Transform of its Nth order cumulant sequence $c_N(\tau_1,\tau_2,...,\tau_{N-1})$,

$$C(\omega_1,\omega_2,...,\omega_n) = \sum_{\tau_1=-\infty}^{\infty} ... \sum_{\tau_{N-1}=-\infty}^{\infty} c_N(\tau_1,\tau_2,...,\tau_{N-1}) e^{-j(\omega_1\tau_1+...+\omega_{N-1}\tau_{N-1})}. \tag{A.6}$$

In general, $C(\omega_1,\omega_2,...,\omega_n)$ is complex and a sufficient condition for its existence in that $c_N(\tau_1,\tau_2,...,\tau_{N-1})$ is absolutely summable. The power spectrum, bispectrum and trispectrum are special cases of the N^{th} order spectrum defined by equation (A.6).

At this point, a natural question that arises is why the N^{th} order spectrum (or polyspectrum) is defined as the Fourier Transform of the cumulant rather than of the moment sequence of $X(n)$. The reason is twofold: a) if $X(n)$ is a stationary Gaussian random process, than all its N^{th} order moments for $N \geq 3$ do not provide any additional information pertaining to the process. It is, therefore, better to have a function that shows this fact explicitly. The cumu1ant spectrum function does so since higher order ($N \geq 3$) cumulants are zero for Gaussian processes; b) if the random variables $x_1,...,x_n$ can be divided into any two or more groups which are statistically independent, their N^{th} order cumulants are identically zero. Hence, cumulant spectra provide

a suitable measure of statistical dependence. Finally, the ergodicity requirements are met more easily with cumulants than with moments.

APPENDIX B

CALCULATION OF THE RMS, THD, IMBALANCE AND SNR

The Root Mean Square (RMS) of a time series $x(n)$ is defined as follows,

$$RMS = \sqrt{\frac{1}{N}\sum_{i=1}^{N} x(i)^2}. \tag{B.1}$$

The Total Harmonic Distortion (THD) is defined as the RMS value of the total harmonics of the signal, divided by the RMS value of its fundamental frequency. The THD is defined as,

$$THD = \frac{\sqrt{I_2^2 + I_3^2 + ... + I_n^2}}{I_F}. \tag{B.2}$$

where I_n is the RMS value of the n^{th} harmonics; I_F is the RMS value of the fundamental frequency.

For three phase signals a, b, c, the imbalance is calculated as,

$$Imbalance = \frac{\max|RMS_{(a,b,c)} - avg|}{avg}. \tag{B.3}$$

where $RMS_{(a,b,c)}$ is the individual RMS values of the a, b, c phases, and avg is the average of the RMS over the three phases.

Signal to noise ratio is an engineering term for the power ratio between a signal (meaningful information) and the background noise. It is defined as,

$$SNR(dB) = 10\log_{10}(\frac{P_{signal}}{P_{noise}}) \tag{B.4}$$

where P is the average power.

VITA

Lin Wang received his Bachelor of Science degree from Zhejiang University at Hangzhou, P.R. China in 1995, and his Master of Science degree from Southwest Jiaotong University at Chengdu, P.R. China in 1998, respectively, both in Mechanical Engineering. In May 2007, he received his Ph.D degree from Texas A&M University. His research interests include signal processing, induction motor fault detection and diagnosis, Artificial Intelligence techniques, and dynamic system estimation and control.

Mr. Lin Wang may be reached at Department of Mechanical Engineering, Texas A&M University, College Station, TX 77843. His email address is linwang@tamu.edu.